Metal-organic frameworks for photoelectrochemical hydrogen production

Abstract

The use of fossil fuels and the resulting increase in CO_2 concentrations in the atmosphere have led to a climate crisis that is causing devastating consequences around the globe. Among the other renewable energy solutions, hydrogen is acknowledged to be one of the priority areas in clean energy transition. Today, several hydrogen production technologies are being used, but the most efficient ones are still based on non-renewable resources. Therefore, in order to reduce the greenhouse gas emissions, the hydrogen sector needs to develop greener production technologies fast. In this Master's thesis, metal-organic frameworks (MOFs) are proposed as a promising solution to green hydrogen production due to their many suitable properties. For example, MOFs can be used in light absorbing photoelectrodes in photoelectrochemical (PEC) cells offering more active sites, directing charge transfers, and expanding the range of light absorption. In this way, hydrogen can be produced via water splitting utilizing only electricity and direct solar radiation as energy sources.

In the experimental part, different MOF compounds suitable for water splitting were synthetised. Previously reported MOFs, CuI-(bpy) and Ce-UiO-66 compounds with different ligands were synthetised in mild reaction conditions, and the Ce-UiO-66-NH_2 structure – reported as the most promising for hydrogen production of the Ce-UiO-66 compounds – was attempted to be grown on a fluorine doped tin oxide (FTO) electrode for the further use in PEC cells. Other research groups have already reported modified ZIF-8 and NH_2-MIL-125 MOFs to be directly grown on electrode materials, nickel foam (NF) and FTO respectively, and these syntheses were repeated in this work as well. One well known MOF structure, NH_2-UiO-66 was attempted to be synthetised by combining reaction parameters from two different articles for a simpler and faster production. The reactions of the work were carried out as saturation crystallization, solvothermal and hydrothermal reactions and by refluxing. Powdery samples were characterised by thermogravimetric analysis (TGA) and powder X-ray diffraction (PXRD), and for the electrode samples, TGA, PXRD and scanning electron microscopy (SEM) with an energy dispersive X-ray spectroscopy (EDX) were used. However, it was noticed, that these characterisation methods might not be the most suitable for investigating structures grown on top of the electrode materials, because of the nano scale of the target compounds and the macro scale of the electrodes. This size difference caused the signals of the electrode materials to cover the signals of the MOFs and their possible dopants. Therefore, even if the used characterisation methods give a good overview of the success of known powdery MOF samples, compounds grown on an electrode require other, more precise techniques.

Tiivistelmä

Fossiilisten polttoaineiden käyttö ja siitä johtuva hiilidioksidipitoisuuden kasvu ilmakehässä ovat johtaneet ilmastokriisiin, joka aiheuttaa tuhoisia seuraamuksia ympäri maailmaa. Muiden uusiutuvien energiaratkaisujen joukossa vety on tunnustettu yhdeksi painopistealueista puhtaaseen energiaan siirtymisessä. Jo tällä hetkellä on käytössä useita vedyn tuotantotekniikoita, mutta niistä tehokkaimmat pohjautuvat edelleen uusiutumattomiin luonnonvaroihin. Kasvihuonekaasupäästöjen vähentämiseksi vetysektorin on siksi kehitettävä nopeasti vihreämpiä tuotantotekniikoita. Tässä pro gradu -tutkielmassa metalliorgaaniset verkkorakenteet (eng. *metal-organic framework,* MOF) esitellään yhtenä lupaavista ratkaisuista vihreän vedyn tuotannossa niiden monien sopivien ominaisuuksien vuoksi. MOF-yhdisteitä voidaan esimerkiksi käyttää valoa absorboivissa elektrodeissa valosähkökemiallisissa (eng. *photoelectrochemical,* PEC) kennoissa tarjoten reaktiopinta-alaa, ohjaten sähkövarausten siirtoa ja laajentaen valon absorptiospektriä. Näin vetyä voidaan tuottaa veden halkaisun avulla hyödyntäen energianlähteinä ainoastaan sähköä ja suoraa auringonvaloa.

Kokeellisessa osassa syntetisoitiin erilaisia veden halkaisureaktioihin soveltuvia MOF-yhdisteitä. Aiemmin raportoituja MOF-rakenteita, CuI-(bpy):ä ja erilaisilla ligandeilla varustettuja Ce-UiO-66-yhdisteitä valmistettiin miedoissa reaktio-olosuhteissa, ja Ce-UiO-66:n aminofunktionalisoitua rakennemuotoa – joka on raportoitu lupaavimmaksi erilaisista Ce-UiO-66-yhdisteistä vedyn tuotannossa – yritettiin kasvattaa fluoriseostetun tinaoksidilasin (FTO) päällä mahdollista jatkokäyttöä varten PEC-kennoissa. Muut tutkimusryhmät ovat jo raportoineet erilaisia ZIF-8- ja NH$_2$-MIL-125-MOF-yhdisteitä, joita on kasvatettu suoraan elektrodimateriaalina toimivan nikkelihuovan (eng. *nickel foam*, NF) tai FTO:n pinnalle, ja nämä synteesit toistettiin myös tässä työssä. Yksi hyvin tunnettu MOF-rakenne, NH$_2$-UiO-66, pyrittiin syntetisoimaan yhdistämällä kahden eri synteesireseptin reaktio-olosuhteet. Sovelletun reaktion tavoitteena oli saavuttaa aiempaa yksinkertaisempi ja nopeampi valmistusmenetelmä kyseiselle yhdisteelle. Kokeellisen osuuden synteeseissä käytettiin muun muassa saturaatiokiteytyksiä, solvo- ja hydrotermisiä reaktioita sekä refluksointia. Pulverimaiset näytteet karakterisoitiin termogravimetrisellä analyysillä (TGA) sekä jauheröntgendiffraktiolla (eng. *powder X-ray diffraction*, PXRD), ja elektrodinäytteille käytettiin näiden menetelmien lisäksi pyyhkäisyelektronimikroskopiaa (eng. *scanning electron microscopy*, SEM), jossa hyödynnettiin myös energiadispersiivistä röntgenspektroskopiaa (eng. *energy-dispersive X-ray spectroscopy*, EDX*)* alkuaineiden tunnistamiseksi. Kuitenkin havaittiin, että nämä

karakterisointimenetelmät eivät ole kaikkein sopivimpia elektrodimateriaalien päälle kasvatettujen rakenteiden tutkimiseen kohdeyhdisteiden nanomittakaavan sekä elektrodien makromittakaavan vuoksi. Kyseinen kokoero sai elektrodimateriaalien signaalit peittämään MOF:ien ja niihin mahdollisesti liittyneiden lisäaineiden signaalit. Vaikka käytetyt karakterisointimenetelmät antoivat hyvän yleiskuvan analysoitujen jauhemaisten MOF-näytteiden koostumuksesta, elektrodilla kasvatetut yhdisteet vaativat myös edellä mainittuja tarkempia analyysitekniikoita, jotka mahdollistavat eri komponenttien rakenteellisten ominaisuuksien tarkastelun myös nanoskaalassa.

Preface

This Master's thesis was done at the Department of Chemistry at the University of Jyväskylä in the Inorganic Chemistry Department during the year of 2023 and 2024 spring. The experimental part was performed in 2023 between April and June, and the work was supervised by a university lecturer Manu Lahtinen. The focus in this work was metal-organic frameworks (MOFs) and the possibilities to use them in the photoelectrochemical hydrogen production. Scientifical databases used for the literature search were Web of Science, Google Scholar, and JYKDOK and the keywords were related to, for example, metal-organic frameworks, semiconductors and different hydrogen production and water splitting methods.

I want to thank Samu Forsblom, Iida Ulaska and Antti Marttinen for the help in the laboratories and Mahya Asgharian Marzabad for doing the SEM imaging for me. A special big thank you to Manu Lahtinen for flexible and understanding supervision. Last but not least, I want to thank my friends and family for the endless support and believing in me.

Table of contents

Used abbreviations

ACN	Acetonitrile
AEM	Polymer anion exchange membrane
AWE	Alkaline water electrolysis
BDC	benzene-1,4-dicarboxylic acid (terephthalic acid)
BPY	4,4′-bipyridine
BTC	benzene-1,2,4-tricarboxylic acid
CB	Conduction band
CSD	Cambridge Structural Database
C-MOF	Conductive metal-organic framework
DC	Direct current
DCBPy	2,2′-bipyridine-5,5′-dicarboxylic acid
DSC	Differential scanning calorimetry
EDX	Energy-dispersive X-ray spectroscopy
E_g	Band gap energy
HER	Hydrogen evolution reaction
HMT	hexamethylenetetramine
HOMO	Highest occupied molecular orbital
IPCE	Incident photon to electron conversion efficiency
IRMOF	Isoreticular metal-organic frameworks
LUMO	Lowest unoccupied molecular orbital
MO	Molecular orbital
MOF	Metal-organic framework
MW	Micro-wave
NF	Nickel foam

NHE   Normal hydrogen electrode

NP   Nanoparticle

OER   Oxygen evolution reaction

PEC   Photoelectrochemical water splitting

PEM   Proton exchange membrane

PSM   Post-synthetic modification

PXRD   Powder X-ray diffraction

RHE   Reversible hydrogen electrode

SBU   Secondary building unit

SEM   Scanning electron microscopy

SOE   Solid oxide electrolysis

SCXRD   Single crystal X-ray diffraction

TCNQ   Tetracyanoquinodimethane

TG   Thermogravimetry

TGA   Thermogravimetric analysis

VB   Valence band

WGS   Water gas shift

1 Introduction

Greenhouse gases and aerosols play an integral role in the energy balance on Earth regulating the warming effect of the Sun. As they absorb and radiate the heat back from the surface as infrared heat, they maintain a life-supporting temperature of 15 °C on Earth. This way, the build-up of the greenhouse gases in the atmosphere forms a natural greenhouse effect. However, human activities have had a warming impact on the climate since the Industrial Revolution in the middle of the 18th century. Carbon dioxide (CO_2) is one of the most significant greenhouse gases and it participates in the carbon cycle of the Earth. When burning carbon containing fossil fuels, such as coal and oil, the carbon combines with the oxygen in the atmosphere forming atmospheric carbon dioxide. This has increased the CO_2 concentrations over the last century changing the natural greenhouse with a warming effect. The warmer conditions on Earth will lead to the melting of glaciers and the rise of sea levels, drying of some areas and wetting others shifting the climate patterns, thus affecting for example the agriculture and the survival of different species.[1,2]

Approximately 75 % of the greenhouse gas emissions in European Union come from the energy use and production. In 2019, the European Commission presented a new EU growth strategy, The European Greed Deal, which aims to make Europe the first climate neutral continent by the year of 2050. The most energy demanding industries in Europe, such as steel and chemicals are in a key role in Europe's economy, and to reduce emissions from these sectors, they are in an urgent need of green modernisation. Even if the greenhouse gas emissions were already reduced by 23 % between 1990 and 2018 – while the economy grew by 61 % – the current policies will only reach to 60 % of gas emission reduction by 2050. Due to this fact, the Commission has acknowledged still rather little utilized hydrogen to be one of the priority areas in the green energy transition.[3]

1.1 Hydrogen and hydrogen economy

Since the production of molecular H_2 requires energy, hydrogen is not an energy source but an energy carrier, and it can be used as an energy providing fuel. The largest source of hydrogen is water, which makes hydrogen highly abundant on Earth and therefore it's production – when implemented cleanly – does not produce any greenhouse gases, pollutants, or other harm to

environment as a side product. Its energy density is also significantly higher than in most of the currently used fossil fuels such as coal, oil, and gas. In terms of sustainable development, hydrogen has stated to be suitable for carrying energy in many green energy production systems. It can play a big role replacing fossil fuels in industrial sectors – such as steel and chemical – where considerable amounts of carbon emissions are currently emitted. In addition, it can offer alternative solutions to processes, where other renewable energy solutions have been attempted to use but have not been able to completely replace the role of fossil fuels. When it comes to the role of hydrogen as a fuel in transportation, it can be produced near to the hydrogen fueling stations and at least in theory, can be transferred long distances through pipelines or in tankers Therefore, using hydrogen to achieve the European Green Deal and Europe's clean energy transition is highly benefical.[4]

However, for example, the low volumetric energy density of H_2 makes it difficult to store. The available techniques today include physical storage based on absorbents, compression or liquid phase using a lowered temperature (-253 °C, 0.1 MPa). Moreover, there are numerous chemical storage techniques, including the use of metal-hydrides, high hydrogen content possessing amine-borane-adducts and lithium amides or imides. Some thermodynamically tailored systems, wherein components are added to hydrogen storage materials with the intention to stabilise or destabilise a decomposition reaction have been suggested as suitable hydrogen storage techniques. Chemical systems based on the hydrogenation or dehydrogenation of cyclic hydrocarbons as liquid hydrogen carriers have also been proposed. Despite many available technologies, the storage of hydrogen is a widely recognised problem requiring a great deal of development work.[5]

Currently, the production of hydrogen causes 70–100 million tonnes of carbon dioxide emissions every year. Therefore, it is vital to change the processes to carbon neutral in order for hydrogen to play a part in reducing emissions and expand its role as an economically and environmentally efficient energy option.[6] One emerging technology are metal-organic frameworks (MOFs), which have been studied for example as catalysts in water splitting reactions producing hydrogen. Hydrogen production with MOFs could significantly reduce the need of even hazardous materials used in power plants, while requiring only electricity from renewable sources, or even solar light alone as an energy source. In addition, with the use of MOFs, hydrogen could be produced directly at the hydrogen fueling station for use. Because of the everything penetrating nature of hydrogen, it would be beneficial to produce hydrogen on site.
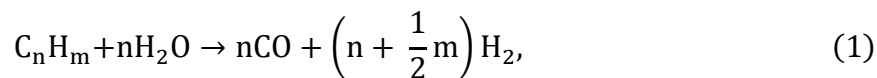
2 Hydrogen production technologies

As mentioned, hydrogen is a very abundant element on earth, and it can be produced through a vast number of techniques. The methods vary in competitiveness and the amounts of produced emissions, which divides them into grey or black, blue, and green hydrogen production categories dependent on the degree of emissions, CO_2 in particular. The most common raw materials used in hydrogen production are fossil fuels, and today almost 50 % of hydrogen is produced using natural gas, such as methane and petroleum gas, 30 % is produced using crude oil, 18 % using coal and only 4% by water electrolysis. According to these percentages, green hydrogen plays still a very small role in hydrogen energy.[7]

2.1 Hydrogen from fossil fuels

Hydrocarbon reforming is widely used, fossil fuel-based hydrogen production method. It can be divided into three different routes, which generally include synthetic gas production and gas separation steps. In syngas production step, the fossil fuel reacts with air/oxygen producing carbon monoxide as a side product. The gas mixture containing CO is directed to a water-gas-shift (WGS) reactor, converting CO to CO_2, and producing additional H_2, thus maximizing the hydrogen production. In the gas separation step the produced CO_2 is captured and H_2 is purified. The most common method to purify H_2, used from the early 1980s, is pressure swing absorption, where the syngas flows through an absorbent, which absorbs the other gases from the mixture.[8]

Steam reforming is a highly endothermic hydrogen production method, that can use natural gas and other methane containing gases as a feed gas. In the method hydrocarbons are converted to hydrogen via carbon monoxide and with aid of steam. If the raw material contains sulphur, the desulphurization step is needed to prevent hydrogen sulphide poisoning of the catalyst (commonly nickel). To achieve pure hydrogen, a very high temperature, up to 900 °C, and pressure of 20–35 bar are required to avoid coking formation on the catalyst and to achieve higher steam-to-carbon (S/C) ratio. After the reformation step, the gas mixture is directed to a WGS reactor where the CO and steam react to produce more H_2. After WGS, the mixture goes through CO_2-removal and methanation, or pressure swing absorption, which leads to almost

100 % H_2 purity. The reactions of reforming, WGS and methanation are shown in equations (1–3), respectively:

$$C_nH_m + nH_2O \rightarrow nCO + \left(n + \frac{1}{2}m\right)H_2, \tag{1}$$

$$CO + H_2O \rightarrow CO_2 + H_2 \tag{2}$$

and

$$CO + 3H_2 \rightarrow CH_4 + H_2O. \tag{3}$$

Steam reforming of methane is the most used and developed method for hydrogen production with an efficiency of 74-85 % and CO_2 emissions of around 8–10 kg per one kg of produced H_2.[9,10]

Another common hydrocarbon reforming method is partial oxidation, which is used when processing heavy, non-compressible and non-pumpable hydrocarbons, such as diesel and coal. Without a catalyst, this method can also be used to operate methane (Equation 1) or naphtha. Comparing to the steam reforming, the main principle of the conversion of the raw material to hydrogen and carbon oxides in hydrocarbon reforming is similar, only in this catalytic method a stoichiometric amount of oxygen is added to partially oxidize the feedstock to produce syngas as shown in Equation (4).

$$C_nH_m + \frac{1}{2}nO_2 \rightarrow nCO + \frac{1}{2}mH_2. \tag{4}$$
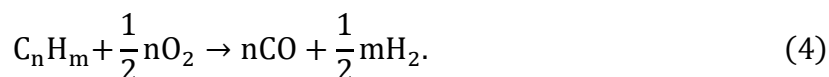
Similarly to the previously technique sulphur must be removed before this step. It is also noteworthy that with a catalyst, the temperature and pressure are similar as steam reforming, but without a catalyst the temperature of partial oxidation process can be up to 1500 °C with a pressure of 80 bar. Although the general reaction Equations (1–3) look very similar to the reaction (4), the processes are thermodynamically the opposite, partial oxidation being an exothermic burning reaction.[9]

The steam reforming and partial oxidation methods can also be combined in a reformer, where these simultaneous processes have their own roles, partial oxidation providing heat, and steam reforming increase the H_2 production rate. This is called autothermal reforming, where the total enthalpy is possible to bring near to zero.[7] In addition to the hydrocarbon reforming methods, hydrocarbons can also be decomposed with heat in hydrocarbon pyrolysis. This process does not require anything else than a light hydrocarbon material with a low boiling point (50-200 °C), and heat as a decomposition catalyst. In pyrolysis, the WGS and CO_2 removal or capture steps are not included.[9]

2.2   Hydrogen from biomass

Biomass, derived from organic material, such as animals and plants and their residues is a renewable source of primary energy. Hydrogen production from biomass can occur via thermochemical or biological methods. Thermochemical processes are fast and offer high yields and they can be considered as environmentally and economically promising options. In a thermochemical process, the biomass is converted to hydrogen and hydrogen-rich gases from syngas. Both pyrolysis and gasification, included in the thermochemical processes, produce methane and CO, which can further be processed via steam reforming and WGS. In pyrolysis, the biomass is heated at 350–550 °C temperatures under 0.1–0.5 MPa pressure generating solid charcoal, liquid oils, and gaseous compounds. If partial combustion is not used, the reactions occur in absence of air. The yield of a pyrolysis process depends on the feedstock, temperature, time, and a catalyst. Biomass gasification uses air, pure oxygen, or steam to convert biomass thermochemically to syngas and the process takes place in between temperatures of 500–1400 °C and pressure of 33 bars depending on the production scale, reactor, and application of the produced syngas. In addition to pyrolysis and gasification, also combustion and liquefaction can be used, but they are not usually as preferable due to the polluting by-products, extremely high pressure and airless reaction conditions.[9]

Especially the biological hydrogen production has increased with the growing attention to sustainability and climate chance. In addition to the environmentally friendly reaction conditions, different waste materials can also be used as a feedstock in these processes. The most used biological hydrogen gas production methods from biomass are bio-photolysis, where bacteria and algae are used to produce hydrogen through their enzyme systems via photosynthesis, and fermentation. Fermentation can be further divided into photo-fermentation, where hydrogen is produced from organic material using solar energy, and dark fermentation, where solar energy is not used. In photo-fermentation, photosynthetic bacteria can be used to convert organic acid, such as lactic and acetic acid into H_2 and CO_2. In dark fermentation carbon hydrate rich substrates, such as glucose, are digested by anaerobic bacteria producing hydrogen and organic acids, which photosynthetic bacteria can then utilize for additional hydrogen. Although the biomass processes cause carbon emissions, the amount of released carbon is equal to the amount absorbed by the once lived organisms and, for this reason, biomass can be considered as a renewable energy source. Even if the biological processes are driven in mild and environmentally friendly conditions, those usually have low production rates and yields.[9]

2.3   Water splitting and solar-to-hydrogen processes

As water splitting accounts less than 4 % of the current hydrogen production techniques, it is clear, that the reaction methods have to be improved in order to increase the share of green energy in the hydrogen energy sector. Decomposition of water molecule consists of two stoichiometric half reactions, which can be described as follows:

$$H_2O + 2h^+ \rightarrow 2H^+ + \frac{1}{2}O_2, \tag{5}$$
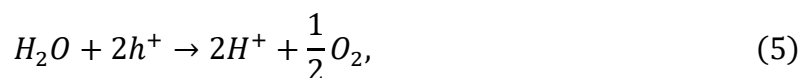
which is called oxygen evolution reaction (OER) and

$$2H^+ + 2e^- \rightarrow H_2, \tag{6}$$

called hydrogen evolution reaction (HER). Together they form the following overall water splitting reaction:

$$H_2O \rightarrow \frac{1}{2}O_2 + H_2. \tag{7}$$

The Gibbs Free energy change (ΔG^θ) of Equation (5) depends on the phase of the water. In a room temperature (25 °C) the ΔG^θ for liquid state is +237.0 kJ/mol and for gaseous +228.4 kJ/mol. Therefore, the water splitting reaction is highly non-spontaneous and needs external energy to occur. For example, solar energy has been a widely used energy source in a green hydrogen production.[11]
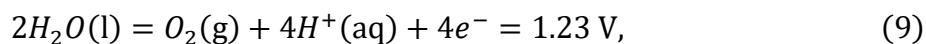
Electrolysis

Water electrolysis can provide an emission-free way to produce hydrogen via water splitting using an electric current through an electrochemical cell. Because the technique requires an external power supply, the consumed energy must be renewal to call the electrolysis process green. The external energy source can be a solar power plant, and the solar energy must be converted to electricity for use of electrolytic process. In general, an electrochemical cell consists of an anode and a cathode, an electrolyte, and an external DC (direct current) power source.[12] The current is applied from the negative terminal of DC source to the anode, from where the electrons flow to the cathode and combine with hydrogen ions of the water forming hydrogen atoms (reduction). Vice versa, the oxidation i.e., the actual water splitting occurs at the anode, where the hydrogen ions and oxygen atoms form. From there, the electrons flow
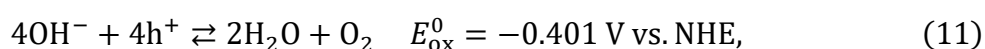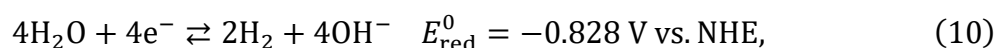
back to the positive terminal of the DC source. The electric potential required for the reduction in water splitting reaction on surface of cathode is
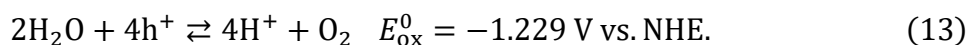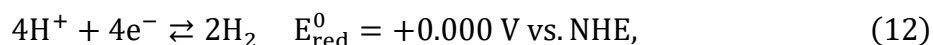
$$2H^+(\text{aq}) + 2e^- = H_2(\text{g}) = 0.00 \text{ V},\tag{8}$$
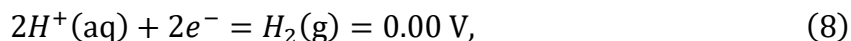
and for oxidation on surface of anode is

$$2H_2O(\text{l}) = O_2(\text{g}) + 4H^+(\text{aq}) + 4e^- = 1.23 \text{ V},\tag{9}$$

which indicates the theoretical minimum electricity input.[11,13] The corresponding potentials in alkaline electrolyte are

$$4H_2O + 4e^- \rightleftarrows 2H_2 + 4OH^- \quad E^0_{\text{red}} = -0.828 \text{ V vs. NHE},\tag{10}$$

$$4OH^- + 4h^+ \rightleftarrows 2H_2O + O_2 \quad E^0_{\text{ox}} = -0.401 \text{ V vs. NHE},\tag{11}$$

and in acidic

$$4H^+ + 4e^- \rightleftarrows 2H_2 \quad E^0_{\text{red}} = +0.000 \text{ V vs. NHE},\tag{12}$$

$$2H_2O + 4h^+ \rightleftarrows 4H^+ + O_2 \quad E^0_{\text{ox}} = -1.229 \text{ V vs. NHE}.\tag{13}$$

NHE is an abbreviation for normal hydrogen electrode, but nowadays the applied potentials can also be seen as reported against reversible hydrogen electrode (RHE) which does not take the pH into account making the RHE scale more convenient compared to the NHE scale. According to the following equation

$$\Delta G = -nF\Delta E,\tag{14}$$

where n = moles of electrons transferred in the reaction and F = Faraday constant, the electrochemical voltage ΔE_{cell} = -1.229 V of Equation (13) corresponds to the ΔG^θ of +237 kJ/mol.[13]

Water electrolysis for hydrogen production can be divided in four main types. In large-scale applications, the most common method is alkaline water electrolysis (AWE, Figure 1. a). In AWE, usually 30–40 % potassium hydroxide with Ni-coated stainless-steel electrodes are used. The alkalinity in the process is generated circulating the electrolyte across both electrodes, which are separated from each other with a porous diaphragm which allows the OH⁻ ions to pass through. The diaphragm is made of a ceramic oxide material. The operating temperatures for hydrogen and hydroxide production at cathode are moderate 65–100 °C and alkaline water electrolysis has a conversion efficiency of 60–80 %, with typical cell operating voltage being 1.8–2.4 V. The fact that the AWE does not require a catalyst to produce hydrogen is a significant advantage in addition to mild operation conditions such as low temperature. However, alkali solution used in the process causes relative strong electron corrosion. Similarly, proton

exchange membrane (PEM) electrolysers (Figure 1. b) operate in a moderately low temperature range of 70–90 °C producing high-purity hydrogen. In PEM, the electrodes used are mainly IrO_2 or RuO_2 at anode side and Pt at cathode side. In contrast to AWE, in PEM the electrolyte is a solid, for example Nafion© membrane (sulfonated tetrafluoroethylene polymer), which conducts the H^+ ions to form hydrogen molecules at the cathode making the electrolyte acidic in nature. This with the metallic surfaces of the electrode leads more rapid reaction kinetics compared to the alkaline cell. PEM electrolysers are generally safe, and the anode side can operate even in atmospheric pressure. The cathode side is, nevertheless, exposed to higher pressures. Due to the technical challenges PEM electrolysers are still difficult to scale up to large-scale applications.[14]
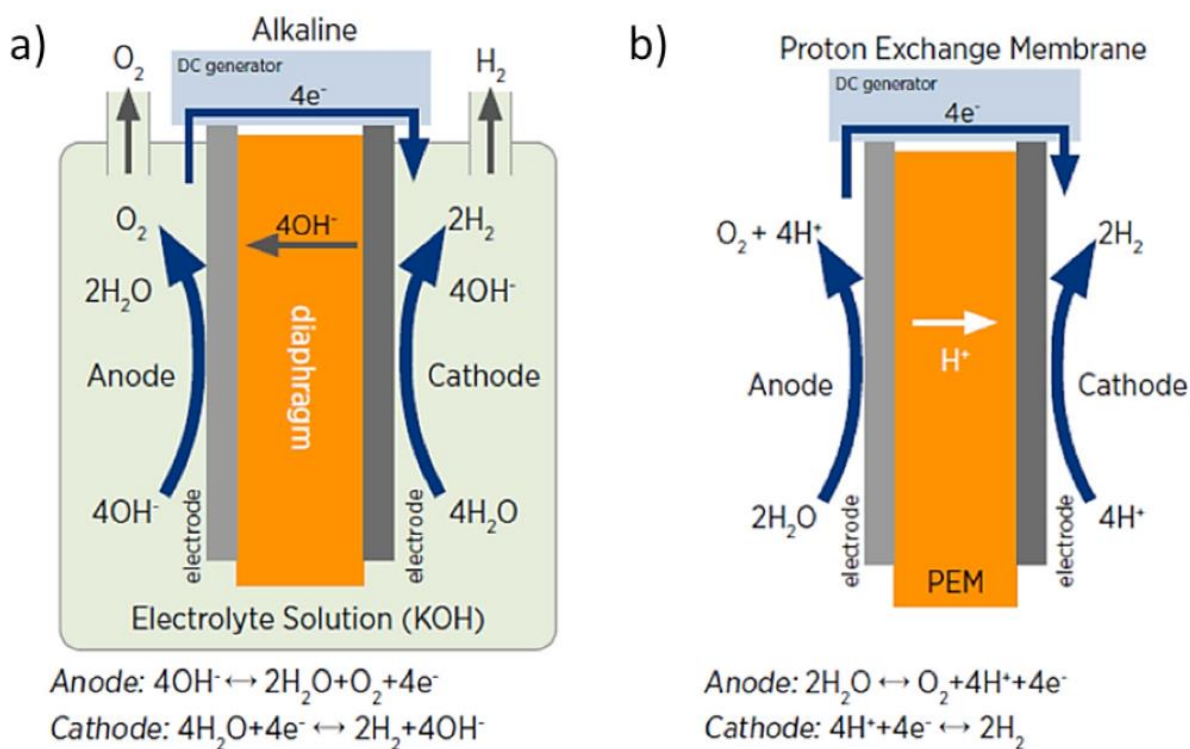

Figure 1. Schematic diagrams and reaction mechanisms of a) AWE and b) PEM electrolysers.[14]

The cells in solid oxide electrolysers (SOE, Figure 2. a) operate in a much higher temperature range (900–1000 °C) compared to the other water electrolysis types, but the hydrogen separation process requires less electricity. In SOEC (solid oxide electrolyser cell), the anode is usually perovskite-type material and Yttria-stabilised zirconia (YSZ) supported nickel is typically used as cathode. The heat can be applied to the cell for example by nuclear energy or waste heat to minimize the need of electric heating. In addition, the efficiency of the cell increases with an increase in temperature. As a downside, higher temperature reduces the

lifetime of the SOEC and causes rapid electrolyte degradation. The SOECs existing today can also be operated only at the kW-scale.[14]
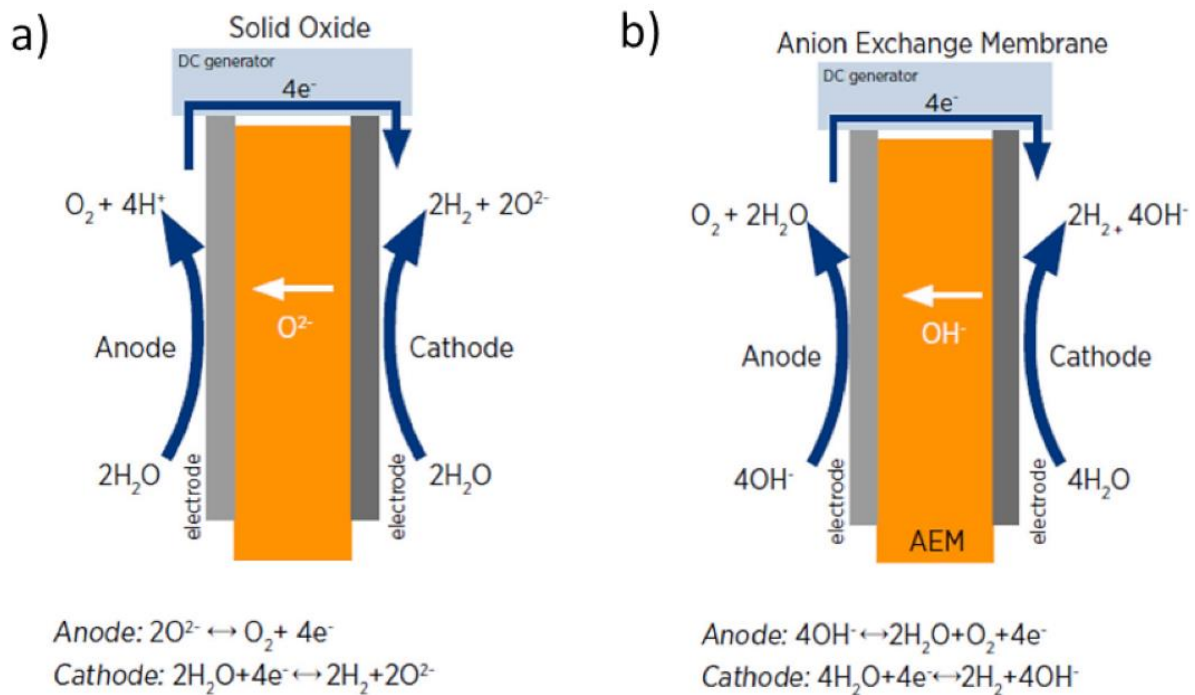

Figure 2. Schematic diagrams and reaction mechanisms of a) SOEC and b) AEM electrolysers.[14]

According to the literature, the most recent water electrolysis type, anion exchange membrane (AEM, Figure 2. b) electrolysers, combine many advantages of AWE and PEM. They also have significantly low operating temperature ranges of 50–70 °C. In AEM, the anode material can be Co_3O_4, the cathode is nickel, and electrolyte being a polymeric membrane supported with KOH or $NaHCO_3$. Both hydrogen and hydroxyl are generated on the cathodic side of the cell. The cost of the hydrogen production with AEM is low, for example due to the possibility of using non-noble catalyst materials. However, the poor catalyst activity and low conductivity diminish the AEM performance, and many aspects of the process still needs further investigations.[14]
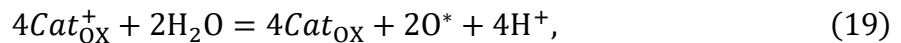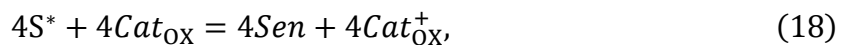
Thermolysis

Using extremely high, over 2000 °C temperature, it is possible to decompose water molecules directly to oxygen and hydrogen via thermochemical water splitting (thermolysis) using solar

or nuclear energy as a temperature supply. However, in these high temperatures the gases cause a severe risk of explosion and, therefore, the pure thermolysis is still under development. The temperature can be decreased with a help of auxiliary substances, which generate hydrogen or/and oxygen releasing intermediates. This kind of process is called thermochemical water decomposition and in its closed cycle the reagents can be recycled as the formation of intermediates and gas are integrated. The water splitting half reactions can be carried out with metal redox reactions using metal oxides such as ZnO, TiO$_2$, FeO and many others. It is also possible to add external energy to the cycle as electricity, which changes the water splitting type to a hybrid thermochemical cycle. In both methods, the high temperature, up to 3500 °C can be obtained for example by solar concentrating furnaces, which makes solar energy a very suitable source.[11]

Photolysis

In addition to using electric potential to break the bonds of a water molecule, some water splitting methods can include auxiliary substances (photosensitisers or photocatalysts) that can capture energy as direct sunlight (photons). Because photons by themselves cannot break the O-H-bonds of a water molecule, in a photochemical process, photons are used for electron activation. The simplest model of a photochemical hydrogen production cell is described in Figure 3. The photon absorbed into a photosensitiser can excite one electron per one photon to a higher energy state and the activated electrons can then be captured by water molecules and, as a result, activate them to higher energy states. This allows a further formation of hydrogen and oxygen atoms and the reactions of the photochemical water splitting process are shown in the following equations:

$$4Sen + 4hv = 4Sen^*, \tag{15}$$

$$4Sen^* + 4Cat_{\mathrm{R}} = 4Sen^+ + 4(Cat_{\mathrm{R}}^-)^*, \tag{16}$$

$$4(Cat_{\mathrm{R}}^-)^* + 4H^+ = 4Cat_{\mathrm{R}} + 4H^*, \tag{17}$$

$$4S^* + 4Cat_{\mathrm{OX}} = 4Sen + 4Cat_{\mathrm{OX}}^+, \tag{18}$$

$$4Cat_{\mathrm{OX}}^+ + 2H_2O = 4Cat_{\mathrm{OX}} + 2O^* + 4H^+, \tag{19}$$

$$4H^+ = 2H_2, \tag{20}$$

$$2O^* = O_2, \tag{21}$$

where *Sen* means sensitiser, h = Planck constant (6.626×10^{-34} J s), v = photon frequency, thus hv means a photon and its energy. *Cat*$_R$ and *Cat*$_{OX}$ are the catalysts for the reduction and oxidation reactions. Because one photon absorbed and activated by the photosensitiser is enough to reduce only one proton – when hydrogen molecules have two protons – a catalyst is used to accumulate the electrons for the formation of H_2. In a photochemical process, to split only water molecules rather than other possible compounds, catalysts are also required because of their capability to capture electrons from the negative valence oxygen atom of the water molecule.[11] Photocatalysts, as their name suggest, are a good example of light absorbing catalytic materials. As the electrochemical water splitting reaction includes two electron transfers, the ideal photocatalytic semiconductor material would be able to reduce and oxidise water molecules with photon generated holes and electrons. Electrolysis and photocatalysis can also be combined in photoelectrochemical water-splitting (PEC). In this method, an electrochemical cell is used with a light-absorbent electrode.[15] All the mentioned hydrogen production methods, their capital costs, efficiencies, and disadvantages are presented in Table 1.
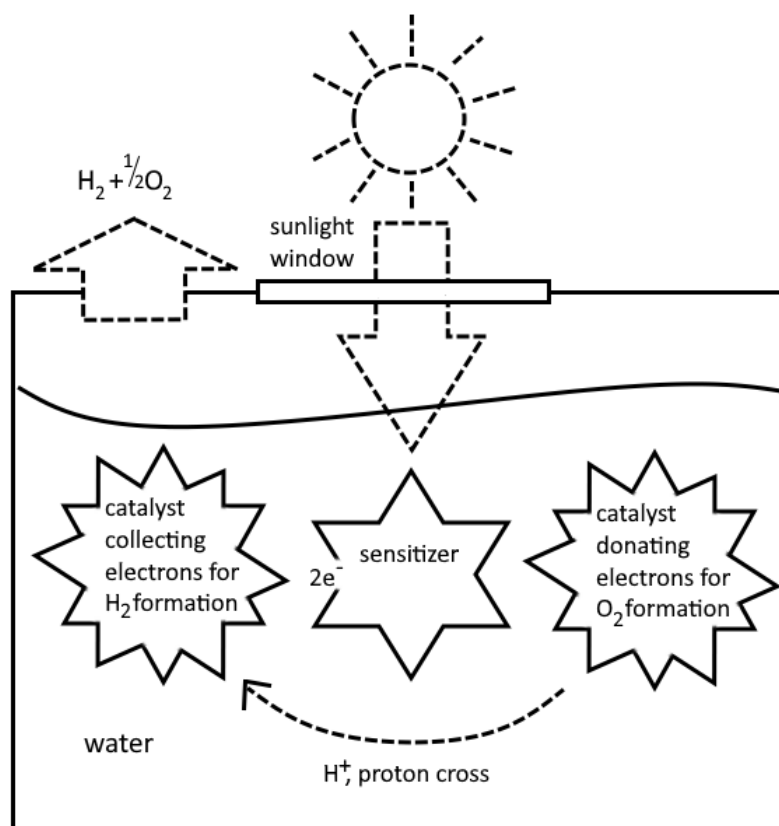

Figure 3. Components of a photochemical unit for water splitting. Drawn according to Wang *et al.* 2012.[11]

Table 1. A comparative table of different hydrogen production techniques, their capital costs, efficiencies, and main disadvantages.[9,14]

Technique	Hydrogen cost (€/kg)	Efficiency	Main disadvantages
Steam reforming	2.09 (with CCS) 1.91 (without CCS)	70–84 %	CO_2
Partial oxidation	1.50 (with CCS) 1.23 (without CCS)	60–75 %	CO_2
Autothermal reforming	1.36	60–75 %	CO_2
Biomass (thermochemical)	1.15–2.02 (pyrolysis) 1.62–1.89 (gasification)	35–50 %	Tar formation, seasonal availability, varying H_2 content, feedstock impurities
Biophotolysis	1.31–1.96	0.5–10 %	Low H_2-rates and yields, large reactor, O_2-sensitivity, expensive raw material
Fermentation	2.37 (dark) 2.69 (photo-)	60–80 % (dark) 0.1 % (photo-)	Low H_2-rates and yields, large reactor
Water electrolysis	3.82–21.41 (depends on the electricity source)	40–60 %	Low efficiency, high cost
Thermolysis	2.00–7.73 (depends on the electricity source)	20–45 %	High cost, toxicity, corrosive problems
Photolysis	9.54	0.06 %	Low conversion efficiency, non-effective photocatalytic material
Photo-electrochemical water splitting	More data required	-	Small production scale, low efficiency

3 Photoelectrochemical water splitting (PEC)

Already in the year of 1972 Fujishima and Honda reported the first photoelectrochemical cell for water splitting using TiO_2 as a semiconductor material and Pt as a counter electrode.[16] Compared to other hydrogen production methods, PEC is very advantageous in many ways. It does not require high temperatures or organic components which makes the system robust and easy to modify. In addition, as the oxygen and hydrogen are produced in two separate electrodes, the post separation of the gases is not needed.[13] As the system among the other photocatalytic techniques does not rely on external power source, it is also easy to distribute the hydrogen plants near the fueling stations or in geographically remote areas. This allows to avoid building expensive and complicated distribution and power transmission grid.[11]

In general, PEC cells include two separate electrodes submerged in an electrolyte, at least one of which is a semiconductor capable of absorbing light (photoelectrode), usually the photoanode being an n-type semiconductor and photocathode being a dark metal, such as Pt.[16,17] In contrast to n-type semiconductors, semiconducting materials can also be classified as p-type semiconductors, but they are rare and unstable, with generally too small band gaps.[15] Therefore, the principles of PEC in this thesis will be described using n-type system. The typical PEC water splitting system is described in Figure 4.
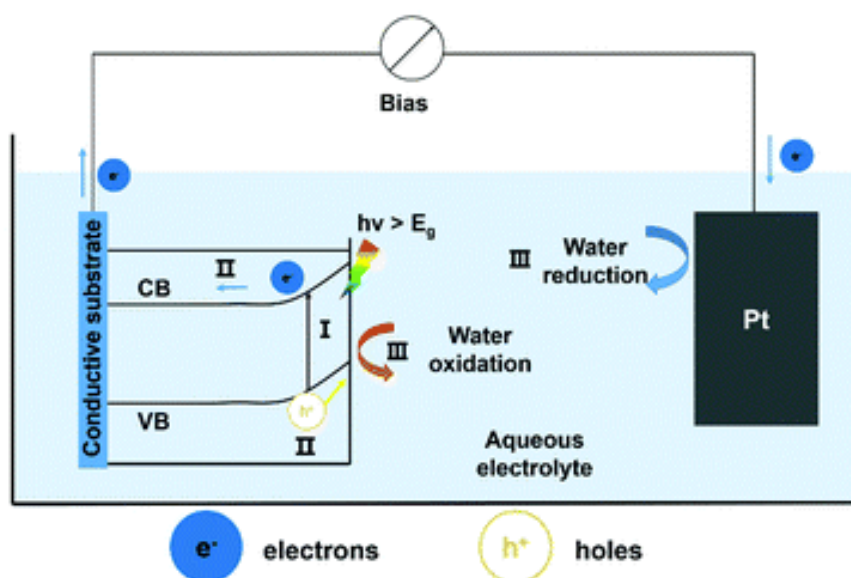

Figure 4. PEC water splitting system with n-type photoanode semiconductor with a Pt cathode. I) photon absorption, electron excitation and hole generation, II) electron-hole separation, III) surface redox reactions (Equations. 21 and 22).[18]

In the cell, electrodes are connected with a wire to form a closed circuit. As the photoanode absorbs photons, it generates electrons (e⁻) and holes (h⁺, regarded as unoccupied valence band states working as positive energy carriers) as shown by Equation 22 and Figure 4. I, which the electric field of the photoelectrode-electrolyte interface separates from each other (Figure 4. II).

$$2hv \rightarrow 2e^- + 2h^+, \tag{22}$$

where h = Planck's constant and v = frequency. Generated electrons migrate through the external circuit to the cathode and the holes at the anode/electrolyte-interface then split the water molecules to oxygen and hydrogen (Figure 4. III) as follows:

$$2h^+ + H_2O \rightarrow \frac{1}{2}O_2(g) + 2H^+. \tag{23}$$
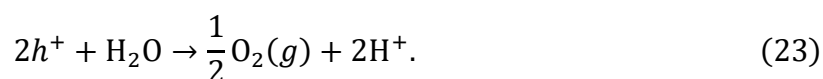
The generated H⁺-ions migrate through the internal circuit to the cathode and are then reduced by the electrons from the Equation 22. (Figure 4. III).[15,18]

3.1 Semiconductors

Semiconductors are solid materials consisting of 5×10^{22} atoms per cubic centimetre and they have an electric resistivity higher than metal and lower than insulator. In general, semiconductors have a crystalline structure, where atoms are arranged periodically forming a crystal lattice. For a more detailed description, the lattice can be thought of as containing lattice points, which all have similar surroundings and symmetry. The electric conductivity of a semiconductor can be modified by, for instance doping, optical excitation, injecting excess charge carriers and varying the temperature. Tunability enables the usage of semiconductors in a wide variety of different applications such as transistors and catalysts. The property changes due to the impact of temperature are one of the main characteristics of semiconductors: where the conductivity in metals decreases as the temperature increases, in semiconductors the conductivity does the opposite.[19]

The possible electron energy states in solid materials are called energy bands. The formation of the bands can be described with quantum theory or molecular orbital (MO) theory. The MO theory can be thought of in terms of a linear chain of atoms, which can be considered forming a one-dimensional solid. In this solid, a bond forms between atoms when their atomic orbitals overlap each other forming two MOs, which can be viewed as a linear combination of the two participating atomic orbitals. One of these orbitals is a bonding MO on a lower energy level

and the other is on a higher level, being called an antibonding MO. As the length of the linear atom chain increases, the number of MOs increases, and they gradually begin to overlap each other forming bands of allowed energy levels. Between these energy levels there are being left forbidden energy regions, which are formed from the atomic orbitals of the atoms, and are not involved in the MO formation, thereby can be thought of as localized atoms. The increase of the atoms in the linear chains eventually leads to a situation where the energy levels are so close to each other, that a fully delocalized energy band is being formed through the lattice.[20,21] This interaction between atomic orbitals is demonstrated in Figure 5.
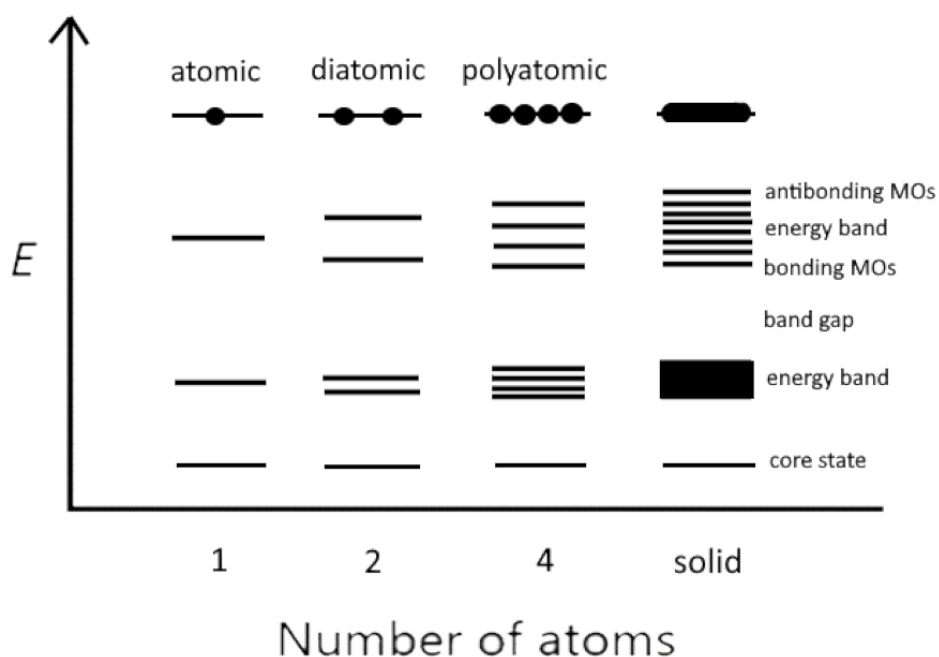

Figure 5. Schematic representation of the electron energy level diagram with gradually growing linear chain of atoms, where E is the potential energy. Drawn according to Kish & Horst 2014, and Brydson 2020.[20,21]

In addition to the previously mentioned conductivity-temperature relationship, one even more important property to be considered, when designing semiconductors to a certain application, is fundamental energy band gap (E_g). The band gap is a forbidden energy area between the allowed energy states, called valence band (VB) and conduction band (CB), of which the VB contains a high density of occupied energy states and the CB unoccupied states. In more detail, the energy band gap is located between the highest occupied molecular orbital (HOMO) of VB and the lowest unoccupied molecular orbital (LUMO).[22] In metals, electrons can be thought of as flowing without activation, because the VB and the CB overlap with each other allowing the electrons to move nearly freely between them. In a case of semiconductors, the conduction can

only be observed if the valence electrons can exceed the band gap energy (1–6 eV) and excite to the conduction band. For electrons to excite, an external energy is needed, and is usually applied as heat or light.[20]

In some of the common semiconductor materials, such as Si, the atoms from the 3s and 3p orbitals bond together covalently forming sp³-hybrid orbitals, which form the energy bands of the semiconducting material. However, in metal oxides the energy band formation is a bit more complicated due to the relatively high electronegativity of oxygen, which makes the nature of the bonds more ionic. As a more electronegative atom, oxygen tends to transfer its valence electrons to the metal atom, which makes the O-2p orbitals mainly the valence band. Thus, for example in TiO_2, primarily the Ti-3d orbitals become the conduction band (Figure 6).[13] In the band gap between the VB and the CB, there is located an electrochemical potential energy level called Fermi level. The Fermi level can statistically be thought of as the energy wherein the probability of the electron to be occupied on is 0.5. In a thermodynamic point of view, the Fermi level corresponds to the electrical potential of an electron in a solid. The location of the Fermi level varies depending on the purity of a material: in an ultrapure semiconductor Fermi level usually locates in the middle of the band gap, but when the material is doped with impurities either as electron donating or accepting atoms, the Fermi level is closer to the valence or conduction band respectively.[20]
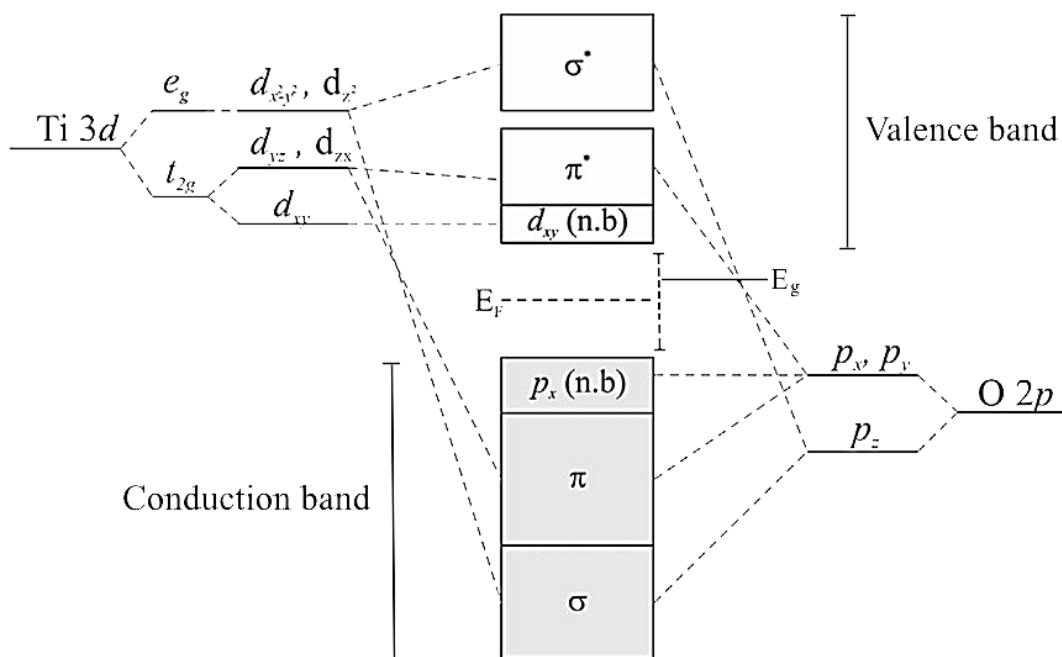

Figure 6. Molecular orbital energy-level diagram of an anatase TiO_2, where E_F is the Fermi level. Adapted from the article of Greiner *et al.* (2013).[23]

Optical properties

The band gap energy is possible to measure with photoelectrochemical and optical methods. The relation between the intensity of the light arriving to the surface and the intensity after passing through a transparent solid with a thickness of d (cm) can be written using Lambert-Beer law:

$$I_{tr} = I_0 e^{-\alpha d}, \tag{24}$$

where I_{tr} = Transmitted light, I_0 = Incident light and α = Absorption coefficient (cm^{-1}). With the absorption coefficient obtained from the Lambert-Beer law, it is possible to calculate the theorical band gap for a thin transparent layer as follows:

$$[\alpha(hv)]^{1/j} = A(hv - E_g). \tag{25}$$

However, because the semiconductors used in photocatalytic applications in general are not thin transparent films, but more of opaque layers or powders, the absorbent coefficient cannot be obtained with standard absorption techniques. Then, for example a diffuse reflectance spectroscopy (DRS) can be used.[20]

Considering the thermodynamics, a semiconductor suitable to work as a photoelectrode in PEC must meet three conditions. First, the minimum value of the edge of the CB must be more negative than the reduction potential of hydrogen 0.00 eV and secondly, the maximum value of the edge of the VB must exceed the oxygen oxidising potential 1.23 eV. Lastly, the absorbed photon should have an energy of 1.23 V or higher to be able to undergo a water-splitting reaction. However, to this date, no semiconductor has been able to meet all these thermodynamic requirements.[17]

To reach high enough efficiency for hydrogen production, light responsive material should also be able to absorb wavelengths of the visible light area (380–700 nm, 3.26–1.77 eV), because 43 % of the light coming from the Sun consists of visible light and only 4 % UV light.[24,25] In addition, visible light is more environmentally friendly and economic than UV-light.[22] Currently the efficiency of PEC is low, only approximately 16 %, because the band gaps in photoelectrode materials are relatively large, over 3.2 eV, hampering the use of larger wavelength portions of solar irradiance.[11] Because of all the above said conditions, the semiconductor elector band gap energy should ideally be between 1.6–3.1 eV.[17]

3.2   Efficiency and viability

There are a few important evaluating parameters for a water splitting process. When determining whether the used compound is electrochemically active, a Tafel analysis can be used. One indicator for the activity is current density (j_0), which is the absolute value of the current of the redox reaction on the catalyst-electrolyte interface at equilibrium potential (1.23 V at 1 bar and 25 °C). As briefly mentioned before, the water splitting reaction can initiate, when a higher potential i.e. the overpotential is applied and, thereby, a current can be observed. For simple electrochemical reactions, the relationship between the total current (j) and the potential of the redox reaction in both directions at the equilibrium potential (zero overpotential) can be represented by the Butler-Volmer equation:

$$j = j_0 \left(-e^{-\frac{\alpha \mathrm{n} F \eta}{RT}} + e^{\frac{(1-\alpha)\alpha \mathrm{n} F \eta}{RT}} \right), \tag{26}$$

where α = transfer coefficient, n = number of electrons transferred during the oxidation/reduction of a single molecule, η = overpotential (applied potential greater than the equilibrium in order to initiate the reaction and release the entity at the electrodes)[26], F = Faraday's constant, R = the universal gas constant and T = the absolute temperature. The Equation (26) is directly the sum of the half reactions, and it can be further modified on a case-by-case basis. At potentials close to the overpotential, Equation (25) transforms into a simpler equation:

$$j = j_0 - \frac{\alpha \mathrm{n} F \eta}{RT}. \tag{27}$$

Besides the activity, Tafel analysis is a useful tool also determining the reaction mechanism of an electrocatalysis, and it can be used at highly negative overpotentials. For water splitting, an optimal catalyst should show a low Tafel slope, but high current density. Figure 7 represents Tafel plots for some Co-doped MIL-53-NH_2 MOFs which Han et $al.$[27] synthetised in 2016. The MOF(Fe_1–Co_3)$_{550N}$ showed the best catalytic activity for OER with a Tafel slope of 72.9 mV dec^{-1} and a low overpotential of 0.39 V at 10 mA cm^{-2}. Overpotentials are useful when comparing the electrocatalyst activities and thus determining a good catalyst. To make the comparison as simple as possible, the same current density, usually of 10 mA cm^{-2} is chosen. The current density of 10 mA cm^{-2} also covers approximately 10 % of the efficiency of solar-to-chemical conversion. Tafel analysis is a unique method to study the activity and kinetics of a system at once, which no other method is capable of.[28,27]
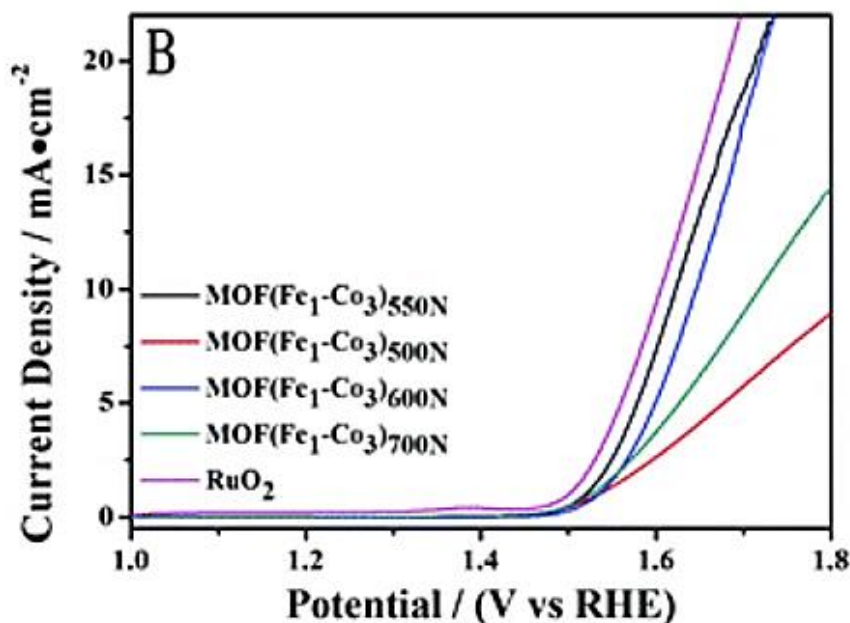
Figure 7. Tafel plots for MOF(Fe₁–Co₃)₅₅₀N, MOF(Fe₁–Co₃)₅₀₀N, MOF(Fe₁–Co₃)₆₀₀N, MOF(Fe₁–Co₃)₇₀₀N, and RuO₂.[27]

Especially in PEC, photocurrent density and incident photon to electron conversion efficiency (IPCE) are great factors determining the efficiency of a photoelectrocatalyst. The photocurrent corresponds to an electric current, but which is only generated with a photosensitive device and photocurrent density is a number of e^-/h^+-pairs collected per photon. The IPCE describes the conversion ratio of the incident photon to an electron as a percentage in a photovoltaic cell. In all simplicity, also the properties of the used electrolyte affect the photoelectrode performance. As shown in Equations (10–13), pH is an important factor affecting the electron affinity of cations. The nature of the electrolyte also affects the stability of the used electrode, which is another important parameter in water-splitting PEC.[26]

Because of the high oxidation potential, it is observed that compared to an acidic or neutral electrolytes the performance of a catalyst is the best in alkaline medium. The pH range sets challenges for efficient materials, and it is important to ensure that the used catalyst is chemically stable and, thereby, to make sure that the structure does not collapse, the compound does not dissolve, or form derived metal oxides during or after the electrochemical process. The stability, including mainly chemical, thermal, and mechanical stability, can be investigated via many methods including X-ray diffraction analysis, scanning electron microscopy and thermogravimetric analysis.[26] Due to the high oxidation potential, one of the highest performances of a catalysts today in PEC can be reached with UiO-66 metal-organic framework solutions. Metal-organic frameworks (MOFs) are a highly diverse compound group, which can

include even both, catalytic and light-harvesting components. MOFs have been used as cocatalysts alongside semiconductors to for example prevent electron-hole recombination, but they can also be used directly as photoelectrocatalysts and photocatalysts.[24]

4 Metal-organic frameworks

Metal-organic frameworks evolved from the fields of solid-state/zeolite and coordination chemistry. In 1960 developed coordination chemistry covers polymeric compounds, which are built from metal ions and organic linkers. Not until the year of 1995, the field took a significant leap in development, when Yaghi & co-workers popularized already in the earlier 1990 introduced term metal-organic framework. The main property, that distinguishes MOFs from regular coordination polymers, is their extremely high porosity, and thus the compound group increased interest in porous materials. In addition to extremely high porosity – even 90 % free volume – and flexible structures, the pores are also highly tunable with functionalities. These properties alongside many others make MOFs useful in a wide range of different applications, including catalysis, drug delivery, water treatment, chemical censoring, storing energy and producing solar fuels.[29,30,31]

4.1 Structure

By definition, MOFs consists of two different – organic and inorganic – secondary building units (SBU). The inorganic metal node or cluster connect di- or polytopic organic linkers with coordination bonds forming a net structure, usually via self-assembly[32]. Generally, any transition metal can be used as metal clusters forming MOFs, because their partially empty d-orbitals make them prone to form coordination bonds actively. The highly variable coordination numbers and oxidation states between different metals are one of the main features making MOFs' structures highly versatile. This enables many structural geometries such as square-planar, trigonal, tetrahedron, octahedron and so forth,[33,34] and as in fact, the Cambridge Structural Database[35] (CSD) has been added nearly 100,000 MOF structures in their collection to date.[36]

The organic ligands have an essential role in the structural dimensionality. The properties of the ligand, such as size, length and functionality affect the active site availability, interpenetration, and porosity of the framework. [37] A series of MOFs sharing the same topology, but different pore sizes are called by a term IRMOF (isoreticular metal-organic frameworks). One of the first synthesized MOFs was MOF-5, which belongs to a certain IRMOF-family. MOF-5 (IRMOF-1) consists of tetrahedral ZnO_4-clusters and terephthalate anions formed from terephthalic acid (benzene-1,4-dicarboxylic acid, BDC). The 16 different structures of the series can be obtained by lengthening the carbon chain of the terephthalate-ligand using for example 1,2-dihydrocyclobutylbenzene-3,6-dicarboxylic acid (CBBDC) and naphthalene-2,6-dicarboxylic acid (NBC).[38,39] These structures are demonstrated in Figure 8.
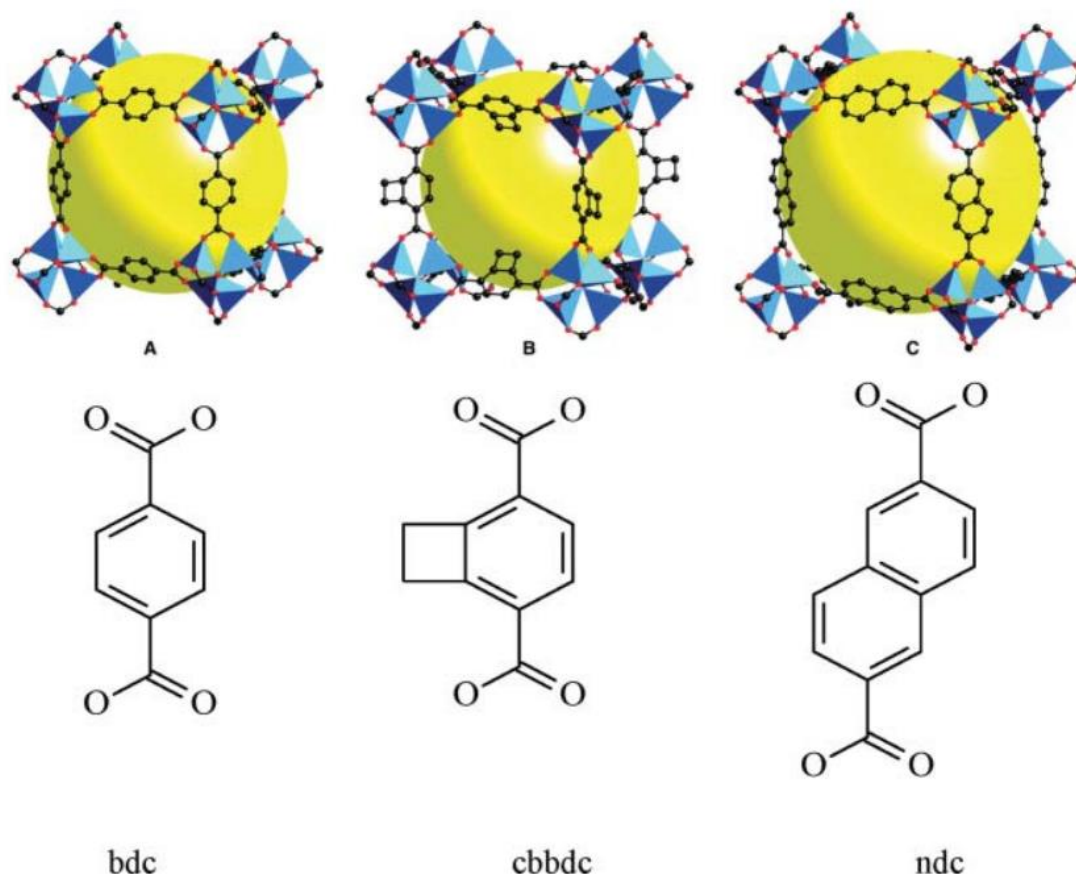
Figure 8. Structures of different MOFs in an IRMOF-series and their ligands. Structure A = IRMOF-1, B = IRMOF-6 and C = IRMOF-8.[39]

Carboxylic acid linkers, for example terephthalic acid, are very common building blocks in variety of MOFs. One photocatalytically active 3D-structure is UiO-66, and it is constructed of 12-connected $[Zr_6(\mu_3\text{-}O)_4(\mu_3\text{-}OH)_4(COO)_{12}]$ clusters and BDC^{2-}-ligands (Figure 9). The high

connectivity of the Zr-clusters exhibits extreme stability even in aqueous solutions in a wide pH range (0–12) for long periods of time, even months. The functionality in alkaline solutions enhances the catalytic performance of the compound. UiO-66's Brunauer-Emmet-Teller surface area is up to 1200 m^2 g^{-1}.[25]
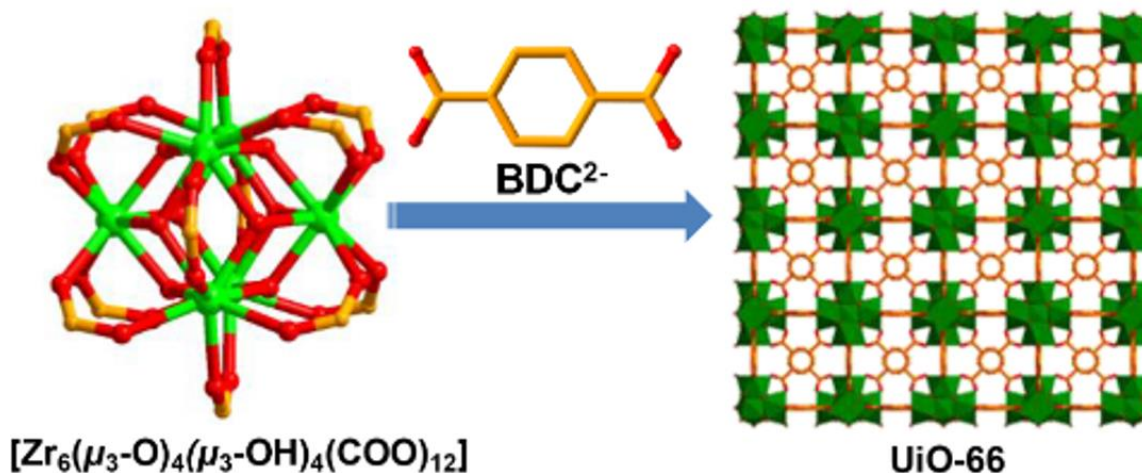

Figure 9. Synthetic procedure of UiO-66 by linking [$Zr_6(\mu_3\text{-O})_4(\mu_3\text{-OH})_4(COO)_{12}$] cluster and BDC^{2-} ligand.[25]

5   Synthesis methods

Usually, when synthesising a smaller amount of a MOF compound, a solvothermal or hydrothermal method can be used. In these reactions, an organic linker, and a metal salt in organic or aqueous solvent respectively are added to a closed vessel, for example a Teflon-lined autoclave which is heated up above the boiling point of the solvent causing a high-pressure environment to be formed inside. Solvothermal method is useful especially when processing sparingly soluble reagents, as the solubility increases with a temperature rise. In non-solvothermal method, the reaction takes place in standard air pressure and can be carried out for example with refluxing or precipitation.[30] Precipitation reactions are based on the supersaturated conditions of the reaction solution, where the components will self-assembly and crystallize in particles of tenths of nanometres to micrometres as different parameters are being changed.[32] With a cooling rate regulation, the nucleation, and therefore the crystal size can be controlled as solubility decreases in lower temperatures. A proper crystal growth can

also be achieved afterwards by for example a slow diffusion or a slow solvent evaporation. Slow nucleation, and thus a larger crystal size is preferred in the MOF characterisation.[30]

In addition to the conventional synthesis methods where the energy is introduced into the reaction as heat, the reactions can also be initiated using alternative energy sources. The need of alternative synthesis methods comes into play when specific features, such as morphology, material properties, or particle size cannot be obtained using conventional methods. Micro-waves (MWs) principally used in organic syntheses can also be used in MOF syntheses, especially when fast crystallization and small crystal size are desired. MW-assisted method is also used when temperature and pressure need to be strictly monitored.[30]

In sonochemical MOF synthesis, the energy is obtained from ultrasound. The ultrasound waves cause large pressure differences in the MOF solution creating bubbles, that release energy when bursted. This energy creates a high-temperature and high-pressure spots (4700 °C and 1000 bar) in the solution. Usually, an aqueous solvent is used in sonochemical reactions due to the high volatility of organic solvents. In mechanochemical synthesis, a mechanical force is used to break intramolecular bonds and does not necessarily require solvent at all. In a mechanochemical process, small particles can be evolved fast in a room temperature, for example in a ball-mill grinder. This method can be useful in metal oxide syntheses, because of their generally poor solubility.[30]

In order to take a MOF synthesis from academic world to industry, there are plenty of things to consider. When synthetising MOFs in a small scale for research purposes, the challenging environments, such as high temperature and pressure are easier to manage, and the prize of the reagents is less prominent. To synthesize MOFs in a larger scale, the reaction parameters and reagent costs must be moderate and even more importantly, with the climate goals and restrictions, the role of the renewable and recyclable materials must carry a main role.[30,40] The sustainability of MOF synthesis must be taken into account also when considering the ecology of the produced hydrogen.

5.1   Functionalization and post-synthetic modification

The high porosity of MOFs provides and large surface area for functionalization. Functional groups can be included into the structure during the synthesis as a part of organic ligands or afterwards by post-synthetic modification (PSM).[38] PSM is often included in a detailed design of MOFs because it enables a better control of the node-ligand combinations and including

properties, that are not possible to obtain with conventional synthesis routes. Therefore, PSM have opened new possibilities to use MOFs in a wide range of different applications, for example in the fields of catalysis, gas absorption and chemical sensors. The PSM often includes the modification of the ligand or metal node, which is attractive due to the labile nature of the metal coordination bonds or changing the quest molecules, of which the high porosity and thus a great accessibility provides.[37]

Metal-based methods

The most used metal-based modification methods of MOFs are transmetalation and metal doping. In transmetalation i.e., metal exchange, a new metal is introduced in the structure while breaking the old coordination bonds between the organic ligands and the original metal, which makes the method a very energy demanding process. Several factors influence the determination of a partial or complete metalation such as the lability of the exchanged metal, valence and coordination characters of the included metal, the used solvent, and the stability of the new modified structure. The stability, especially of a bivalent metal, can be predicted with Irving-Williams series, where the divalent first-row transition metal stability order would be $Mn(II) < Fe(II) < Co(II) < Ni(II) < Cu(II) > Zn(II)$. In transmetalation, only partial metal ion exchange has been accomplished and the equilibrium is usually reached quickly. Therefore, the solution containing the incoming metal ions should be replenished during the process for a more extensive exchange.[37] The transmetalation in practise can be very simple. In 2015 Lv et $al.$[41] soaked cadmium MOF crystals into cobalt and copper containing solutions. After keeping the parent MOF in a Cu-solution for 216 h, the Cu^{2+} content in the structure was increased by 66.6 % and with the same parent structure, after immersing it in the Co-solution for the same amount of time, 29.3 % of the Cd^{2+} ions had been exchanged with Co^{2+}. This also suggests that the Cu-based framework exhibits higher stability due to the Jahn-Teller effect of Cu-ions.

Metal-doping can be carried out with involving the additional metal complex or ion into the open channels or by a direct coordination. The changes caused by an additional metal can be drastic, as entirely new connections may form in the structure. For example, in 2015 Yuan et $al.$[42] synthetised a bimetallic MOF by introducing nickel nitrate in DMF to the Zr-MOF, PCN-700, where $[Zr_6O_4(OH)_8(H_2O)_4]$ clusters are 8-connected via Me_2-BPDC (2,2′-dimethylbiphenyl-4,4′-dicarboxylic acid) ligands leaving eight terminal -OH^-/H_2O-ligands free for metalation. As Ni^{2+}-ions were added into the terminal ligands, the carboxylate linkers

migrated forming bridges between Zr and Ni through the O-atoms by breaking the original Zr–O bonds and creating the new Zr–O–Ni bonds (Figure 10).
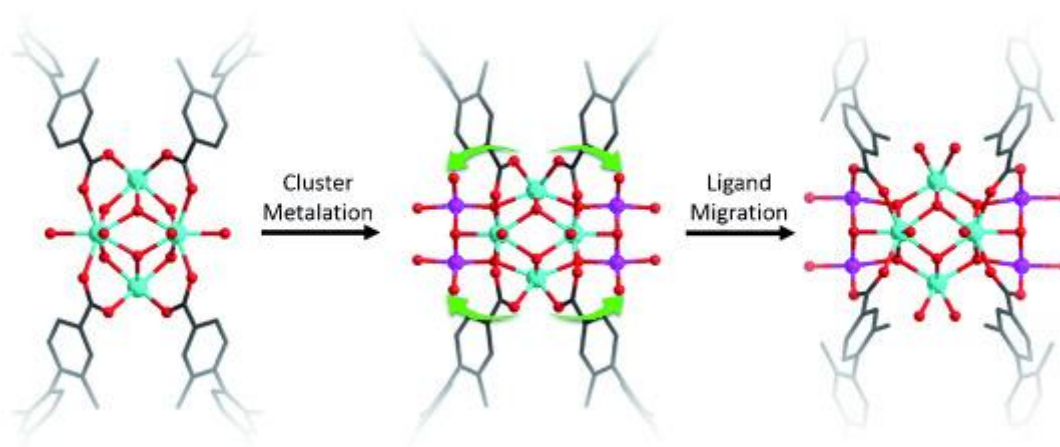

Figure 10. The ligand migration in PCN-700 resulted from the cluster metalation with Ni^{2+}.[42]

It has been shown that doping MOFs with different particles can improve the visible light absorption. For example, the incorporation of Au nanoparticles (NPs) into the light harvesting material, can increase the capability to absorb visible light due to the surface plasmon resonance, which enhances the electron transfer to LUMO orbitals.[25] In 2016 Zhang *et al.*[43] grew Ti-based MOFs, MIL-125 and NH_2-MIL-125 on the surface of TiO_2 nanowires constructing core-shell hybrid composites. In addition, Au NPs were included into the TiO_2/NH_2-MIL-125 nanocomposite forming TiO_2/NH_2-MIL-125/Au composite for PEC water splitting (Figure 11). The resulting material showed stabilized photocurrent of 30 μA cm^2 at a bias of 0.75 V *vs*. RHE, which was almost 50 % better compared to the non-doped TiO_2/NH_2-MIL-125.
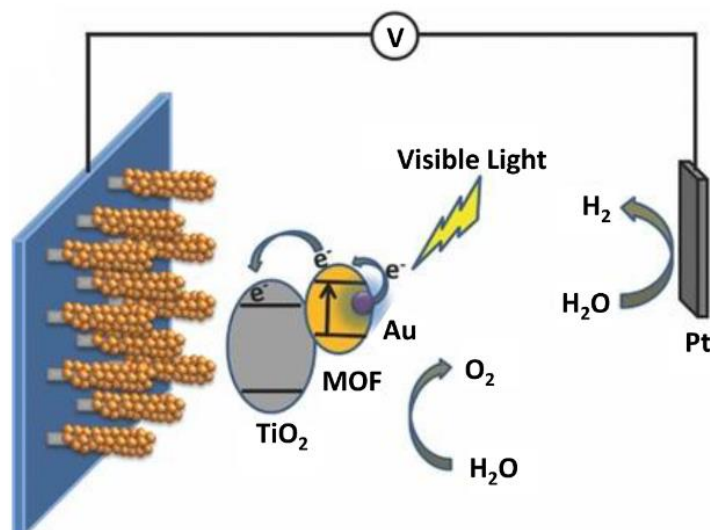
Figure 11. PEC water splitting device with TiO_2/NH_2-MIL-125/Au photoanode and Pt cathode under visible light illumination.[25]

In addition to transmetalation and metal doping, a less used post-synthetic metathesis and oxidation (PSMO) can be useful, when synthetising labile, high valence state metal-ion containing MOFs. In that method, a framework template with labile metal bonding can be used for metal exchange with the desired metal in an inert environment, followed by oxidation to a certain oxidation state.[44]

Ligand-based methods

Even if ligands are the backbone of MOFs, they can be completely replaced in PSM, but also only the functional groups of the ligands can be modified, especially when the original structure is to be preserved. With ligand modification, it is possible to bring new catalytic sites into the structure creating heterogeneous compounds, which can be highly beneficial in terms of hydrogen production in PEC. Compared with homogeneous MOFs, the heterogeneous structures have many advantageous qualities, such as better stability and efficient recycling. In 2019 Wang et al.[45] introduced a catalytic hydrogenase biomimetic site Fe_2S_2 into a UiO-type, $[Ru(BPy)_3]^{2+}$-derived MOF – constructed of $ZrCl_4$ and trifluoroacetic acid – by a click-reaction shown in Figure 12. Click-reactions usually refer to a cycloaddition reaction between azide and alkyne[46], but as Wang et al. proposed, the reaction can be expanded to different applications. Fe_2S_2 mimics a biological [FeFe]-hydrogenase enzyme, which can produce hydrogen by a

highly efficient proton reduction. The click-reaction resulted in a new HER-catalyst UiO-MOF-Fe_2S_2, which shows improved stability in water, compared to its analogues.[45]
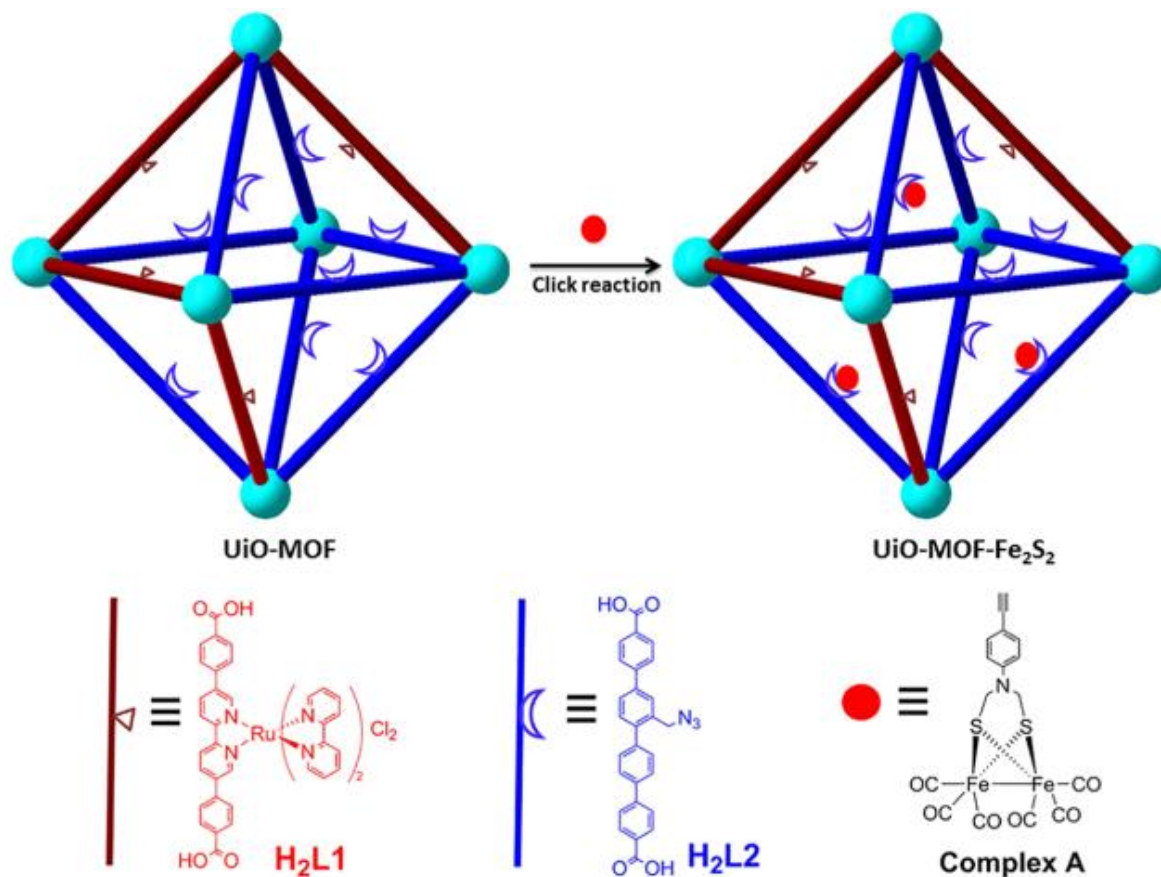

Figure 12. Click-reaction modification of UiO-MOF to construct new catalytic UiO-MOF-Fe_2S_2.[45]

The covalent bonding via click-reactions can show improved stability in comparison to more labile coordination bond-based links. However, if the aim is to obtain a new structure with similarities with the parent structure, or for example different dimensions, the ligand exchange method can be used for replacing ligands of a labile MOF. For a successful replacement, various aspects must be taken under consideration. These can be the thermodynamics, kinetics, and thus the stability of the structures, functionality and the size of the replacing ligand, and reaction conditions.[45] In 2016, Johnson *et al.*[47] incorporated a well-known OER catalyst [Ru(TPy)(DCBPy)(H$_2$O)](ClO$_4$)$_2$ (TPy = 2,2′:6′,2″-terpyridine, DCBPy = 2,2′-bipyridine-5,5′-dicarboxylic acid) into UiO-67 MOF, built from $Zr_6(O)_4(OH)_4$ clusters and BPDC-ligands (BPDC = biphenyl-4,4′-dicarboxylic acid), and the resulted MOF thin films were grown onto a functional electrode. As 6.43 % of the ligands were exchanged, the real concentration of the

catalyst was increased significantly compared to a theoretical monolayer, which can be beneficial for the diffusion and catalyst efficiency.

When controlling the exchange rate, one main thing to consider is the pK_a-value of the ligands. It has been shown that the kinetic rate of the exchange increases with the increasing acidity of the incoming ligand. On the other hand, in a ligand exchange, the sites wherein the exchange occurs is impossible to control. However, the post-synthetic ligand installation where a secondary linker can be installed to a predetermined site without modifying the structure, can overcome this problem.[37] In 2016, *Yuan et al.*[48] installed ligands with different lengths and functionalities to a PCN-700 framework creating variation to the pore size and pore environment in mild conditions. First, they had to synthetise the parent structure with predesigned missing linker sites, which was possible under kinetic control. The terminal OH^-/H_2O-ligands of adjacent $[Zr_6O_4(OH)_8(H_2O)_4]$ clusters were replaced by linear carboxylate linkers resulting eleven different mixed-ligand structures, each with three functionalities. For example, when sequentially installed, DCBPy and TPDC-R_2 (terphenyl-4,4″-dicarboxylate, R = Me, Ph, or Hex) can work together in the PCN-700 framework. The open bipyridine is used for binding a copper atom forming a metalated, size-selective MOF-catalyst for aerobic alcohol oxidation and tpdc-R_2 controls the accessibility of metal centres for substrates. The installation processes also resulted in increased H_2 absorption capacities, even by 57 %. The opposite of ligand installation is ligand removal, and it can provide a formation of defective MOFs, which are in the spotlight of catalytic MOF research due to the various applications.[37]

The porosity and pore size of MOFs are easy to modify and often the frameworks provide a wide range of under 2 nm micropores. Many applications of MOFs, such as gas absorption, separation, and censoring benefit from a small pore size, but considering PEC, the micropores are too small to transport large reactants and products between the liquid electrolyte and the redox sites on the surface, Mesopores (2–50 nm) suitable for PEC and macropores (>50 nm) can be accomplished by a partial removal of the ligand from the framework. This requires a usage of two different types of ligands with different stabilities against certain conditions, such as high temperature, light, and chemicals. The ligand, which of the two is more prone to react under the used conditions, can be removed for example by thermolysis, photolysis or acid treatment respectively. When a size-control of the mesopores is needed, a mixing ratio of the different ligands or the amount of the exposure of used factors can be varied.[31]

The removal of ligands requires labilisation of a pro-labile ligand in a framework, which also includes a non-labile ligand that remains in the compound. The labilisation can occur for

example through hydrolysis or thermolysis, and the ligand can then be washed out of the structure with a suitable solution.

Guest-based methods

Generally, the pores of the MOFs are occupied by guest molecules, such as ions, solvents, and additional molecules from the synthesis. Exchanging the quest may, for example, improve the electrostatic field in the cavities, which enhances the binding of H_2 in hydrogen absorbing MOFs. To reach more accessible pore volume in the framework, the guests can be removed and replaced in various ways. If an anionic MOF contains cations as extra-framework ions, their exchange, for example, to reach higher gas absorption properties, is relatively easy thermodynamically and kinetically. In 2007, Long & Dincă[49] were – at least to their knowledge – the first ever attempting to vary the quest cations in an anionic host MOF $Mn_3[(Mn_4Cl)_3(BTT)_8(CH_3OH)_{10}]_2$ (H_3BTT =1,3,5-tris(tetrazol-5-yl)benzene). The aim was to increase the H_2 absorption energy with metal-H_2 binding. Crystals of the MOF were immersed in concentrated metal chloride solutions containing the wanted guest cation and the soakings lasted for 1 month with three solvent refreshings. Then, the residual free cations were removed by rinsing and soaking the cation-exchanged crystals in distilled methanol. In the experiment, the large observed Cu/Mn and Zn/Mn ratios suggested that in addition to the expected extra-framework cation substitution, also intra-framework substitution did occur. The exchanged crystals maintained the crystalline structure of the parent MOF. Anion exchange is more complicated, but for example modulator formate ions have been reported to be exchanged with chloride and sulfate ions using HCl and H_2SO_4 respectively. In these exchanges, the MOF functions as an esterification reaction catalyst.[37]

When aiming to generate exquisite properties to a parent MOF, quest incorporation can be a useful method. Quest molecules can be attached to a framework as a solvent or as a reactive molecule. With the guest incorporation, it is possible to for example lower the optical band gap. In 2017, Guo et al.[50] π-intercalated an electron rich tetrathiafulvalene (TTF) guests between the napthalenediamide (NDI) ligands of a MOF-74 lowering the band gap by 1 eV (Figure 13).
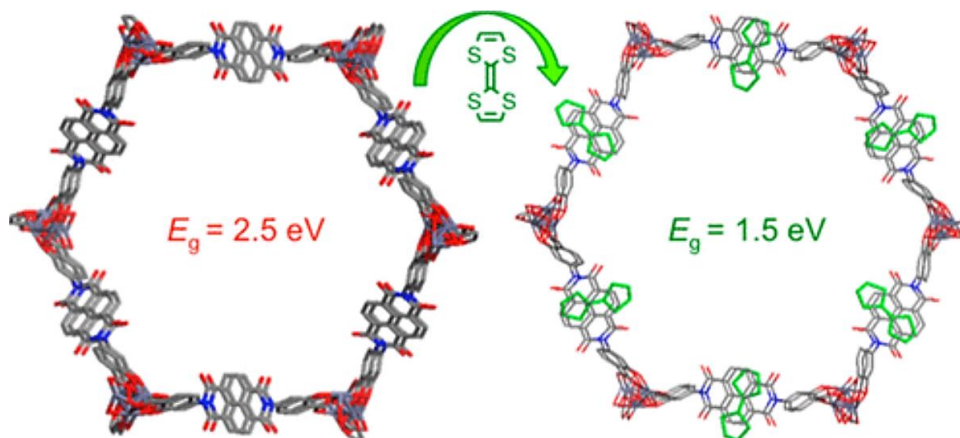
Figure 13. The π-intercalation of electron-rich TTF molecules in between the electron-deficient NDI moieties constructing a MOF-74 analog.[50]

5.2 Characterisation

X-ray diffraction

When analysing a crystalline solid at atomic resolution, the most accurate and detailed information of the structure can be obtained using single crystal X-ray diffraction (SCXRD). X-rays can be produced in a vacuum chamber containing a tungsten filament cathode with negative potential and normally a ground potential anode. By heating the cathode, electrons are produced, and they are accelerated by an electron field and collided into the water-cooled anode. The collision causes an energy loss, where the majority of the energy of the electron beam is emitted as heat, but a small amount – less than 1 % – is converted to x-rays. The emitted x-rays have different wavelengths depending on which electron shell the incident electron has ejected the electron from in an atom. Therefore, for an efficient use in characterisation, a monochromator is used to eliminate the unwanted wavelengths.[51]

In a crystal structure, atoms can be thought of as situated on lattice planes, located at a constant distance from each other. When the monochromatic beam – commonly Cu Kα radiation (1.5418 Å) – hits the sample, the diffracted constructively interferenced X-rays from multiple crystal planes satisfying Bragg's law (Figure 14), formulated by W. L. Bragg in 1913, can be detected to form a diffraction pattern in a function of diffraction angle. This law helps to relate

the wavelengths of the scattered x-rays to the atomic plane spacing in a crystalline material and can be written as

$$n\lambda = 2d \sin\theta , \qquad (27)$$

where n = order of reflection, which is an integer. The order of reflection is equal to 1 when the incident and scattered waves have one wavelength path difference (first order reflection) and larger than 1 in higher order reflections. λ = measurement wavelength, d = the separation of the crystal planes, and θ = the angle, where the beam hits a lattice plane and the constructive interference of the reflection from multiple parallel planes is satisfied (Bragg angle). It is important to notice, that in this case, the word reflection does not mean the classical optical reflection: The diffraction of the x-rays from the crystal planes is only analogical with a surface light reflection effect. [51,52]
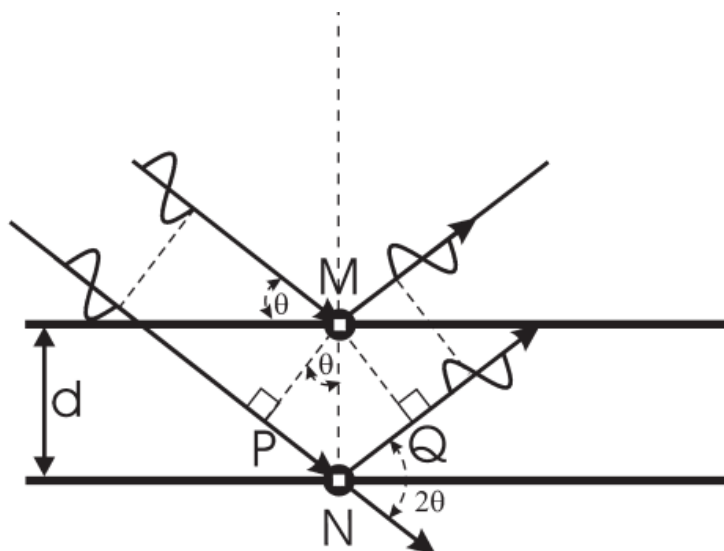
Figure 14. Illustration of the geometry used for the simplified derivation of Bragg's law.[53]

Occasionally, growing high-quality single crystals can be tough and a time-consuming task due to, for example, a rapid nucleation. Therefore, in many cases, the MOF-solids exist in a powdery form. Powder X-ray diffraction (PXRD) is an alternative method for SCXRD when single crystals cannot be obtained, but it also provides considerably less information. However, especially when characterising known compounds, PXRD is a fast and useful method and has earned its place as the most used qualitative analysis method for characterising powders.[54]

Usually in a PXRD measurement, the X-ray detector moves around the sample and the recorded diffraction peaks are the detector positions as an angle 2θ. Correspondingly, the recorded peak intensities in the diffraction pattern come from the counted number of X-rays in each angle.[55]

After the diffraction pattern has been constructed, it usually needs to be compared with reference patterns for a compound phase identification. These references can be simulated from SCXRD data and can be retrieved for example on Cambridge Structural Database[35] or directly on the local user-database implemented in the software attached to the computer from which the diffractometer is operated.

Thermogravimetry

One widely used and relatively simple method for gathering more information about the chemical composition of solids is thermogravimetry (TG). In thermogravimetric analysis (TGA), the sample is heated – typically at a constant rate – in a controlled environment and the characteristic gradual mass losses for a particular sample are followed. The mass losses are usually due to desolvation, thermal decomposition, or reactions with the measurement atmosphere. From the mass losses and the temperature where they occur, it is possible to determine, for example possible solvent residues, the bonding of metals and ligands, formation of undesired by-products during the synthesis and many other things. However, these determinations usually need additional analysis methods. Differential scanning calorimetry (DSC) measures the energy flow – usually heat flow – into or out of the sample and thus, gives a good insight about transitions occurring in the observed heating range and can reveal for example melting, burning, re-crystallisation or even glass transition processes. DSC is commonly utilized as a simultaneous analysis method with TGA for a more comprehensive information about the properties of the compound. Additionally, thermogravimetry-mass spectroscopy (TG-MS) and thermogravimetry-infrared spectroscopy (TG-IR) are useful hyphenated techniques, when gases are evolved during the degradation, and they are to be identified. Thermogravimetric analysis is well suited for exploring a wide range of practical properties, such as material composition and lifetime, heat tolerance and humidity content.[56]

Scanning electron microscopy

When synthetising MOFs directly on an electrode material, it is crucial to investigate the coated surface in more detail. For visual information on the surface topology, MOF distribution, and the shape of the crystals, a scanning electron microscopy (SEM) can be used. In SEM, high-energy electron beam from, for instance, a thermal source is applied on the surface of the

sample, and it interacts with the surface atoms. To obtain a sharp image, the electron beam spot is compressed and directed with lenses creating a spot size less than 10 nm. The incident electrons excite the sample atoms, from which the emitted secondary and backscattered electrons are detected on the electron detector. The signals are displayed on a computer screen, where a magnified image of the 3D-surface of the sample can be viewed. Altering of the electron accelerating voltage affects the penetration depth of the electrons through the sample.[57] A scanning transmission electron microscopy (STEM) mode can be used in SEM analysis. In STEM, the images are generated by the transmitted electrons providing sharper images.[58]

As an important addition to scanning transmission electron microscope, an elemental mapping extension can be helpful when the proper chemical composition of the desired MOF cannot be investigated with other techniques, such as PXRD. The invisibility of the MOF coating in PXRD is not unusual, as the thickness of a MOF layer is generally relatively small compared to an electrode whose atoms are dominantly visible in the measurements. With elemental mapping, usually using electron energy loss spectroscopy (EELS) or energy dispersive X-ray (EDX) function, the chemical composition of a specimen can be obtained from characteristic signals of different elements. EELS has offered an elemental mapping at atomic resolution already since the early 1990's. However, the small detector size with a small collection angle makes the interactions between the probe and the material nonlocal, complicating the interpretation of the map. Compared to the STEM EELS, the inelastic interaction using STEM EDX is effectively local. The detector of an EDX is large covering the whole solid angle.[59]

6   MOFs in PEC

Many characteristic properties of MOFs make them great materials for PEC. High crystallinity reduces the electron-hole recombination by suppression of defects in the lattice and the interface between two grains of the structure improving the electron transportation. The porous structure provides also more surface area for active sites. A small particle size enhances easier transport of holes and electrons to the surface, but when going to too small particle size, the electron-hole recombination is enhanced in turn. For this reason, a large crystal size is desired in the synthesis, in addition fo a better characterisation of the compound. As all of these characteristic properties of MOFs have a positive effect to the electron transfer, they exhibit great

overpotentials and appropriate Tafel slopes in water splitting. In addition, the integration of MOF to PEC may also improve and broaden the light absorption. Based on the functions of the MOFs used in the system, they can be categorized as precursors, photosensitizers, co-catalysts, counter electrodes, or stability increasers.[18,26]

Carboxylates are widely used linkers in MOFs for PEC. To form a stable MOF, these hard Lewis base ligands with low pK_a values form strong interactions with metals which function as hard Lewis acid found in high-valent main group and transition metals, such as Al(III), Fe(III), Cr(III) Ti(IV) and Zr(IV). Even if high valence metals are favoured building blocks in MOFs, also low valence metals can be used, but they form only weak coordination bonds, and thus exhibit weaker stability. This problem can be avoided introducing hydrophobic functional groups to the organic ligand, which affects decreasingly to the water and moisture affinity of the structure, thereby increasing the stability.[25] For example, in 2011 Yang *et al.*[60] introduced a methyl group to the BDC^2-ligand of a MOF-5 and showed the resulting structure to be more resistant towards water than the parent MOF.

6.1   Engineering the band gap

Previously, PSM of MOFs has been discussed on a general level, but a more detailed look into the band gap engineering plays a crucial role in achieving efficient structures for light absorption. In 2014, Butler *et al.*[61] calculated the energy band diagrams for variety of MOFs including MOF-5, HKUST-1, ZIF-8, and MIL-125. The calculations revealed that most MOFs exhibit a relatively large, over 3.0 eV E_g, which cannot absorb light from the visible light area. Even if classic PSM offers several powerful methods to improve the photocatalytic performance of MOFs, the modulation nature of the electronic properties such as band levels and optical absorption are still poorly understood, and the semiconductor properties of MOFs have not been able to be completely defined. However, it is reported that the light harvesting abilities of MOFs are mainly affected by the photoabsorption of the ligands, which is further affected by the metal ions and cluster varieties and coordination. Therefore, almost all modulation techniques optimising and lowering the band gaps are based on either the ligands or the metal nodes.[62] In 2014, Volkmer *et al.*[63] gathered several strategies for decreasing the band gap energy. For achieving higher energy level VB, the degree of the conjugation of the linker should be increased and for lowering the CB energy level, the chosen node metal should

possess partially unoccupied *d*-orbitals. Finally, electronic rich fragments can be placed into the nodes.[62]

In MOFs, the level of the CB depends on the node metal coordination. The VB height – thus the band edge and the width of the band gap – can be modified without changing the topology by elongation and introducing different functionalities to the ligand, or with mixed design of the ligands.[24,31] Gascon *et al.*[64] (2008) synthesised terephthalic acid-based IRMOFs with increasing resonance effect and conjugation between the ligands and then determined the band gap energies of the structures with UV-VIS spectroscopy. The functional groups were selected by the unshared electron pairs participating the resonance effect (bromine) or by the hyperconjugation effects (aromatic rings). As they expected, the band gap energies decreased dramatically with the increasing resonance effect and conjugation of the ligand (Figure 15).
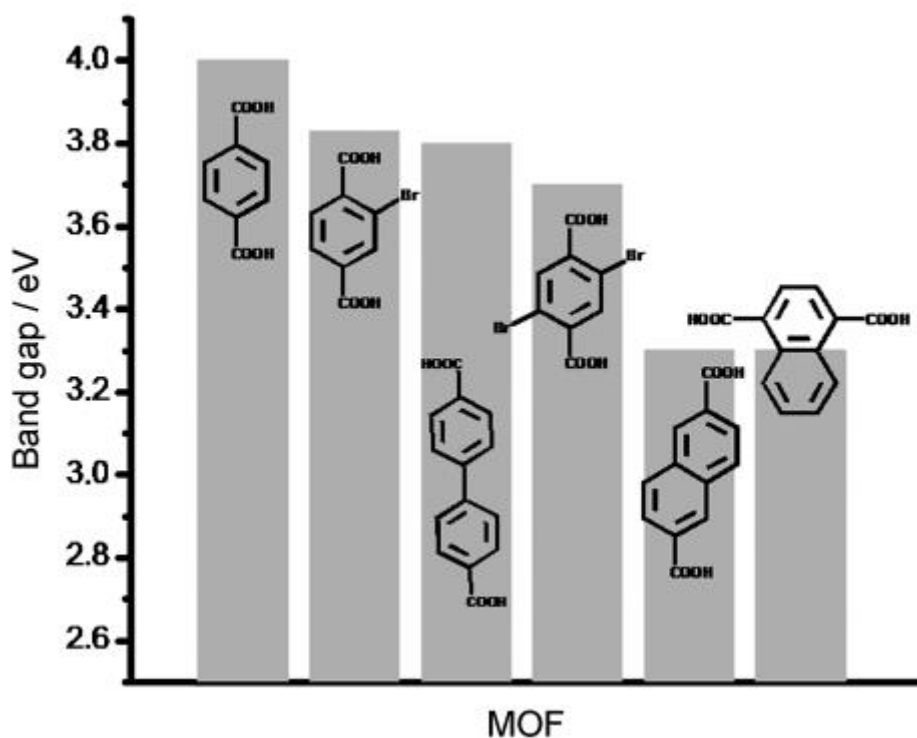
Figure 15. Different ligands used in MOFs with decreasing band gap energies.[64]

By decorating organic ligands with functional groups, for example hydroxyl, amino, nitro and halogen, it is possible to reduce the band gap energy and redshift the light absorption edge. This is due to the changes in electronic densities, which also leads to an improved hybridisation with the metal ions.[62] It has been shown, that for example the increasing number of NH_2-groups shifts the valence band maximum (VBM) upwards, which narrows down the band gap. For example, MIL-125 has been reported to have a band gap energy of 4.08 eV, whereas the NH_2-

functionalized version, MIL-125-NH$_2$, has a significantly smaller band gap of 2.68 eV. This is due to the lone pair electrons of the nitrogen, which facilitates the absorption of visible light. Based on calculations, it is also proposed, that the best band energy structures for PEC could be achieved by an optimized mixing of two different ligands, but this still needs more experimental confirmation. In band gap engineering and electronic properties, also conductivity, stability, charge carrier separation and migration, charge carrier lifetime and structural properties, such as morphology and porosity must been taken under consideration.[31,62]

In addition to linkers, metal node engineering plays an important role in band gap tunability by modifying the conduction bands. Metal nodes are also a crucial building block of MOFs, as they offer reactive sites in catalyses and connect the ligands. It has been verified with density functional theory (DFT), that by increasing the size of the inorganic node the band gap can be significantly decreased. Another feature having different effects on the band gap, is the type of the metal.[62] In 2009, Kang *et al.*[65] reported that changing the metal ratio between Zn^{2+} and Co^{2+} ions in case of IRMOF-1, band gaps ranged between semiconducting to even metallic states. Higher the percentage of Zn ions were substituted with Co, the more metallic character the structure showed. This phenomenon can be explained with partial density of states. As the amount of cobalt increases, the overlap between Co and Zn *d*-orbitals and the O and C *p*-orbitals increase, thus decreasing the band gap. The increase of the overlap is a result of the lack of empty *d*-orbitals of Zn, and Co having an empty *d*-orbital allowing electron donation from the O p_π-orbital to the Co d_π-orbital. In addition to these common methods for tuning the band gap, also fine-tuning the ligands and doping nodes can be used for MOFs with a moderate light-harvesting abilities.[65]

6.2 Charge transport and conductive MOFs

The ability to generate electrons and holes via visible light in MOFs does not afford as an efficient charge transport and systems with slow transport across the electrode-electrolyte interface in PEC are prone to electron-hole recombination. Even if MOFs consist of conductive metal nodes, the insulating organic ligands and the high porosity makes the wide-range charge carrier transport and the electric conduction more complicated. However, both ion- and electron conductive MOFs (C-MOFs) have shown significant progress on this issue.[31] In practise, it is difficult to distinguish the charge transport mechanism of MOFs, but they are generally known

pathways, and the knowledge of them helps to build a suitable structure for certain applications.[66]

In MOFs, the conduction can occur through bonds, through space, via extended conjugation, via quest molecules or as redox hopping. The pathway through bonds consists of the orbitals from the metal and ligand functional groups (Figure 16 a), whereas in through-space pathway the charge transports via π-π bonds of the organic units (Figure 16 b). Determining the through-bond conduction, it is important to consider the overlapping of the orbitals. For example, the ionic bonding between metals and carboxylate ligands do not establish a significant overlapping, but using azolate linkers, the overlapping and the conduction improves. An example of conductive azolate-including 3D-networks are Fe-azolate frameworks (Fe-N-N)$_\infty$ with controlled multivalency of Fe(II/III). In 2021, iron was reported to be the most effective multivalent metal for C-MOFs, and the conductive nature of a framework including multivalent Fe could be modulated with controlling the [FeII]/[FeIII] -ratio. This can be done, for example by additives or redox reactions. In addition to metal redox pairs, also organic linker redox pairs can improve the conductivity.[31]
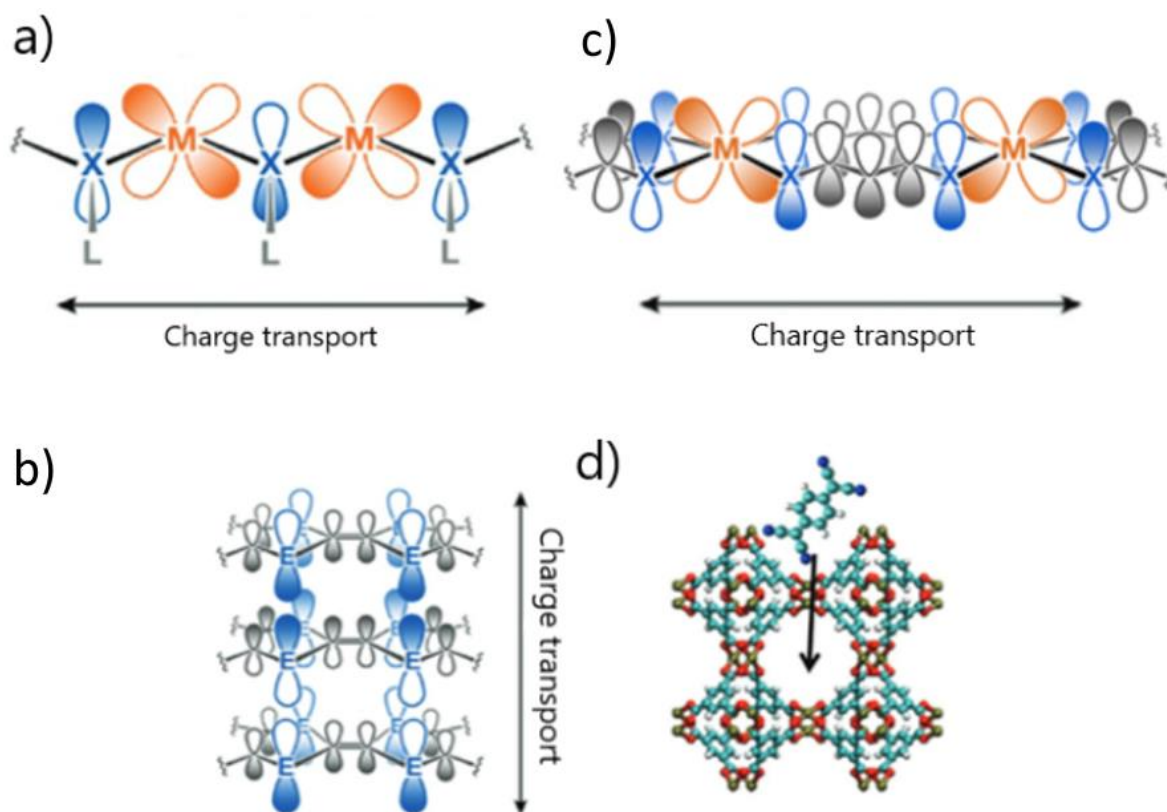

Figure 16. Orbital representations of different band-like charge transport pathways in MOFs. a) Through-bond pathway, b) Through-space pathway, c) Extended conjugation pathway and d) Quest involving charge transport with $Cu_3(BTC)_2$-MOF and TCNQ quest. Edited from the articles.[31,66]

When using ligands, which contain organic core conjugated chelating functional groups, they can be paired with transition metals to create frameworks with an extended conjugation (Figure 16. c). The ligands found in this kind of MOFs can include for example dihydroxybenzoquinone, chloranilic acid, and hexa-substituted benzenes. In addition, a few usable functional groups are diamines, dithiols, and orto-diols. Some MOFs have an extended π-d conjugation within the *ab* plane (*a* plane normal to the *c*-axis, to which the mesoporous channels align)[67], which is very similar in nature to the *sp*^{2}-hybridization of graphene. Therefore, some 2D-MOF structures are referred to be metal-organic graphene analogues. MOFs with π-d conjugation usually have the highest conductivity among MOFs, because it allows an efficient charge carrier delocalization within the plane. [66]

In through space pathway, the conductivity is strongly affected by the stacking distance between the π-π interactions showing ligands. The conductivity increases with decreased spacing, and it can also be modified by involving different sized metal ions or by varying the stacking motifs in ligands. Although the π-π interactions are highly directional, the anisotropy of through space conductivity will also take place in C-MOFs. This can be avoided, for example, by growing the MOF in an aligned way on other materials. If electroactive guests are involved in the framework, the charge transport pathway can travel through them. In this case, the conduction occurs from guest to guest or guest to ligand. One example of quest involving charge transport is Cu$_3$(BTC)$_2$-MOF (BTC = benzene-1,2,4-tricarboxylic acid) and TCNQ (tetracyanoquinodimethane) quest. The quest placement into the pore of the MOF structure is visualised in Figure 16 d. However, when electroactive guests are involved into a framework, the porosity may decrease significantly. This can restrict the use of guests for the purpose of increasing conductivity.[66]

In addition to band-like transport pathways described above, when the structure does not have that kind of transport allowing crystallographic pathways, the charge transport is assumed to occur via redox hopping. This requires redox-active material and a small spatial separation between the active components. Redox-hopping is likely to be the general mechanism of the conduction in MOFs, because they often include redox-active materials, but which are too far from each other for their orbitals to overlap. The conductivity in structures implementing this mechanism is usually lower compared to conductivity with the other mechanisms. However, the limiting factors of the conductivity are proposed to vary considerably. The affecting features can be, for example, charge carrier concentration and mobility or grain boundary resistance.

Ligands with metal-dithiolene units or azo groups and conjugated organic cores can be used as redox-active components offering higher conductivity.[66]

Redox hopping can occur via either metal units, organic linkers (Figure 17) or both. Already in 2009, Takaishi *et al.*[68] hypothesized, that combining $[Cu^{3+}(PDT)]^-$ (PDT = pyrazine-2,3-dithiolate) – a commonly known electron acceptor – with electron donating Cu^+ ions, it would lead to an electrically conductive $Cu[Cu(PDT)_2]$ 3D-MOF. When analysing the bond lengths and angles of this structure with X-ray crystallography, the crystal structure indicated an electron transfer between the fragments bringing both copper sites to an oxidation state of Cu(II). The oxidation state determination was supported by the paramagnetic behaviour of the sample. Thus, the research group attributed the relatively high conductivity to a metal-based redox hopping between the copper units.[66]
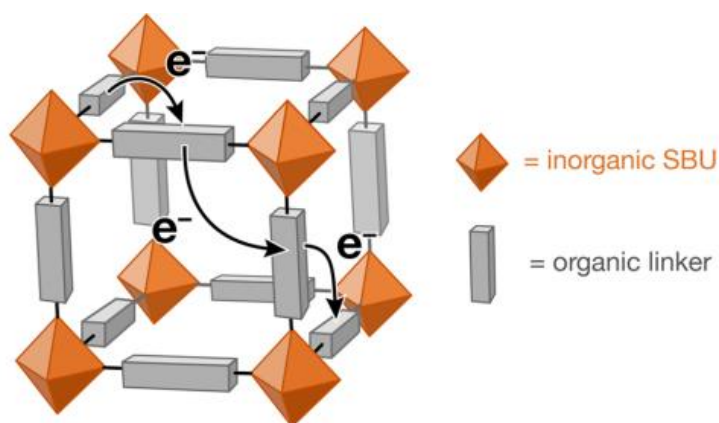

Figure 17. Redox hopping between organic linkers.[66]

In 2019, Hupp *et al.*[69] reported a study of anisotropic NU-1000-MOF, wherein the charge transport occurs via linker-based redox hopping focusing on the commonly-used carboxy-terminated tetraphenylpyrene $TPPy(COO^-)_4$ and its radical $TPPy^{+/0}$. The topology of this ligand causes the strength of linker-linker electronic coupling to be strongly dependent on the coupling direction and whether the hopping occurs along the *c*-axis or *ab* plane (Figure 18), making the redox hopping also anisotropic. According to the computational results that are based on the Marcus' theory of electron transfer, the $D_{hopping}$ is up to 3500 times larger in the *c*-direction than through the *ab* plane. Based on this information, Hupp's group prepared the NU-1000-MOF on a ZnO-coated fluorine-doped tin oxide (FTO) electrode via an electrophoretic route to achieve vertical crystals, and by solvothermally for crystals to grow normal to the FTO. The experimentally measured $D_{hopping\ (c)}$ to $D_{hopping\ (ab)}$-ratio was approximately 3500 supporting the computational expectation.
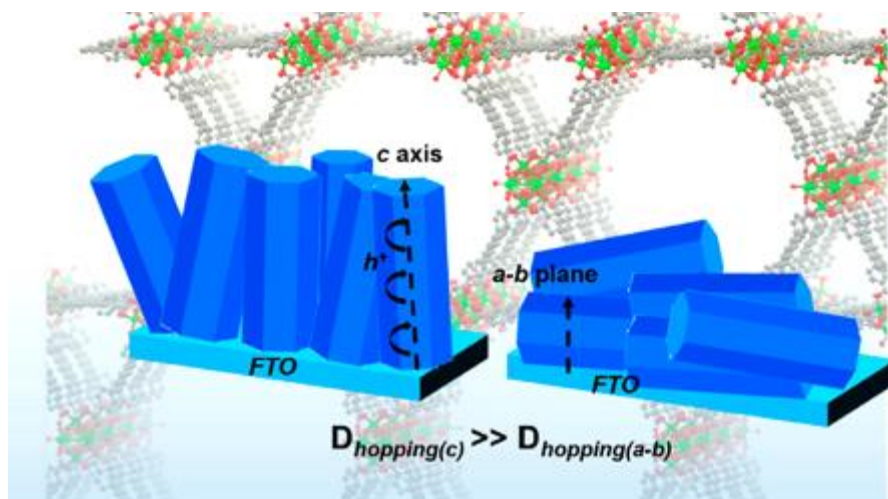
Figure 18. A visualisation of redox hopping along the *c*-axis and through the *ab*-plane.[69]

For more efficient charge separation, MOFs can be integrated with other semiconductors forming MOF composite materials. In PEC water splitting, heterojunctions in these materials can help boosting the separation further. TiO_2 has very a wide band gap of 3.2 eV and a high e^-/h^+-recombination rate, and thus can benefit from MOF integration.[26,70] MIL-125-NH_2 is a commonly used photocatalyst, which consists of TiO_2-clusters and 2-aminoterephthalic acid ligands (NH_2-BDC). Light irradiation generates electrons (photogenerated electrons) in the organic ligands, which migrate to Ti-oxo clusters. 2019 Yoon *et al.*[70] used MIL-125-NH_2 as a precursor for photocatalytic TiO_2 electrode by coating TiO_2-nanorods with the MOF via a hydrothermal reaction to accomplish efficient PEC, which showed better photocurrent density of 1.63 mA/cm^2 at 1.23 V *vs*. RHE. This corresponds to an IPCE of 84.4 % at the maximum absorption wavelength (λ_{max} = 340 nm). The MIL-125-NH_2-coating improves the charge separation and the electron transfer from the CB of MOF to the CB of TiO_2, if an optimal semiconductor band is established at the interface of the structures. Even if TiO_2, the mother of photoelectrochemical cell materials, is considered as one of the most efficient and commonly used semiconductors for PEC, it often requires chemical or electrical bias to work properly.[16] In addition, metals can be included into the MOF-based composite to increase the charge separation efficiency. Yang *et al.*[71] (2018) coated TiO_2 nanorods with a porphyrin-based MOF (PCN-225) and then introduced Co(III) ion into the MOF layer. As a result, compared to the non-Co-doped material, the photocurrent density increased from 1.99 mA cm^{-2} to 2.93 mA cm^{-2} at 1.23 V *vs*. RHE.

7   Summary

Because of the continuously warming climate and its concerning effects to the economy and environment, in addition to the depletion of the non-renewable fossil fuels, developing new sustainable energy production systems and innovations is extremely urgent. As hydrogen is predicted to play a key role in reducing carbon emissions, the focus must be in the environmentally friendly, green production methods. The integration of MOFs with PEC is a promising future solution for green hydrogen production, because the wide range of combinations of ligands and metals can help achieving wider light absorption range and directing charge transfers, in addition to the high porosity offering more active sites and reaction surface. MOFs can be synthetised in a variety of ways, even in environmentally friendly conditions, and they can also be modified and functionalised post-synthetically. In addition to the low emission production, also the storage and transportation of hydrogen need more advanced solutions, to which MOFs could provide the answer.

The use of only sunlight as an energy source for hydrogen production would be ideal, but it is highly ambitious, because there have not been found a MOF compound capable to catalyse the complete water splitting reaction. Therefore, the route to synthetise MOFs for photocatalytic hydrogen production still appears to be needing intermediate stages, where different green energy forms can be combined. In a short term, it is more promising and realistic to try to focus on discovering and synthetising metal-organic framework -based techniques for photoelectrochemical rather than photocatalytic hydrogen production.

Still, even if the green hydrogen production with MOFs requires a lot of research, the use of MOF-compounds as electrode material is clearly justified and it seems to be just a matter of time, when the right parameters for successful compound with for example a suitable band gap energy can be found. Because of the lack of the detailed definition of semiconductor properties of MOF-structures and the poor understanding of the band levels and optical absorption, the number of experimental studies on the field need to be increased along with the theory of optical semiconductors and MOFs. This is important reaching to the change from the current energy economy to a green hydrogen-based faster. Luckily, the constantly growing fundings for the research push us closer to this goal.

EXPERIMENTAL

8   The goals of the research

The aim of this work was to synthetise known MOF-compounds suitable for water splitting and the structures were chosen for a several different reasons. Some of the syntheses were interesting for their fast and mild reaction conditions or hydrogen production improving modifications, but also a simplification of a synthesis route of a well-known compound was attempted considering the possibility of produce the MOF on an industrial scale. In addition, some compounds were attempted to grow on electrode materials for a potential further use. The reactions were carried out as saturation crystallization, solvothermal and hydrothermal reactions and by refluxing. The solvothermal and hydrothermal reactions were performed in Teflon-lined autoclave reactors (Figure 19) and the electrode samples were dried in a Schlenk line under a nitrogen atmosphere.

Figure 19. An autoclave reactor with the Teflon chamber.

9   Materials and methods

The structures were synthetised according to the literature [43,72,73,74,75,76,77] and the used reagents were commercially available compounds. Most of the structures were based on a widely used terephthalic acid ligand, which has been much functionalised and reported in the literature. Thus

making it a relatively firm starting point for studying utilisation of MOFs for different application fields. The reagents, their manufacturers, purities, and molar masses are listed in Table 2 excluding the used solvents.

Table 2. The reagents used in the experimental work.

Compound (CAS)	Manufacturer	Purity	Molar mass
Copper(I) iodide (7681-65-4)	Fluka	> 98 %	190.44 g/mol
4,4´-Bipyridyl (553-26-4)	TCI	> 98 %	156.19 g/mol
2-aminoterephtalic acid (10312-55-7)	Sigma Aldrich	99 %	181.15 g/mol
Zirconium(IV) chloride (10026-11-6)	Strem Chemicals	99.5 %	233.03 g/mol
Terephthalic acid (100-21-0)	Sigma Aldrich	98 %	166.03 g/mol
2-bromoterephthalic acid (586-35-6)	Sigma Aldrich	97 %	245.03 g/mol
Benzene-1,2,4-tricarboxylic acid (528-44-9)	Fluorochem	97 %	210.14 g/mol
2-nitroterephthalic acid (610-29-7)	Fluorochem	95 %	211.13 g/mol
$TiCl_4$ (7550-45-0)	Riedel de Haën	99 %	189.71 g/mol
Tetrabutyl orthotitanate monomer (5593-70-4)	Fluka	> 97 %	340.36 g/mol
2-Methylimidazole (693-98-1)	BASF	p.a.	82.10 g/mol
Zinc nitrate hexahydrate (10196-18-6)	J. T. Baker	99.5 %	297.49 g/mol
Hexamethylenetetramine (100-97-0)	VWR	> 99 %	140.19 g/mol
Zinc acetate dihydrate (5970-45-6)	Merck	99.5 %	219.49 g/mol
Nickel(II) acetate tetrahydrate (6018-89-9)	Fluorochem	98 %	248.84 g/mol
Potassium hydroxide (1310-58-3)	VWR Chemicals	> 85 %	56.12 g/mol
Sodium borohydride (16940-66-2)	Fisher	> 98 %	37.83 g/mol
Gold(III) chloride trihydrate (16961-25-4)	Sigma Aldrich	≥ 99.9 %	393.83 g/mol
$(NH_4)_2Ce(NO_3)_6$ (16774-21-3)	Merck	≥ 99 %	548.22 g/mol

Powder x-ray diffraction was the main characterisation method for all the synthetised products and the measurements were performed with PANalytical X'Pert Pro powder X-ray diffractometer using Cu K_α -radiation ($\lambda = 1.54184$ Å) produced with an X-ray tube with 45 kV voltage and 40 mA current. The powdery samples were prepared on a zero-background silicon disc with a diameter of approximately 10 mm, and for FTO and nickel foam substrates modified cavities with elevated aluminium plates were used for a precise fit. The measured diffraction patterns were compared to the reference patterns retrieved from ICDD PDF-4+[78] powder

diffraction database and Cambridge Structural Database[35]. For thermogravimetric analysis, Perkin Elmer STA 6000 simultaneous thermogravimeter-differential scanning calorimeter (TG/DSC) analyser was used. For a deeper understanding of the topography, composition, elemental distribution, and particle organization and size, SEM images were taken from the coated FTO and NF samples. The images were acquired using Zeiss EVO 50 Scanning Electron Microscope with Bruker Quantax 400 Energy Dispersive Spectrometer. For the SEM images, the electron high tension was adjusted between 15 kV and 20 kV, and the EDX analyses were performed on a range of 0–20 keV. In thermogravimetric analyses, 5-8 mg of each powdery sample were weighed into Al_2O_3 crucible. The measurements were performed under air atmosphere with a flow rate of 40 ml/min. Before each measurement, the sample was held at 22 °C for a one minute, followed by heating up to 600 °C with a constant 15 °C/min heating rate.

9.1   CuI-(bpy)

CuI-(bpy)-MOF, constructed from Cu_2I_2 and 4,4′-bipyridine (bpy) is a cost-effective structure exhibiting photocatalytic activity for H_2 production without any auxiliary substances. The Cu_2I_2 clusters accelerate the copper(I) hydride interaction generating photoelectrons and thus providing redox reaction sites for HER. Proven to be highly stable structure with mild reaction conditions, having a narrow bandgap (2.05 eV) and efficient hydrogen production rate (7.09 $mmol\,g^{-1}\,h^{-1}$), the CuI-bpy MOF has broadened the understanding of the future design of durable MOFs for solar fuel production.[79]

In this experiment, CuI-bpy-MOF was synthetised according to the Batten *et al.* article (1999)[72] by dissolving 0.1894 g (1.0 mmol) CuI to 10 ml of ACN (acetonitrile) and 0.3129 g (2.0 mmol) 4,4'-bpy to 20 ml ACN in separate 25 ml beakers on a heat plate forming 0.1 M solutions. After the reactants had dissolved, they were combined, and the mixture was heated for 10 minutes on a heat plate. Already in one minute the solution started to turn red. After cooling down to room temperature, the red precipitate was filtered with suction and washed with 30 ml of ACN. The dry product (EBP-013-b) was put in the desiccator overnight, after which the mass was weighed to be 0.3319 g. After drying, a PXRD pattern was measured from the product (Figure 20). The measurement gave sharp peaks with good intensities, and even if most of the peaks had shifted towards lower 2θ angles, the PXRD measurement confirmed the product to be the desired compound found from the PDF-4+ database with a reference code 01-087-6931 (Kobayashi *et*

al. 2019)[80]. The shift can be caused by many things, such as differences in lattice parameters or crystal size between the measured sample and the database measurement. In addition, temperature is an important factor to take into account when comparing measured data to the database.
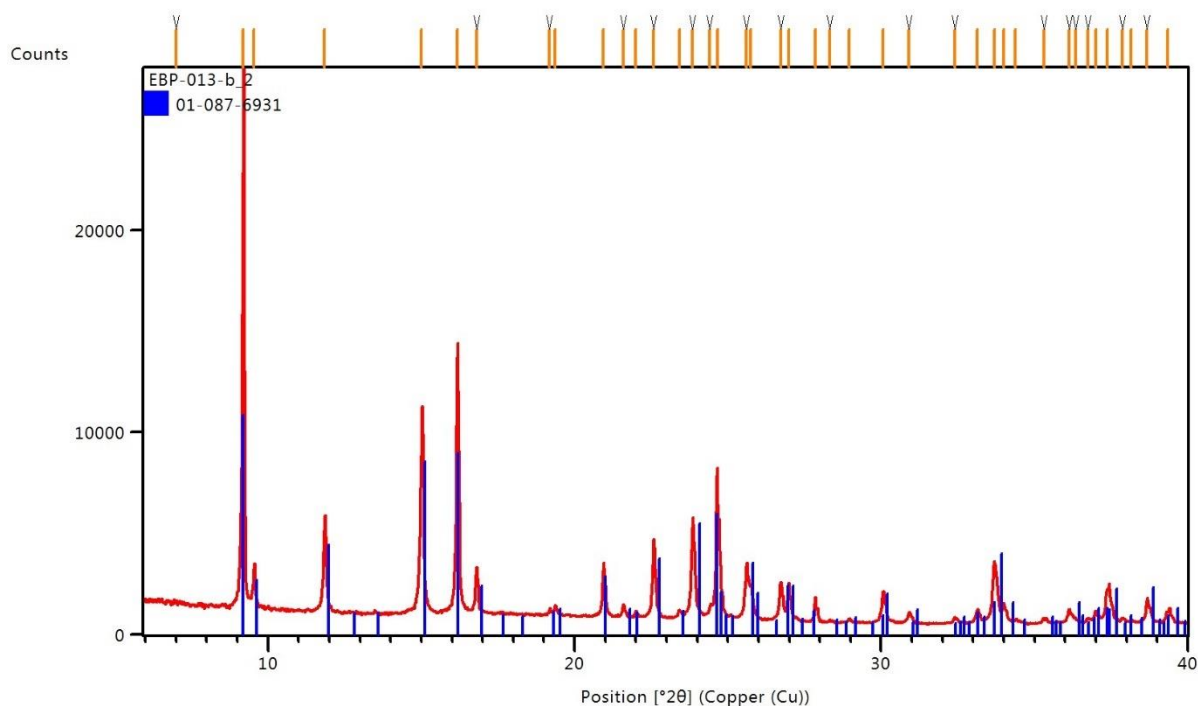
Figure 20. The powder diffraction pattern of EBP-013-b and the peaks of a corresponding reference from the database.[80]

In the TG/DSC analysis of EBP-013-b (Appendix 3, Figure 21. a, Table 3.), the first of the two mass loss phases occurred in 209 °C (wt.-% 22.44) in an endothermic reaction. This first smaller decomposition event was followed by the actual decomposition of the product (wt.-% 54.60) in 328 °C, which was according to the DSC curve, an exothermic burning reaction leaving a residual mass of 23.33 wt.-%. The measurement left an orange-brown deposition to the top lid of the TG- furnace, but the composition of this product could not be identified without further elemental analysis.

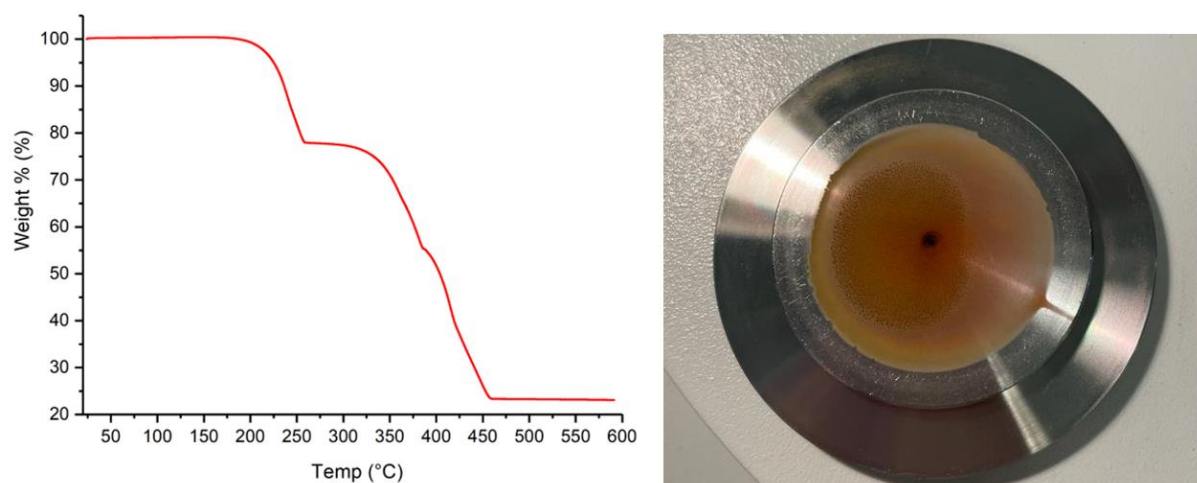Figure 21. a) The TG curve of EBP-013-b and b) The deposition of the decomposition products of EBP-013-b on the top lid of the TG- furnace.

Table 3. The results for the thermogravimetric measurement of EBP-013-b.

Compound	Mass losses wt.-%, (T-range) (%), (°C)	Residual mass wt.-%, (T) (%), (°C)	T_d (°C)
EBP-013-b	22.44, (167–261)		209
	54.60, (261–466)	23.33 (466)	328

T_d = The extrapolated onset temperature of the thermal decomposition.

9.2   NH₂-UiO-66

The synthesis of NH$_2$-UiO-66 was performed adapting Kandiah's[73] and Motegi's[74] groups' articles together. 1.5168 g ZrCl$_4$ (6.5 mmol) and 1.5622 g NH$_2$-BDC (8.6 mmol) were dissolved in 100 ml of DMF in a 250 ml round bottom flask, where the mixture was refluxed for 2 h at 145 °C. After 1.5 h, a yellow precipitate was appeared to the mixture and after another 0.5 h and cooling down to room temperature, the precipitate was filtered with suction, and washed with 20 ml DMF and 40 ml ethanol. The yellow product (EBP-067) was left on a watch glass in a desiccator for two days, and the weight of the dried product was 0.2221 g. A PXRD-

measurement (Figure 22) was performed for the product between angles 4-40° 2θ, but it turned out to be completely amorphous with a strong diffraction hump before 10°, where two of the characteristic strong peaks of a NH_2-UiO-66 should, however be located.
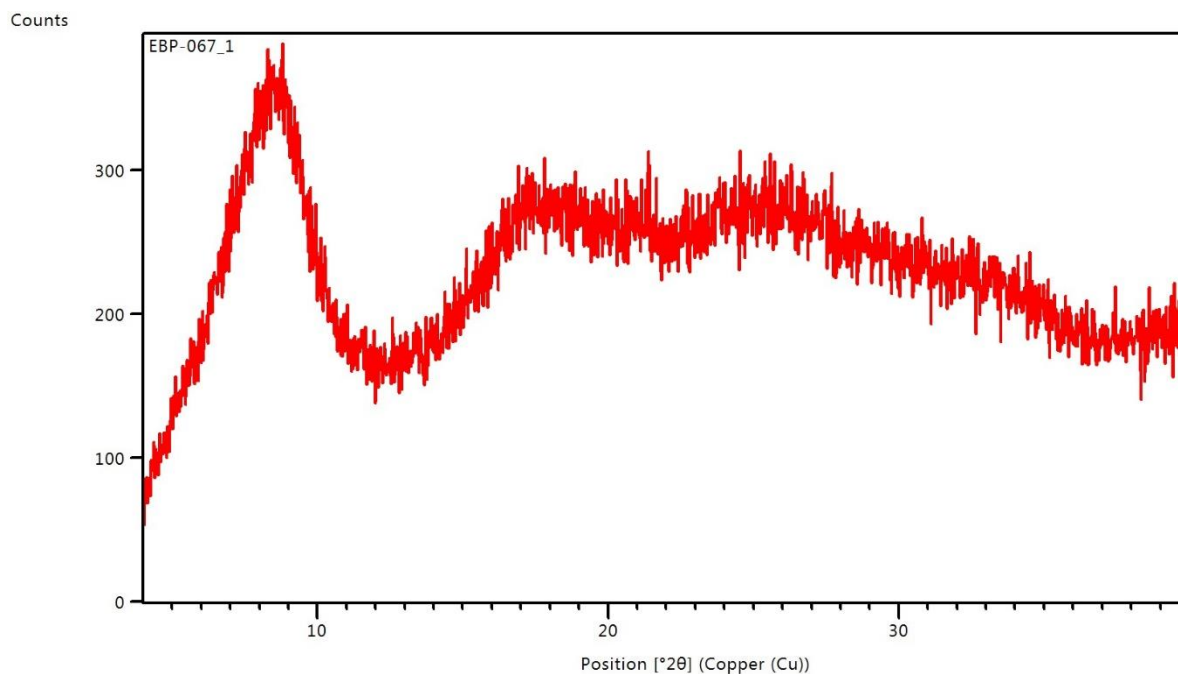
Figure 22. The PXRD pattern of EBP-067.

In the thermogravimetric analysis (Appendix 4, Figure 23, Table 4), the mass losses of EBP-067 occurred in two phases. The first, immediate mass loss (wt.-% 9.02) could have been due to the absorption of the washing ethanol or humidity in the pores of the structure. The actual decomposition of the compound occurred approximately in 306 °C in a rapid, exothermic burning reaction leaving a residual mass of 33.82 wt.-%. Even though the successfully synthetised NH_2-UiO-66 has reported to be stable up to 400 °C[81], the relatively high heating rate could have contributed to the solvent molecules evaporating at a higher temperature which, in turn, could have made it somewhat more difficult to determine the extrapolated thermal decomposition temperature accurately.
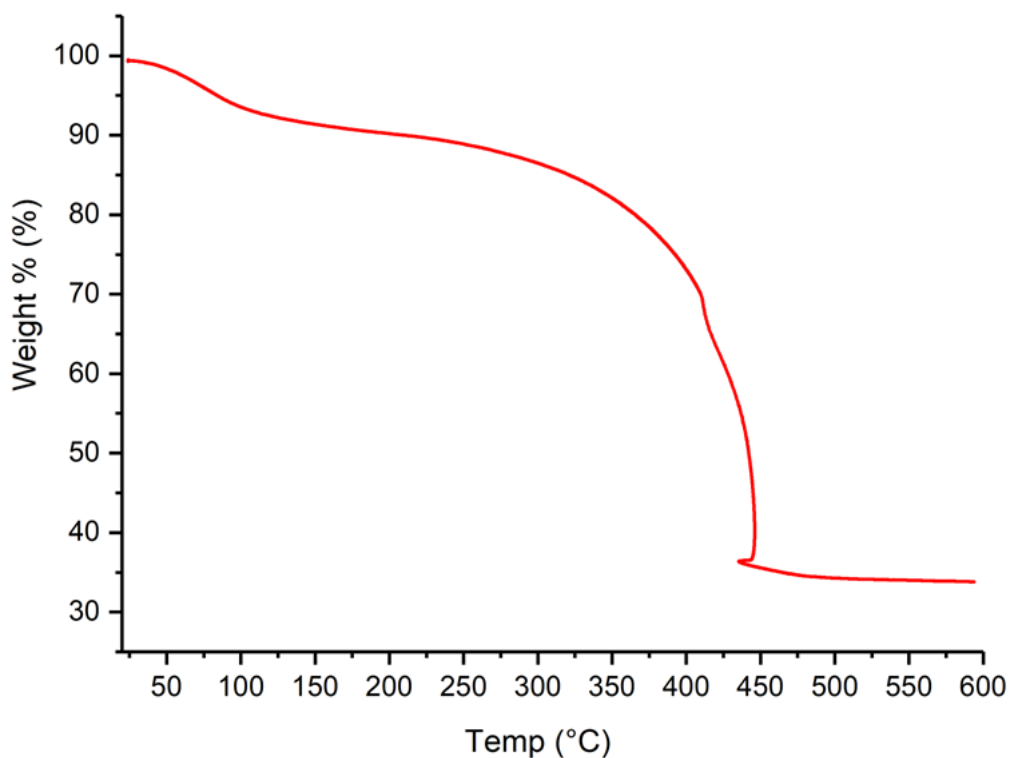
Figure 23. The TG curve of EBP-067.

Table 4. The results for the thermogravimetric measurement of EBP-067.

Compound	Mass losses	Residual mass	T_d
	wt.-%, (T-range)	wt.-%, (T)	(°C)
	(%), (°C)	(%), (°C)	
EBP-067	9.02, (24–187)		46*
	5,92, (240–494)	0.53 (494)	306

T_d = The extrapolated onset temperature of the thermal decomposition.

* = The extrapolated onset temperature for desolvation/dehydration.

9.3 Ni(OH)₂-ZIF-8-ZnO-Nickel Foam

Growing ZnO nanorods on an electrode is beneficial in PEC water splitting due to many aspects, such as high surface-volume ratio, short lateral charge transport length and low light reflection.

ZnO is also a cheap, non-toxic material. However, the surface passivation is required to reduce electron-hole recombination due to oxygen vacancies. The first MOF-based transparent surface layer for PEC, using ZIF-8 was prepared on a nickel foam (NF) supported ZnO nanorod arrays photoanode with Ni(OH)$_2$ nanosheets as synergic co-catalysts according to Liu *et al.* article (2018).[75] The grafted structures on the nickel foam are demonstrated in the Figure 24:
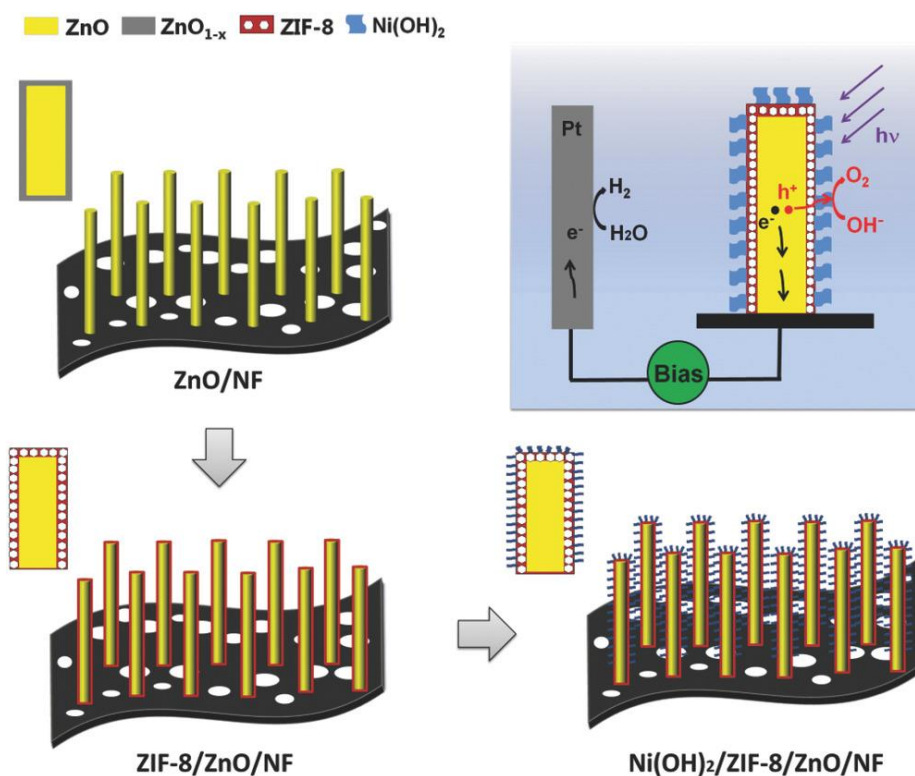
Figure 24. The preparation steps of Ni(OH)$_2$-ZIF-8-ZnO layer on a Nickel foam photoanode and a PEC water splitting mechanism.[75]

A 10.0 x 45.0 x 1.6 mm^2 piece was cut from the nickel foam and it was held in 1 M HCl for 30 min to remove the possible oxide layer from the surface. After the HCl bath, the piece was ultrasonicated with water and then with ethanol, both for 5 minutes, at the same time as 1.576 g of ZnOAc was almost completely dissolved into 100 ml ethanol forming a 0.06 M solution under 15 min ultrasonication. The NF was immersed in the solution for 30 seconds and dried in the oven at 80 °C for two minutes. The immersion-drying step was repeated three times, finally followed by a 30 min heating at 350 °C in an oven. While a ZnO seed layer was growing under the heating, a 50 ml water solution containing 0.4202 g of HMT (hexamethylenetetramine) (0.06 M) and 1.4045 g Zn(NO$_3$)$_2$ (0.06 M) was prepared. The seeded NF was then put into a 50 ml Teflon autoclave and covered with the HMT-Zn(NO$_3$)$_2$ solution. The autoclave was heated in an oven at 90 °C for 12 h. After the treatment, a thin, white layer

had appeared on the surface of the NF (Figure 25). After cooling, the foam was washed with deionized water and put in the oven to dry at 60 °C for 24 h. The washing was too harsh for the ZnO layer, and parts of it were washed off.

To form the ZIF-8 layer, the dry sample was put in 100 ml Teflon-lined autoclave with 64 ml of DMF/H_2O solution (3:1 v/v) including 0,04 g (0.49 mmol) of 2-methylimidazole, and the reactor was kept in an oven for 1 h in 70 °C. After cooling, the ZIF-8-ZnO-NF sample was washed with ethanol immersing the sample into the solvent three times. The washed and dried sample was then immersed in 3 mM of aqueous NiOAc solution for 20 min and then in 0.1 M KOH solution for 10 min. The resulted Ni(OH)$_2$-ZIF-8-ZnO-NF sample (EBP-068, shown in Figure 25 a) was washed with deionised water and left to dry under argon atmosphere in a Schlenk line overnight.

Figure 25. The ZIF-8-ZnO-Nickel Foam samples a) EBP-068, b) EBP-068-b and ZnO-Nickel foam sample c) EBP-081.

The exact procedure was repeated for a 10.0x5.0x1.6 mm^2-sized NF piece (EBP-068-b, shown in Figure 25 b) for a better fit in the electrolyser with 1.5754 g of ZnOAc, 0.4198 g of HMT, 1.4035 g of Zn(NO$_3$)$_2$ each forming the 0.06 M solutions and 0.04 g (0.49 mmol) of 2-methylimidazole respectively. In addition, to distinguish the ZIF-8 layer from the ZnO layer, a NF sample with only the ZnO layer (EBP-081, shown in Figure 25 c) was synthetised with the same procedure as before with 1.5757 g ZnOAc, 1.401 g Zn(NO$_3$)$_2$ and 0.4208 g HMT. The sample was left into the 350 °C oven for 30 min overtime (1 h total), and the NF turned slightly brown.

The Ni(OH)$_2$-ZIF-8-ZnO-NF samples were measured with PXRD in a measurement range of of 6–80° 2θ with a step time of 200 sec (Figure 26). All the measurements gave peaks with identical angles, only with different intensities. The two groups of three peaks between 30–38° 2θ and 66–70° 2θ and the peaks at 47.7°, 56.8°, 62.9° and 72.8° 2θ, in addition to the peak couple between 76–78° 2θ correspond to the PXRD pattern of ZnO (refcode 04-004-4530). The

two other peaks at 44.5° and 52.0° 2θ correspond pure nickel (refcode 04-014-0268) originating from the substrate foam. The correspondences are presented in Figure 27. Since the step time was relatively high and still more peaks did not appear, it can be assumed, that the possible ZIF-8-MOF would not be able to be distinguished with PXRD measurements in this case. In addition, the lack of ZIF-8 and $Ni(OH)_2$ diffraction peaks were expected, based on the results shown in the article of Liu *et al.* The PXRD measurement of EBP-081 with only the ZnO layer (Figure 26) gave, again, peaks with identical angles analogously with the previous samples. The intensities differ from the 068-samples, because of the shorter step time of 50 sec.
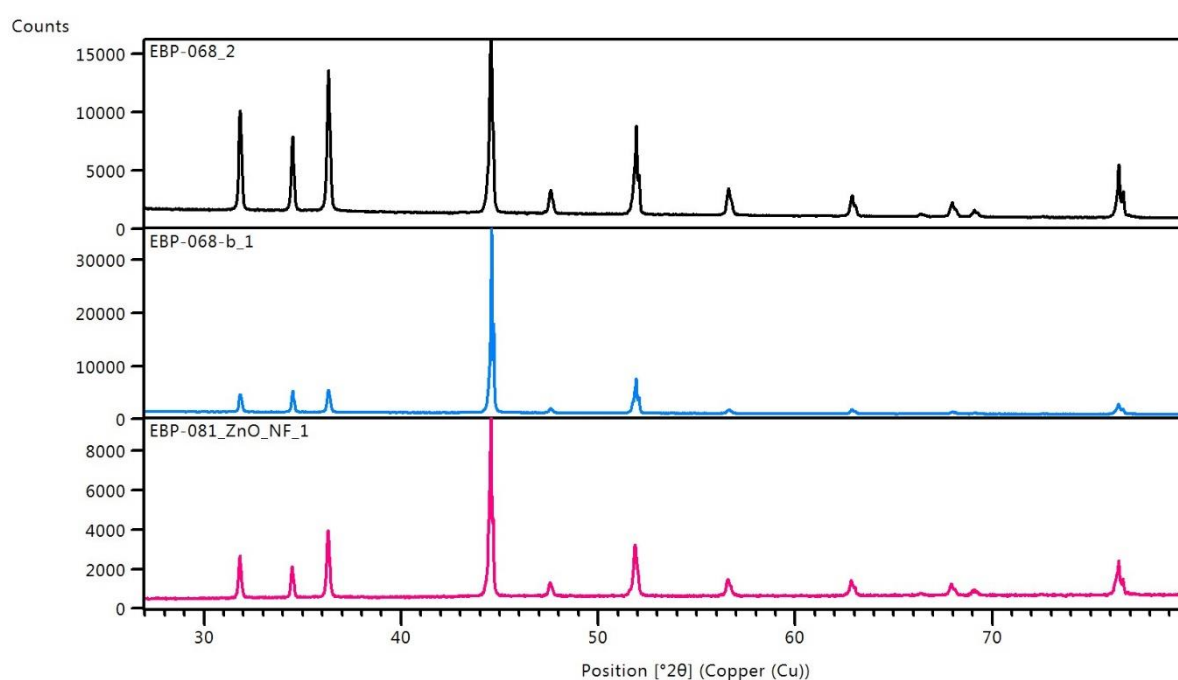
Figure 26. Comparison of the PXRD patterns of EBP-068, EBP-068-b and EBP-081.
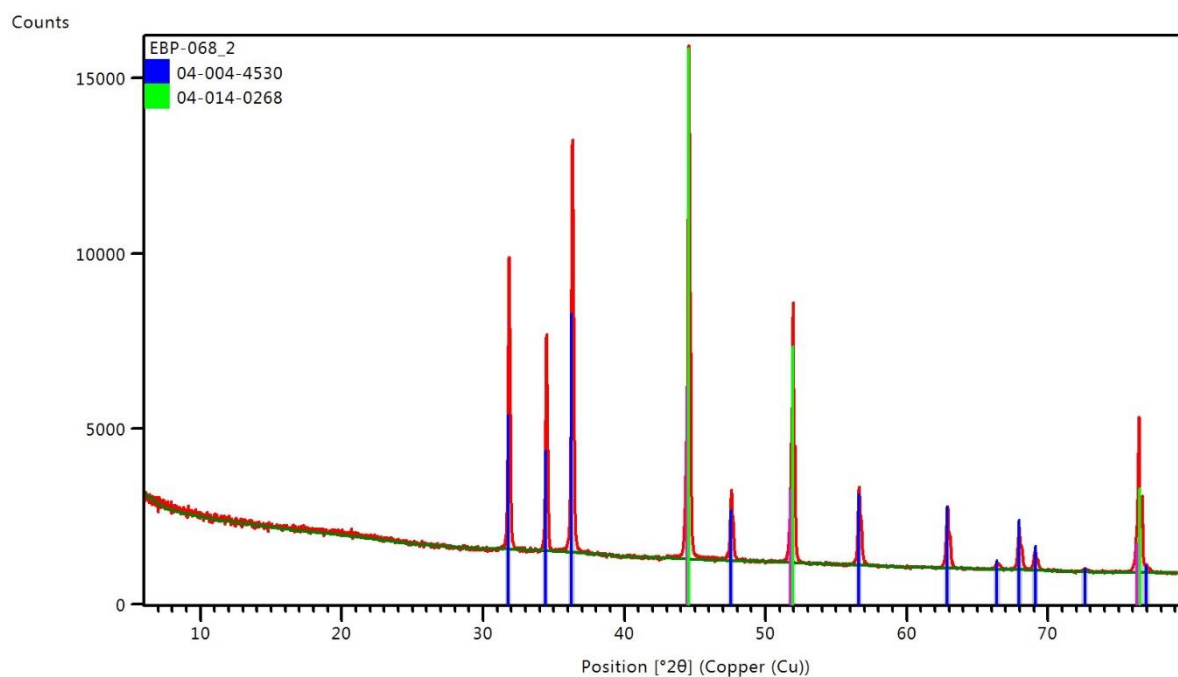
Figure 27. The PXRD pattern of EBP-068 with the correspondences: ZnO (blue) and Ni (green).

Compared to the SEM images of Ni(OH)$_2$-ZnO-ZIF-8-NFs in the Liu *et al.* article (Figure 28), the images in this work (Figures 29 and 30) were expected to show tight layer of thin ZnO/ZIF-8 nanorod layer, and not the Ni(OH)$_2$ on top. In Figure 29 it can be seen extensive areas of rods with different sizes and geometries. According to Liu *et al.*, the main visual difference between the ZnO-nanorods and ZIF-8-ZnO-nanorods is, that the ZnO appears to be softer and rounder at the tip, when the ZIF-8-ZnO follows a pricklier shape. In Figure 29 b) rods can be seen, which seem to be matching to the ZIF-8-ZnO morphology and even the reported size of 500 nm and less. Even if the sizes of the nanorods are for the most parts the same as in the article, there are also larger pieces strongly nucleated in some areas of the nanorod field.
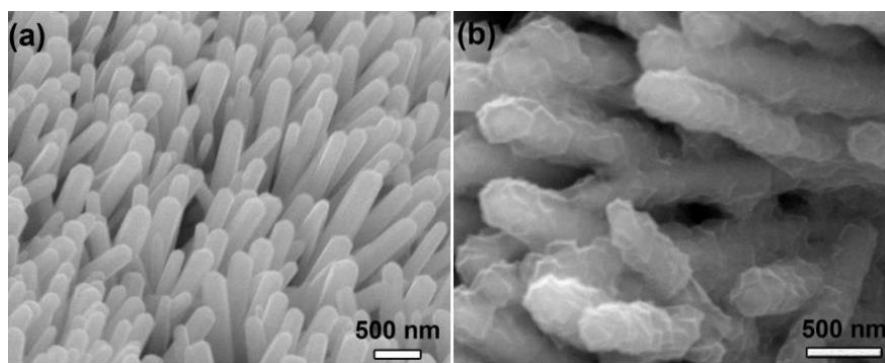
Figure 28. The previously reported SEM images of a) ZnO/NF nanorod arrays and b) ZIF-8/ZnO/NF (Liu *et al* 2018).[75]
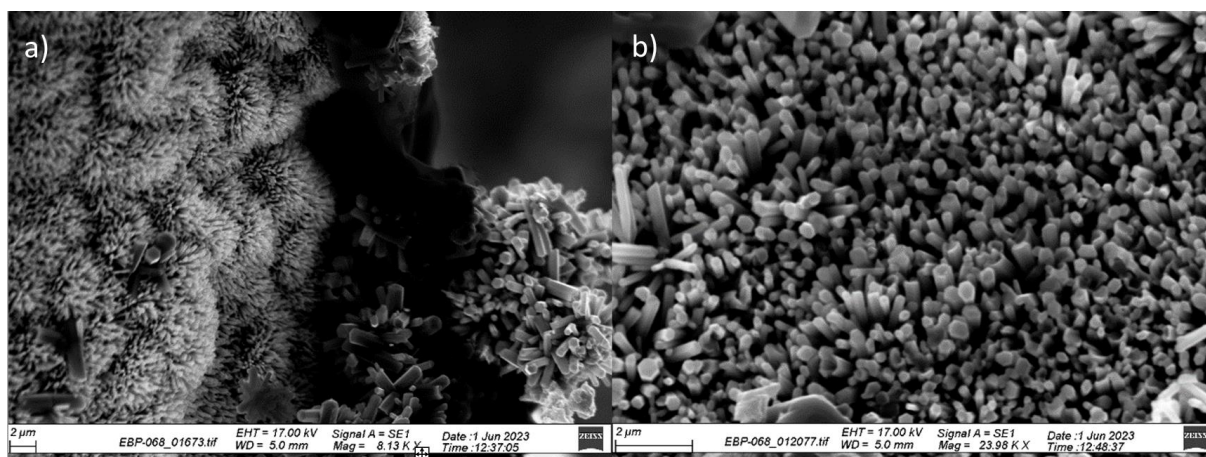
Figure 29. The SEM images of EBP-068 sample surface (a–b).

The EDX measurements of the sample EBP-068 (Appendix 6, Figure 30, Table 5) supported only the observation of ZnO rods: When the measurement was performed in an area on a larger particle, signals of Zn (<70 wt.-%, <50 at.-%) and O (6.65 wt.-%, 20.08 at.-%) were distinguished in addition to some secondary peaks. High concentration of rhenium was also detected but based on the characteristic signal of rhenium (Lα 8.651 keV) and zinc (Kα 8.630 keV), the Re signal in this measurement corresponds to the signal of Zn. Similarly, the obtained Na signal (Kα 1.041 keV) corresponds to the Zn signal (Lα 1.012 keV). Therefore, the Re and Na signals have been left out of the EDX Tables 5, 6 and 7. Based on the results of the EDX analysis is impossible to tell, if the ZIF-8-MOF had grown on the ZnO-nanorods, because of the same metal of the substrate and MOF, in addition to the absence of signals for some other elements in the ZIF-8 structure.
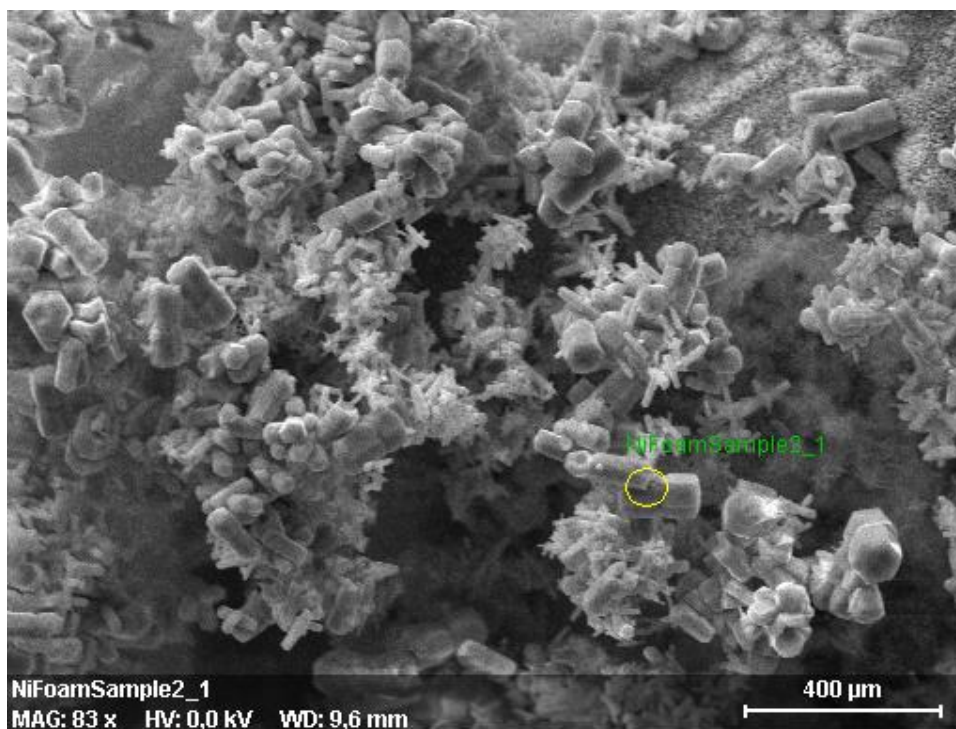
Figure 30. The SEM image of EBP-068 sample surface with the area for the EDX measurement marked with an oval.

Table 5. The main signals of the SEM-EDX measurement of EBP-068.

Element	Atomic number	Series	norm. C [wt.-%]	Atom. C [at.-%]	Error [%]
Zn	30	K-series	67.99	50.26	3.0
Ni	28	K-series	3.14	2.59	0.6
O	8	K-series	6.65	20.08	1.8
Total:			100 %	100 %	

norm. C [wt.-%] = normalised concentration in weight percent of the element.

Atom. C [at.-%] = atomic concentration in weight percent of the element.

In the SEM images of EBP-081 (Figures 31 and 32), particles with similar morphologies can be seen with different arrangements compared to the images of EBP-068. In addition, the size of the larger particles of EBP-081 corresponds to the similarly sized particles seen on the images of EBP-068, but in the Figures 31 and 32 smaller, miscellaneous particles can be seen next to the larger ones. A similar, distinct ZnO nanorod field on the surface of EBP-068 sample cannot be seen in the case of the EBP-081 sample, but there appears to be a smoother surface instead. According to the EDX measurements (Appendix 7, Figure 32), the smooth area (Table 7)

contained mainly zinc (>50 wt.-%, 44.82 at.-%) and nickel (33.43 wt.-%, 33.19 at.-%), and a trace amounts of oxygen. The smooth area is therefore not a ZnO nanorod field, but possibly a pure layer of zinc. Again, in the EDX-measurement of the separate larger particles (Table 7) the signals of zinc (>60 wt.-%, >51.49 at.-%) and nickel (21.90 wt.-%, 21.32 at.-%) were obtained. However, these particles contained a bit more oxygen (1.10 wt.-%, 3.94 at.-%), which could be a contributing factor of why the particles have been nucleating separate from the smooth area. The reason, why there is no oxygen on the areas where the ZnO nanorod field was expected to locate, can be due to the possible burning of the sample in the ZnO seeding phase. This could also affect the fact that the particles on the EBP-081 are not in organised arrays, but more in particles with random shapes, sizes, and order.
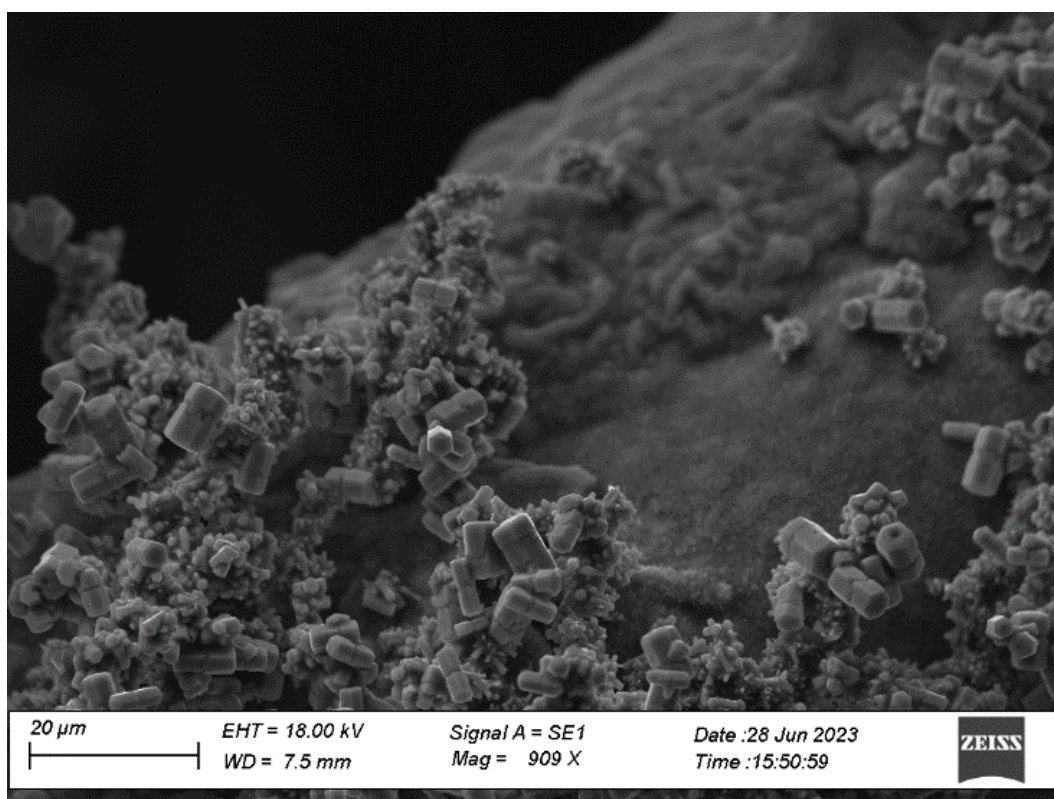
Figure 31. The SEM image of EBP-081 sample surface.
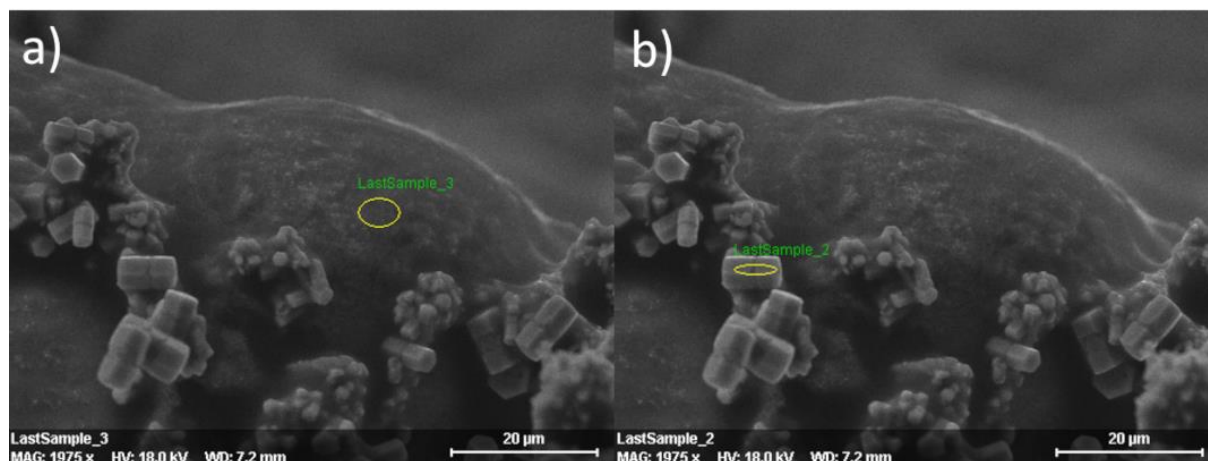
Figure 32. The SEM images of EBP-081 sample surface. a) The marked area for EDX on the smooth surface and b) the area for EDX on a larger particle.

Table 6. The main EDX signals of the smoother area of EBP-081 surface.

Element	Atomic number	Series	norm. C [wt.-%]	Atom. C [at.-%]	Error [%]
Zn	30	K-series	50.29	44.82	4.9
Ni	28	K-series	33.43	33.19	2.4
Total:			100 %	100 %	

norm. C [wt.-%] = normalised concentration in weight percent of the element

Atom. C [at.-%] = atomic concentration in weight percent of the element.

Table 7. The main EDX signals of the particles on EBP-081 surface.

Element	Atomic number	Series	norm. C [wt.-%]	Atom. C [at.-%]	Error [%]
Zn	30	K-series	58.95	51.49	6.4
Ni	28	K-series	21.90	21.32	3.0
O	8	L-series	1.10	3.94	1.0
Total:			100 %	100 %	

norm. C [wt.-%] = normalised concentration in weight percent of the element

Atom. C [at.-%] = atomic concentration in weight percent of the element.

9.4   Room temperature synthesis of Ce-UiO-66-X-MOFs

Many MOF syntheses require elevated temperatures but Ce-UiO-66-MOF catalysts for PEC are inaccessible in high temperatures. Fortunately, these robust and reusable structures can be achieved in room temperature. Mild synthesis conditions with a short reaction time make the synthesis of Ce-UiO-66-MOFs an attractive subject for research. In this work, five different variations, Ce-UiO-66, Ce-UiO-66-NH$_2$, Ce-UiO-66-Br, Ce-UiO-66-COOH and Ce-Ui-66-NO$_2$ were synthetised according to Dai *et al.* article[76] (2023) with synthesis codes EBP-069–072 and EBP-078 respectively (Table 8). The reaction mechanism with the desirable structure are presented in Figure 33 using BDC-based tagged ligand as an example. The reaction for BTC-ligand follows the same procedure.
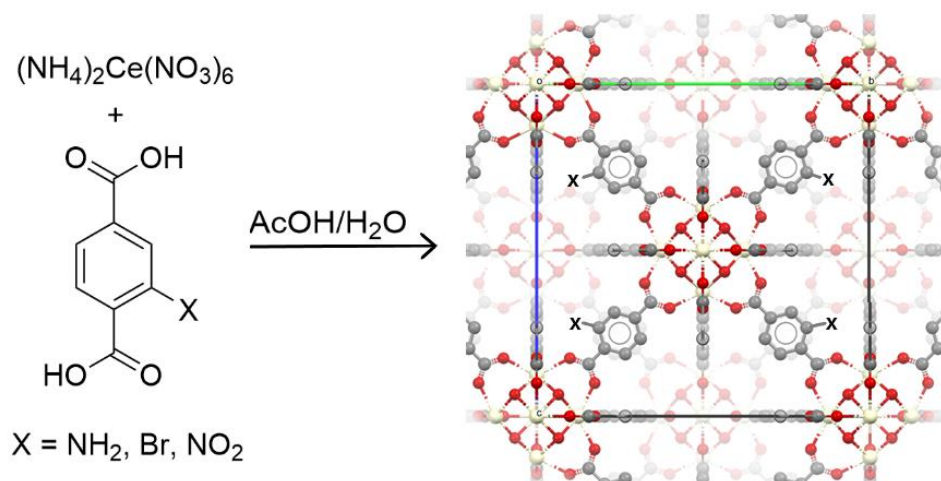

Figure 33. The synthesis of Ce-UiO-66-X using tagged BDC ligands.

Table 8. The synthetised structures, synthesis codes and solvents and the weighed masses of reagents of the Ce-UiO-66-MOFs.

Synthetised structure	Synthesis code	Solvents	Weighed mass of $(NH_4)_2Ce(NO_3)_6$	Ligand and the weighed mass (1.5 mmol)
Ce-UiO-66	EBP-069	H_2O, EtOH	821.7 mg	BDC (249 mg)
	EBP-069-b	H_2O, EtOH	821.3 mg	BDC (249.2 mg)
Ce-UiO-66-NH₂	EBP-070	H_2O, EtOH	820.4 mg	NH_2-BDC (272 mg)
Ce-UiO-66-Br	EBP-071	H_2O	821.5 mg	Br_2-BDC (366.7 mg)
Ce-UiO-66-COOH	EBP-072	H_2O	820.6 mg	BTC (366.7 mg)
Ce-UiO-66-NO₂	EBP-078	H_2O	820.1 mg	NO_2-BDC (316.7 mg)

A theoretical mass of 820 mg (1.5 mmol) of $(NH_4)_2Ce(NO_3)_6$ was weighed for every synthesis (Table 8) in beakers with 3 ml of acetic acid as a modulator and 8 ml of deionised water. In addition, 20 ml ethanol was added in the mixtures of EBP-069 and EBP-070. After stirring the mixtures, 1.5 mmol of the corresponding ligand shown in Table 8 was added to the solution. The mixtures got cloudy right after the addition of the ligands (Figure 34), and they were stirred in a room temperature for 2 h. The products were collected by centrifugation and after collection, they were filtered with suction and washed with distilled water and ethanol. The product EBP-069 leaked through the glass sinter and was therefore washed with the centrifuge distributed in two separate 15 ml tubes with 10 ml water and 10 ml ethanol in each. After drying in a desiccator for 24 h, the products were weighed, and their masses were 493.8 mg for EBP-069, 158.8 mg for EBP-070, 587.7 mg for EBP-071, 573.9 mg for EBP-072 and 577.2 mg for EBP-078.

According to the measured PXRD pattern (Figure 35), the EBP-069 contained terephthalic acid (refcode TEPHTH01[82]) as a residue. Therefore, a new batch (EBP-069-b) was synthetised similarly as before but was also washed with 7 ml of DMF in each tube. The mass of EBP-069-b was 316.0 mg. However, the terephthalic acid peaks did not disappear from the PXRD pattern,

and the sample gave identical peaks with the EBP-069. The PXRD pattern of EBP-069-b has therefore been omitted from the work for a better readability of the results.

Figure 34. Ce-UiO-66-MOF-solutions from the left to right: EBP-069, EBP-072, EBP-071 and EBP-070.
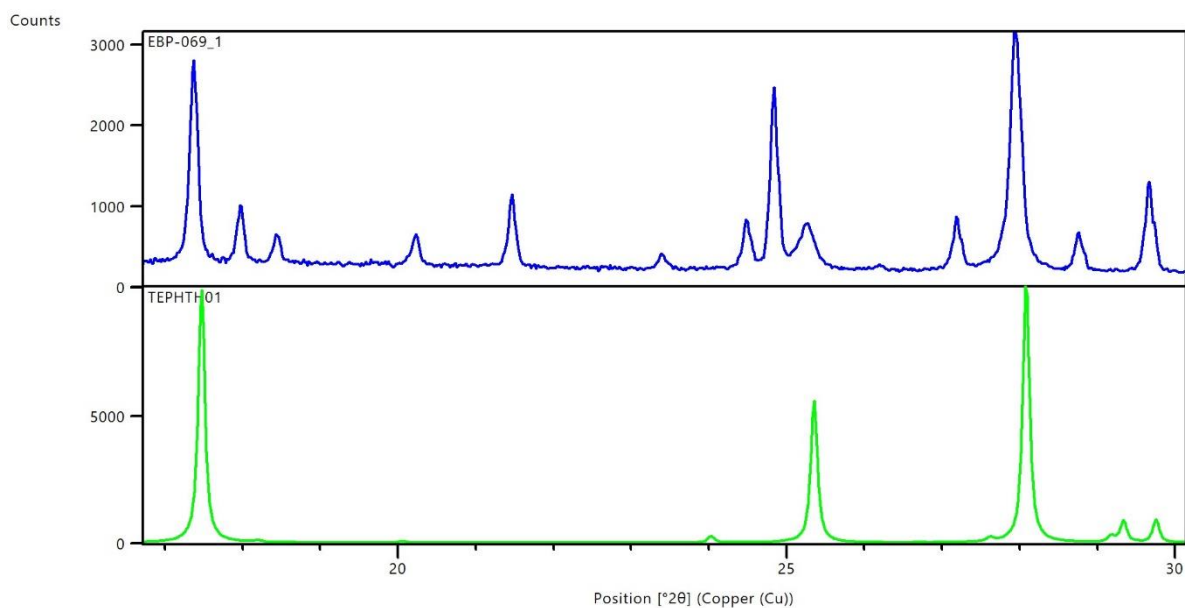
Figure 35. The comparison of PXRD patterns of EBP-069 (Ce-UiO-66) and TEPHTH01[82], terephthalic acid retrieved from the PDF-4+ database.

PXRD measurements were performed for all the Ce-UiO-66 samples (Figure 36) with a measurement range of 3–60° 2θ and a step time of 40–45 sec. All the measurements gave peaks with almost identical values of angles – without taking into account the terephthalic acid visible on EBP-069 pattern – with highest intensities on the peak couple between 7–9° 2θ, and EBP-

070 (NH₂-BDC) and EBP-072 (BTC) being the most amorphous of the five. For EBP-070 the step time of 40 sec gave too low intensity peaks, so the measurement was repeated, and the diffraction patterns were combined with a simple sum-function (EBP-070_1_070_2_SS). The Ce-UiO-66-COOH was compared with a corresponding structure, Ce-UiO-66-BDC, from the PDF-4+ database with a reference code BUPVIT (Lammert *et al.* 2015[83]) (Figure 37). Even if the functional groups of the EBP-070 and BUPVIT differ from each other, the similarity of the PXRD patterns can be explained with the coordination geometry of the groups causing no prominent differences with the crystal structure. This is, because the functional groups form no additional bonds in the structure (Figure 33), implying, that the syntheses of Ce-UiO-66 structures led to a formation of isoreticular MOFs.

Figure 36. PXRD patterns of synthetised Ce-UiO-66-MOFs with different functional groups on a measurement range of 0–28° 2θ: Ce-UiO-66 (blue), Ce-UiO-66-NH₂ (turquoise), Ce-UiO-66-Br₂ (red), Ce-UiO-66-COOH (black) and Ce-UiO-66-NO₂ (green).
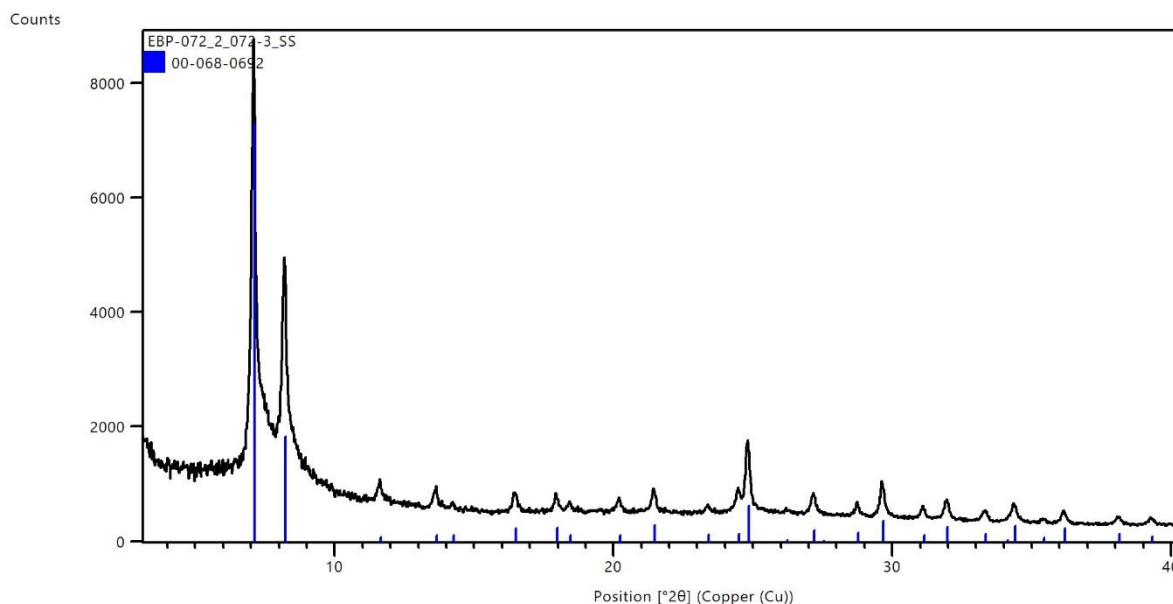
Figure 37. The measured PXRD pattern of Ce-UiO-66-COOH on a measurement range of 0–40° 2θ and the peaks of a corresponding reference pattern with the code BUPVIT retrieved from the PDF-4+ database.
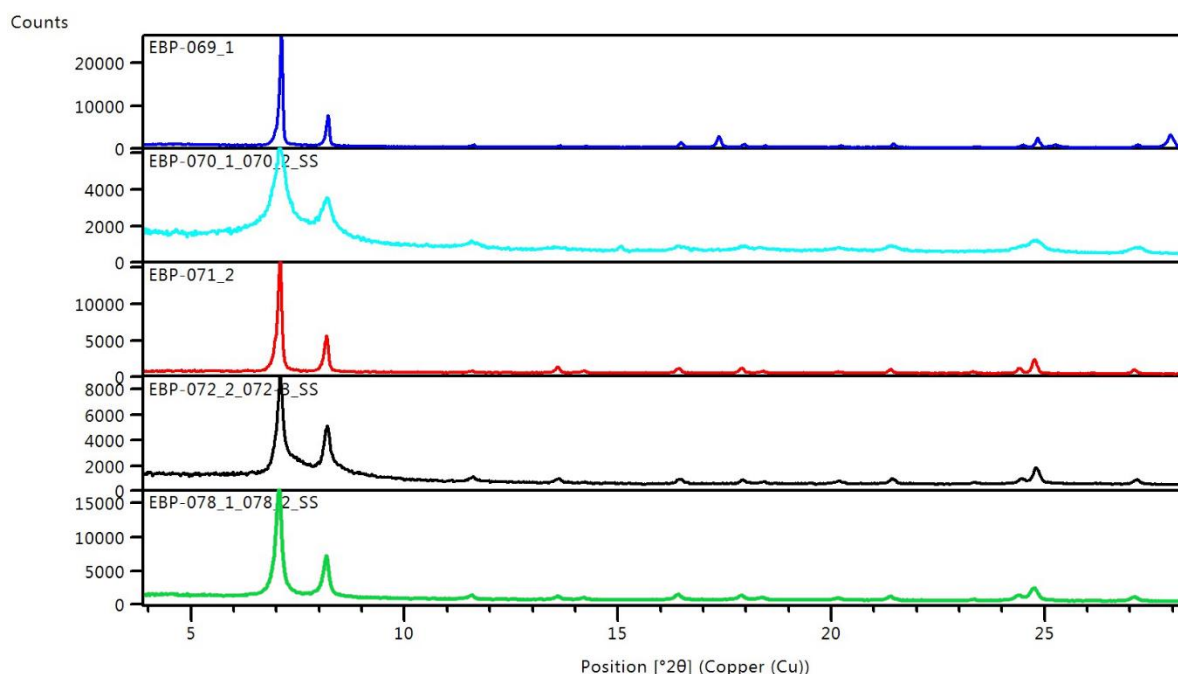
Thermogravimetric analyses were performed to determine the thermal stability of the Ce-UiO-66 structures (Appendix 5, Figure 38 a, Figure 39, Table 9). Comparing the EBP-069 (BDC) and EBP-069-b (BDC), (Figure 38 a) with the different washing treatments of the synthetised products seemed to be affecting to the thermal behaviours of both samples. The TG curve of the EBP-069 sample is noticeably steeper in the beginning, with a two-step mass loss of 24.17 wt.-%. Generally, in MOFs, solvents cover one fourth of the mass of the compound due to the large porosity. Therefore, the mass loss can correspond to the evaporation of ethanol, water, acetic acid and probably even esterified acetic acid (ethyl acetate), which could along with water explain the magnitude of the mass loss around 80 °C. The bump at the onset temperature 191 °C can, for example, correspond to the slow evaporation of the residual terephthalic acid. The actual decomposition of the MOF (40.45 wt.-%) occurs in an exothermic combustion reaction at 349 °C leaving behind a residual mass of 35.13 wt.-%.

When it comes to EBP-069-b, the beginning of the curve is less steep, the first step being 8.76 wt.-% compared to the first step of EBP-069, 17.30 wt.-%, which is probably because of the DMF wash had replaced the ethanol and water. However, after a temperature of 165 °C, the curve steepens unlike in the EBP-069 curve, where possibly the terephthalic acid fills the curve creating a hill, which could refer, that the EBP-069-b contained less terephthalic acid residue.

After the analysis, white substance had deposited on to the top lid of the TG furnace (Figure 38 b), which corresponds to the colour of, for example, terephthalic acid, but could not be further identified without elemental analysis. The main decomposition of the sample occurs at 364 °C after solvent evaporation of 23.31 wt.-%, leaving behind a residual mass of 31.99 wt.-%. The mass percentage of the solvents, also the decomposition temperature and residual mass are near to the corresponding values of the equivalent compound EBP-069.
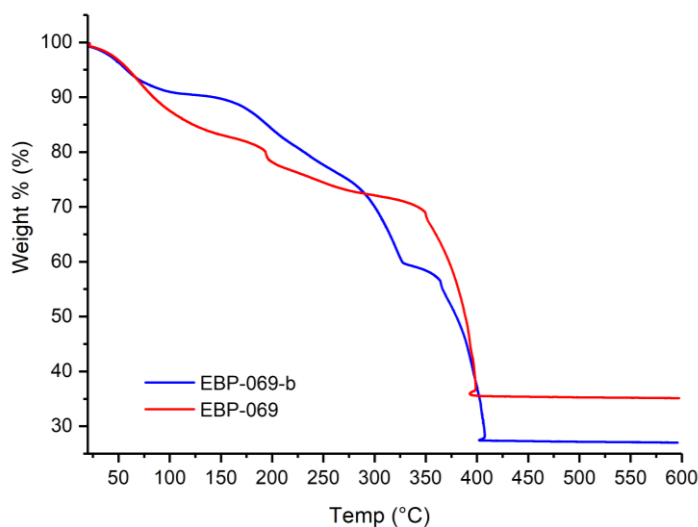
Figure 38. a) The TG curves of EBP-069 and EBP-069-b and b) White decomposition product of EBP-069-b.

According to the TG/DSC-curve of EBP-070 (NH$_2$-BDC, Figure 39), the mass loss of the solvent evaporation was a similar to that of the two-step event on the EBP-069-b – first step starting at 40 °C and the second at 146 °C – but covered only 13.38 wt.-% of the sample, which is a little lower than what could be expected. The main decomposition of the product (52 wt.-%) occurred in 264 °C, which is slightly lower temperature than what is usually observed for UiO-66-MOFs, but it is known that NH$_2$-group is somewhat more prone to be thermally decomposing functional group and by that lowering the thermal decomposition of the MOF. The thermal decomposition was so highly exothermic, that the heat exceeded the nominal heating rate of the TG/DSC device causing overheating. The residual mass of the sample was 34.49 wt.-%.
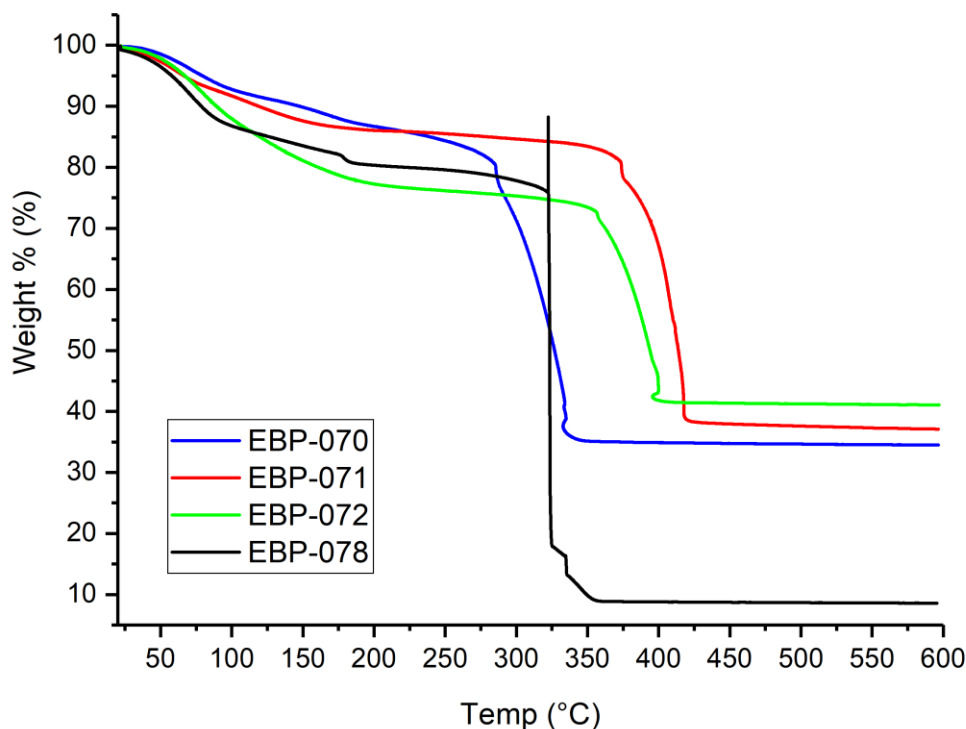
Figure 39. The TG curves of the synthetised Ce-UiO-66-MOFs except of the EBP-069 samples for the better readability: Ce-UiO-66-NH$_2$ (blue), Ce-UiO-66-Br$_2$ (red), Ce-UiO-66-COOH (green) and Ce-UiO-66-NO$_2$ (black).

According to the curve of EBP-071 (Br$_2$-BDC, Figure 39), the evaporation of the water and ethanol was strong with a mass loss of 6.67 wt.-% before 87 °C. In the second step the curve still decreases (6.87 wt.-%), but more gently reaching a temperature of 213 °C, which probably represents the removal of the rest of the water among other possible volatile residues. What is interesting in the thermal behaviour of the sample is, that the main weight loss (354 °C, 48.85 wt.-%) does not occur in significantly higher temperature, than for example on the Ce-UiO-66 sample (EBP-069-b) but lower, even though bromine is known as stabilizing component in MOF structures according to the literature[73]. This could suggest, that as the functional group of the BDC does not create covalent bonds to the adjacent atoms (Figure 33), it also would not affect the thermal stability. Actually, in terms of the functional groups, the cause of the thermal stability differences of Zr-UiO-66 were already studied in 2010 by Kandiah's group[73], where, in addition to the electronic effects, the steric hindrance of the functional groups was considered separate effect. All in all, Kandiah's group stated, that neither steric, nor electronic properties of the functional groups of a BDC linker alone affect the thermal stability of UiO-66-MOFs.

The residual mass of the EBP-071 according to the TG/DSC curve of the compound was 37.09 wt.-%.

The EBP-072 (BTC) sample contained the highest solvent content according to the TG curve (Figure 39), which had only two steps. First occurred as the larger step with a mass loss of 75.29 wt.-%. The magnitude of this dehydration step could be due to the strong hydrogen bonding between the three carboxylic acid groups of the BTC ligand and water and EtOH molecules in the pores, which had thus not been able to evaporate in the drying of the product. In the temperature of 351 °C the compound decomposed in a rapid, exothermic burning reaction causing an overheating bend to the curve. The residual mass of the compound was 41.06 wt.-%.

According to the curve of EBP-078 (NO_2-BDC, Figure 39), the dehydration process was similar to the other BDC containing MOF-series with a two-step mass loss of 18.73 wt.-%. However, there can be seen a small endothermic bump in a temperature of 176 °C, which could refer to a melting of ammonium nitrate (melting point 169 °C), but only if there was some residual ceric ammonium nitrate left in the compound, that could have been decomposed. The NO_2 group is extremely prone to explode in high temperatures, and in 354 °C the TG-curve jumps rapidly creating a sharp exotherm on the DSC-curve due to the possible detonation. The event was also visible after the measurement as burnt, black organic substance on the top lid of the TG furnace (Figure 40). The residual mass of the sample was clearly the lowest for all Ce-UiO-66 samples, being only 8.59 wt.-%. This might be for example because of the detonation.
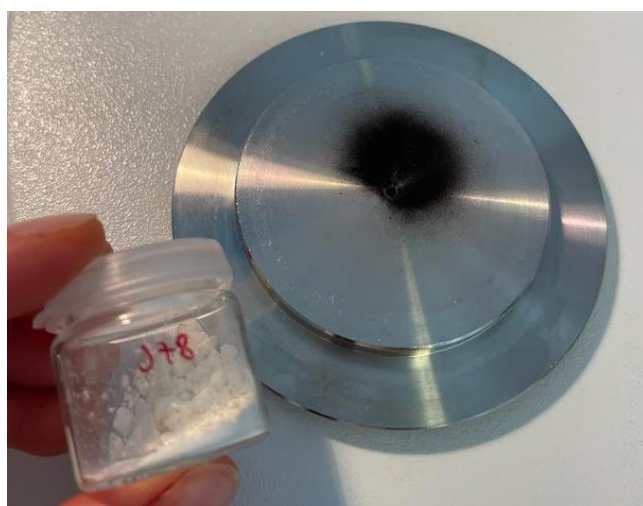
Figure 40. The burnt organic decomposition product of the EBP-078 on the top lid of the TG furnace.

Table 9. The mass losses, residual masses and extrapolated onset temperatures of the thermal decomposition determined for the synthetised Ce-UiO-66 typed MOFs.

Compound	Mass losses wt.-%, (T-range) (%), (°C)	Residual mass wt.-%, (T) (%), (°C)	T_d (°C)
EBP-069	17.30, (22–165)		45*
	6.86, (165–235)		81*
	40.45, (236–597)	35.13 (597)	349
EBP-069-b	8.76, (23–127)		35*
	14.55, (127–267)		165*
	16.75, (267–341)		290
	31.99, (341–596)	27.03, (596)	364
EBP-070	8.00, (22–114)		40*
	5.38, (114–206)		146*
	52.00, (206–597)	34.49, (597)	264
EBP-071	6.67, (22–87)		35*
	6.87, (87–213)		
	48.85, (213–596)	48.85, (596)	354
EBP-072	24.63, (22–300)		42*
	34.24, (300–597)	41.06, (597)	351
EBP-078	16.91, (23–172)		43*
	1.82, (172–193)		176
	71.89, (193–596)	8.59, (596)	322

T_d = The extrapolated onset temperature of the thermal decomposition.

* = The extrapolated onset temperature for desolvation/dehydration.

9.5 FTO substrates

In the experiments, fluorine-doped tin oxide glasses from two different manufacturers were used. The substrates from Redoxme were 25 mm x 25 mm x 2.2 mm, with a resistivity of 7–10 Ω/square. The Ossila substrates (S301 TEC 8) were 20 mm x 15 mm x 2.2 mm with a resistivity of 6–9 Ω/square. PXRD-patterns of both manufacturers' substrates were measured in a measurement range of 3–70° 2θ with a step time of 180 sec for a better distinguishment of the peaks from the synthetised products on top. The appeared peaks can be seen in Figure 41, and they correspond to the characteristic diffraction peaks of SnO_2 with a reference code of 04-008-4169[84]. Based on the PXRD analysis, the crystallinity of substrates could also be compared, but from the similar peaks of the samples it was observed, that both substrates represented a similar crystallinity.
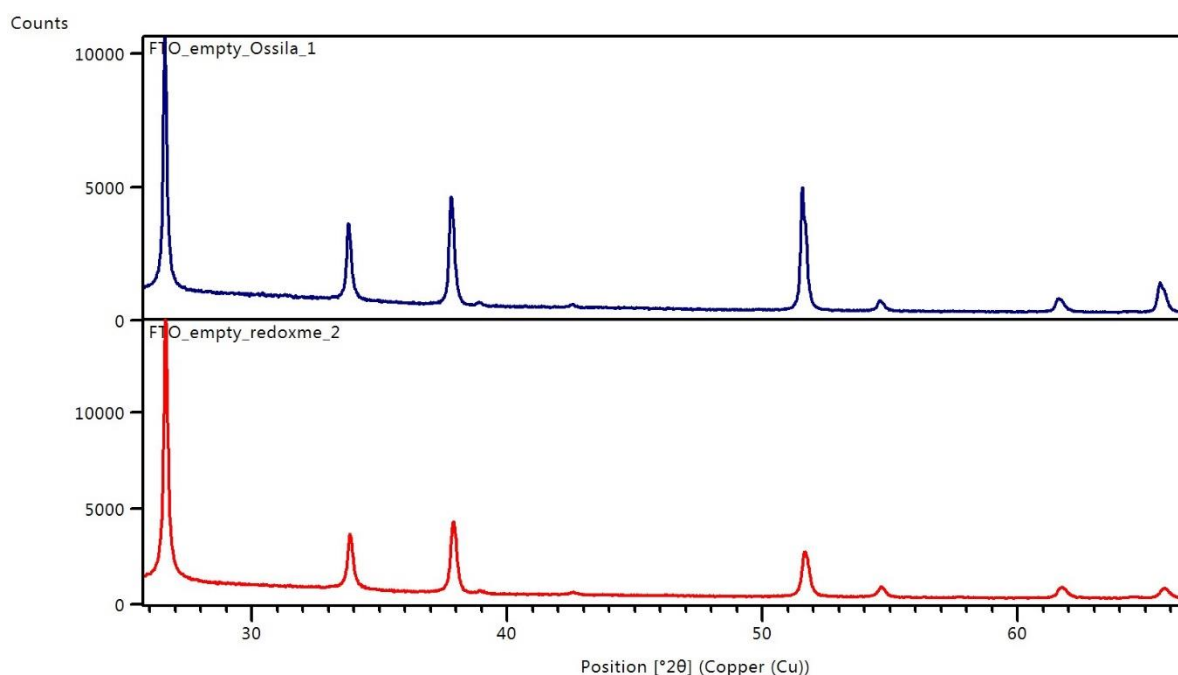
Figure 41. Diffraction patterns of the pristine FTO substrates: Ossila (top), Redoxme (below).

NH₂-MIL-125/TiO₂-nanorods on FTO

A 25x25 mm^2 piece of Redoxme FTO substrate was cleaned ultrasonically in a 30 ml mixture containing deionised water, acetone, and 2-propanol (IPA) with volume ratios of 1:1:1. A

hierarchical layer of TiO_2 nanorods (EBP-073) was synthetised by a hydrothermal synthesis according to the article of Wang *et al.* (2011)[77]. After purification the piece was put in a 50 ml Teflon-lined autoclave, the conductive side facing down in a solution containing 12 ml of deionised water, 12 ml of concentrated hydrochloric acid (37 m-%) and 0.4 ml of titanium butoxide (TBT), which were combined with a 5 min stirring. The mixture was heated in an oven at 150 °C for 18 h, and after cooling the sample piece was washed with deionised water and dried in ambient air. The dried substrate was then immersed in 0.2 M $TiCl_4$ in a tightly sealed container and was left there overnight for the aqueous chemical growth of hierarchical TiO_2 nanostructures. The sample had then developed a white layer on the conductive side and was finally washed with ethanol and dried in an oven in 50 °C. Nonetheless, the FTO film with the white layer on top was peeled off during the drying process (Figure 42). It could be a result of poor washing of the $TiCl_4$, or a manufacturing defect in the FTO substrate.

Figure 42. The partially peeled layer of the FTO film in the synthesis of EBP-073.

The PXRD pattern of the EBP-073 sample was measured and the peaks corresponded to two structures found from the PDF-4+ database: SnO_2 (refcode 04-008-4167) from the FTO glass and TiO_2 (refcode 04-006-1919). The peaks of TiO_2 suggest, that even though the coating peeled off, the synthesis of the TiO_2 nanolayer was somewhat successful – if not as a nanorod layer, then in some other morphology. The PXRD pattern of the sample and the correspondences to the characteristic diffraction peaks of the identified phases are presented in Figure 43.
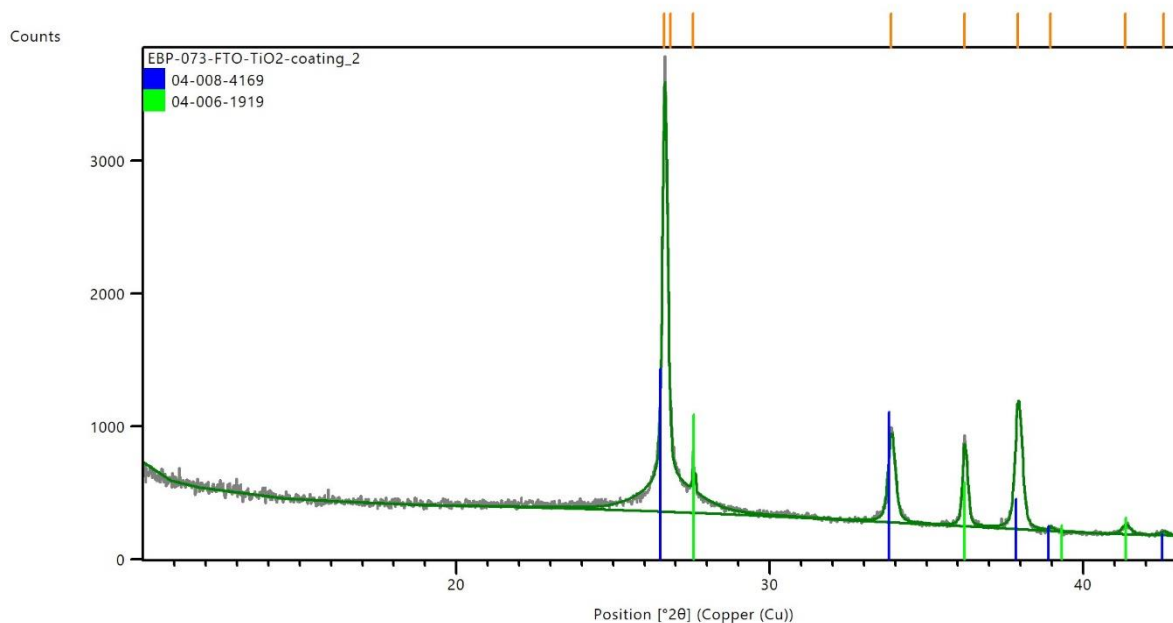
Figure 43. PXRD pattern of EBP-073 and the correspondences to the characteristic peaks of SnO$_2$ (blue) and TiO$_2$ (green).

Au@NH$_2$-MIL-125 nanocomposite on FTO

As Au NPs don't only have a localized surface plasmon resonance (LSPR) and thus a strong visible light absorption, but also a capability to catalyse water oxidation reaction, a NH$_2$-MIL-125 sensitized TiO$_2$ coating was chosen to be further doped with Au NPs according to the Zhang *et al.* article (2015).[43] First, two FTO substrates, each from the different brand were cleaned with 30 min ultrasonication in a mixture of deionised water, acetone, and 2-propanol with a volume ratio of 1:1:1. Both cleaned substrates were put in 100 ml Teflon-lined autoclaves in 6 M HCl solutions containing 0.83 ml of TBT, which were mixed together with 5 min stirring. The hydrothermal syntheses of TiO$_2$ nanowire arrays were conducted in oven at 150 °C for 5 h. The coated substrates were then rinsed with deionised water and dried under flowing nitrogen in a Schlenk line overnight. The dried nanowire arrays were then kept in 450 °C for 30 min for a better conductivity.

The dried TiO$_2$ nanowire arrays were then modified with BDC-NH$_2$. The pieces were immersed in beakers containing 4 ml solutions of 20 mM BDC-NH$_2$ – with weighed mass of 0.0146 g for both – and kept in 120 °C for 3 h. During this step, the solution of EBP-074 mixture had completely evaporated and the sample was dry when taken out of the oven. This was due to the

mistake of not putting, for example, a glass watch on top of the beakers to prevent the evaporation.

To grow the MOF, the pieces were put in a 50 ml Teflon-lined autoclave with 25 ml of MeOH/DMF solution with volume ratio of 9:1, where 0.2713 g (1.5 mmol) of BDC-NH$_2$ and 130 µl of TBT were mixed in. The mixture was kept in 150 °C for 69 h. After solvothermal process, a yellow precipitate, possibly 2-aminoterephthalic acid residues were shown on the surface of the substrates and the pieces were washed twice with methanol, but the yellow substance did not come off entirely. After the wash, the nanocomposites were preheated in 120 °C for 20 h for the further Au NP decoration.

For Au NPs, 0,0156 g (0.04 mmol) of HAuCl$_4$ was mixed into 20 ml of MeOH and the composites were kept in the solution conductive side up for 3 h in room temperature. After washing with MeOH and drying, a 0.2 M NaBH$_4$/MeOH-solution was prepared by weighing 0.1514 g of NaBH$_4$ into 20 ml of MeOH for a gold precursor reduction. Immediately, the mixture started to react and bubble, and the samples were immersed in the solution and were kept in the mixture for 5 min. Finally, the pale-yellow samples (EBP-074 on Redoxme & EBP-075 on Ossila) (Figure 44) were washed with methanol and left to dry in a desiccator.
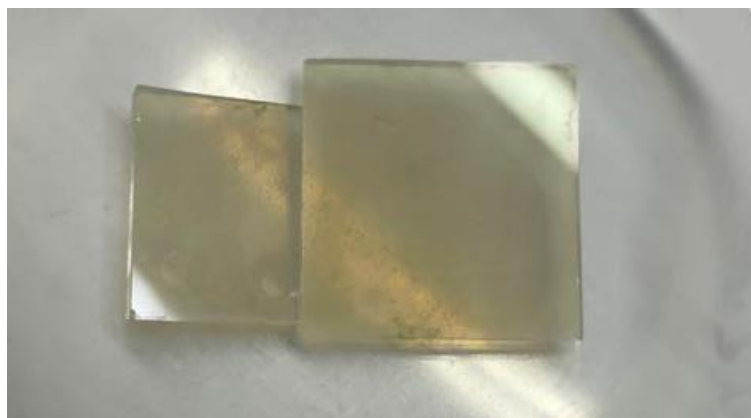
Figure 44. Au@NH2-MIL-125 nanocomposites on FTO substrates. EBP-074 on the right and EBP-075 on the left.

With the same technique, two FTO substrates were coated without the Au nanoparticles (EBP-076 and EBP-077) for a comparison. In the BDC-NH$_2$-modification of TiO$_2$ nanowire arrays, 0.0145 g and 0.0144 g of the BDC-NH$_2$ were weighed for the 20 mM solutions in the beakers with the substrates, respectively. After, for the MOF-growth solution, 0.2716 g (0.5 mmol) of BDC-NH$_2$ was weighed in the Teflon-lined autoclave containing 9:1 MeOH/DMF solution with 130 µl TBT. Both of the substrates were immersed into the same solution and the

mixture was kept in 150 °C for 60 h. Again, after the reaction, yellow stains were left on the surfaces of the samples and assuming that it was from the 2-aminoterephthalic acid, the samples were washed with DMF in addition to methanol, but the yellow colouring did not come off. After the washing, the samples were left to dry into a desiccator.

All the NH_2-MIL-125 samples, with and without the Au NPs were measured with PXRD, and most of the peaks corresponded to the peaks of the pristine FTO substrates. The few additional peaks in each pattern in the range of 5–20° 2θ did not give enough information for their identification, even though it has been reported, that the strongest peaks of the PXRD pattern of NH_2-MIL-125 should locate on that area (Zhang *et al*. 2021[85]). According to the Zhang's group, the Au NPs should have also given visible signals to the pattern. Therefore, it can be assumed, that the Au NPs did not attach to the structure. The PXRD-patterns for Au@NH_2-MIL-125 and NH_2-MIL-125 nanocomposites in a measurement range of 0-67° 2θ are shown in Figure 45.
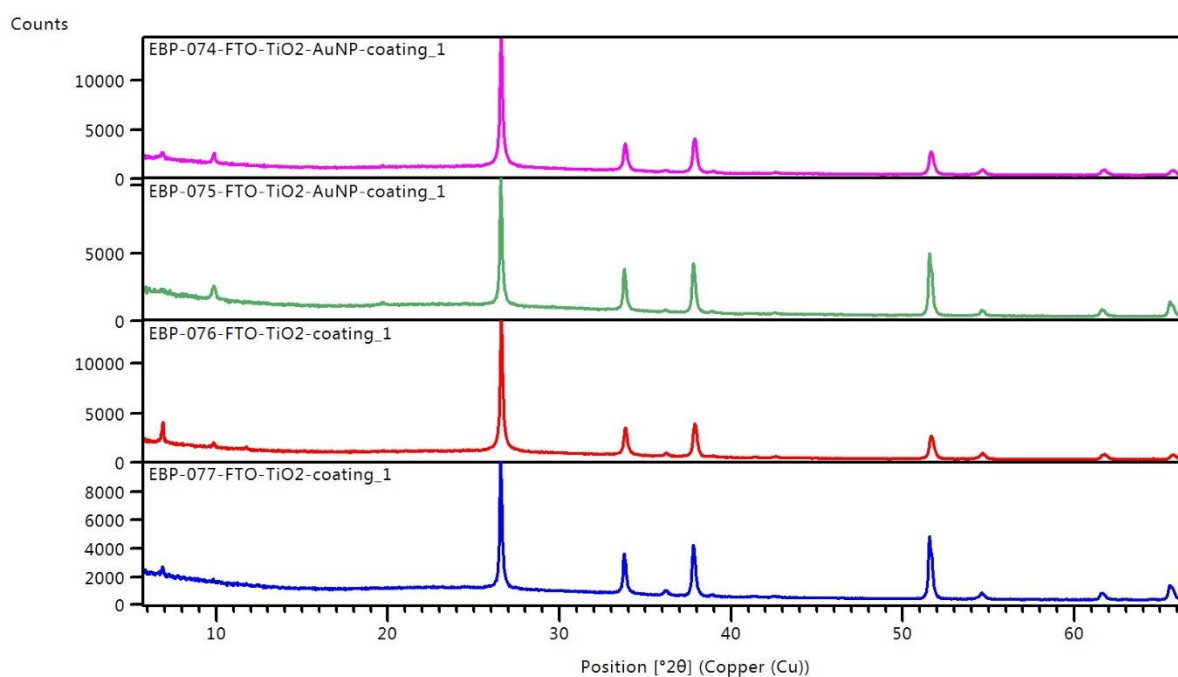
Figure 45. The PXRD-patterns of Au@NH_2-MIL-125 and NH_2-MIL-125 nanocomposites.

For SEM images, the EBP-075 sample was coated with gold for four minutes. However, the images were unclear, and based on the clearest image chosen (Figure 46) it reveals only very few usable details about the content of the prepared sample. In the figure, only particles with a varying diameter of few micrometres with irregular shapes can be distinguished and from this

information, they can only be assumed to be the MOF particles. Expectedly, the size of the Au NPs, on the other hand, is so small, that they were not to be seen in the SEM images.
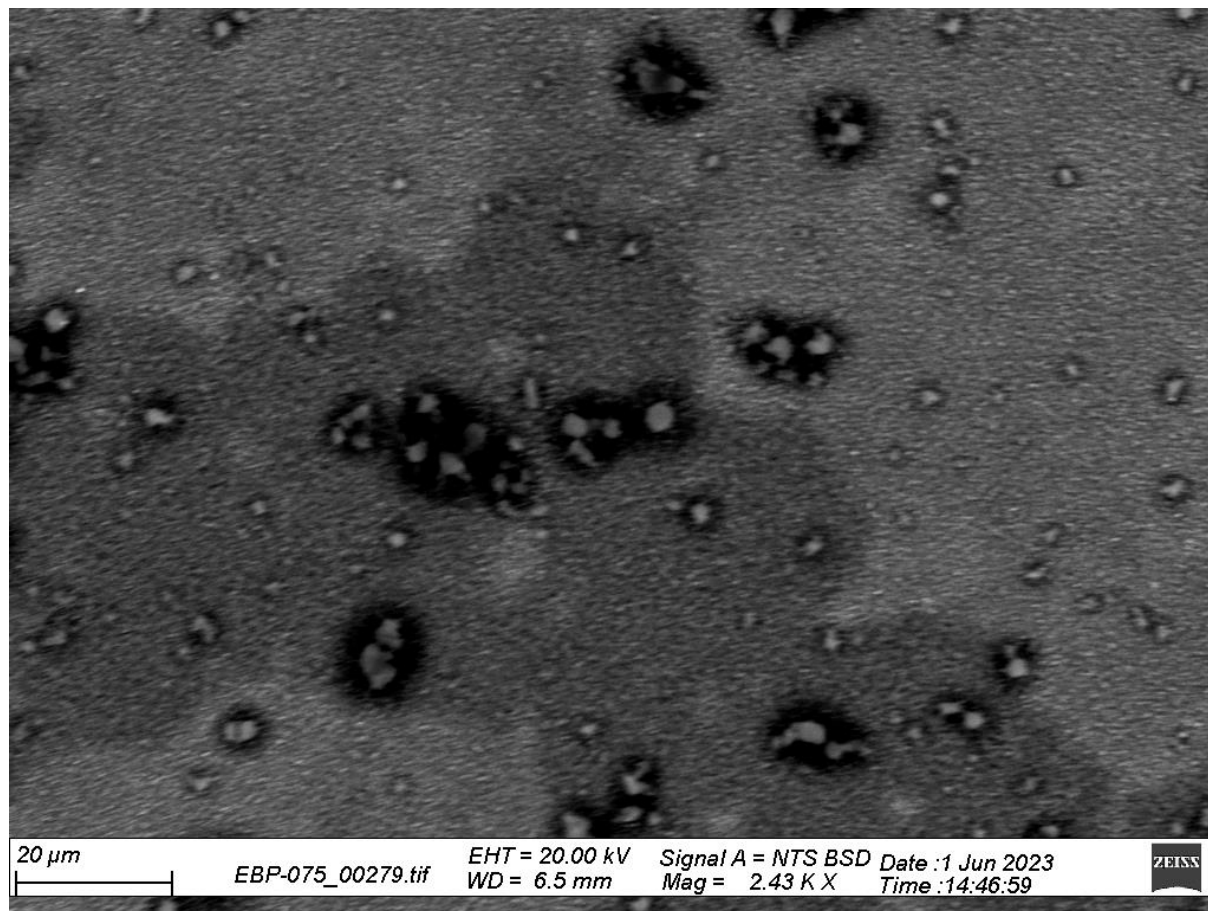
Figure 46. The SEM image of the surface of EBP-075.

The SEM image showing the surface of EBP-076 (Figure 47. a) reveals two kinds of particles: round, and flat, disk-like grains with a diameter of approximately 500 nm on a bed of small and thin rod-like particles (i.e. nanorod arrays). According to Ding *et al.* (2019)[86] (Figure 47. c–d), the round particles correspond to the morphology of the NH$_2$-MIL-125-MOF in addition to the reported average size of 700 nm. The nanorod arrays of EBP-076 correspond to the shape and size of the TiO$_2$ nanorod arrays reported by Gao *et al.* (2023)[87] (Figure 47. b). According to the visual comparisons, the synthesis of the coating seems to have been successful.
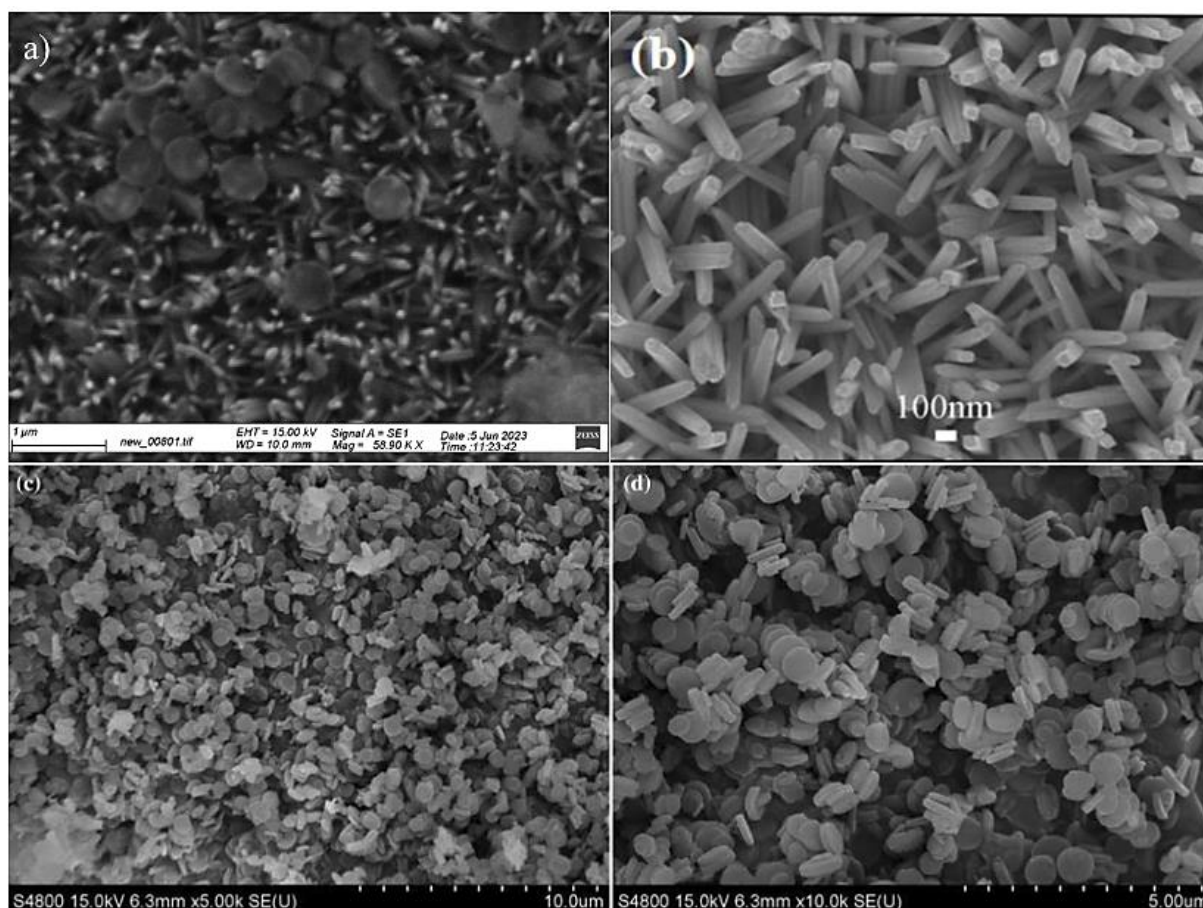
Figure 47. a) The SEM image the surface of EBP-076 sample, b) the previously reported image of TiO$_2$ nanorod arrays (Gao *et al.* 2023)[87] and c) – d) the previously reported images of NH$_2$-MIL-125(Ti) particles (Ding *et al.* 2019)[86].

The SEM-EDX analyses were performed for the samples EBP-076 (Appendix 8, Figure 48, Table 10) and EBP-077 (Appendix 9, Figure 49, Tables 11 and 12). From the image of EBP-076 it can be seen, that the surface of the FTO is quite smooth and according to the EDX analysis, it contains a lot of tin originating from the tin oxide coating (48.21 wt.-%, 12.39 at.-%), oxygen (38.54 wt.-%, 73.50 at.-%) and titanium (9.11 wt.-%, 5.80 at.-%), which refers, that there could be low concentrations of TiO$_2$ nanorods on the SnO$_2$-coating of the substrate. The signal of Si (0.84 wt.-%, 0.91 at.-%) comes from the glass substrate. The other elemental concentrations, however, are too low for further reliable information, but the results do show small amounts of nitrogen and carbon, which could refer to the appearance of NH$_2$-MIL-125 or its precursors.
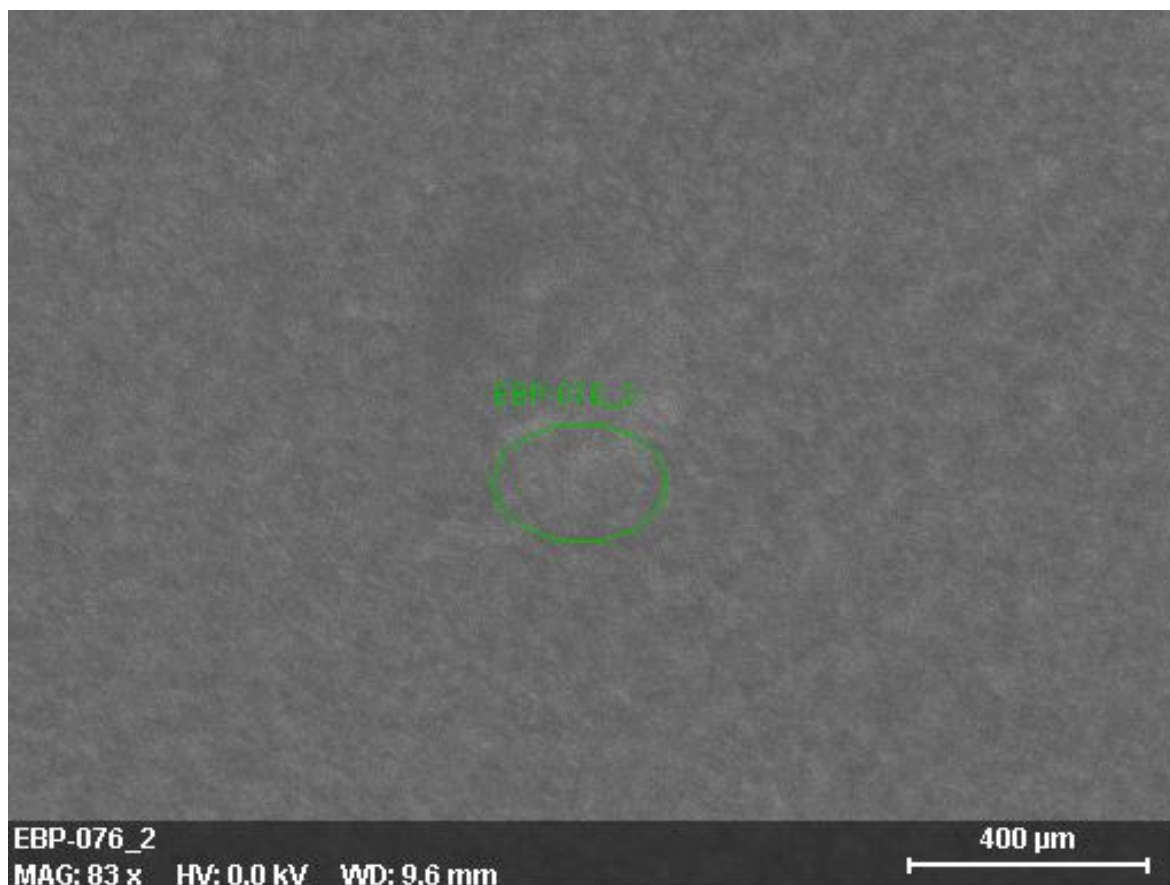
Figure 48. SEM image of EBP-076 surface and the marked area for EDX.

Table 10. The EDX signals of the area of EBP-076 surface.

Element	Atomic number	Series	norm. C [wt.-%]	Atom. C [at.-%]	Error [%]
Sn	50	L-series	48.21	12.39	1.5
Ti	22	K-series	9.11	5.80	0.4
N	7	K-series	2.74	5.96	1.3
Si	14	K-series	0.84	0.91	0.1
C	6	K-series	0.57	1.44	0.3
O	8	K-series	38.54	73.50	6.3
Total:			100 %	100 %	

norm. C [wt.-%] = normalised concentration in weight percent of the element

Atom. C [at.-%] = atomic concentration in weight percent of the element.

From the images of EBP-077 it can be seen that the coatings have not been equally distributed on the FTO surface. According to the results of the EDX shown in the Table 11, the particles on the left of the image (Figure 49 a) seem to be mainly SnO_2 originating from the FTO, and

since the concentration of titanium is a bit higher on the right side of the image (Table 12, Figure 49 b), it can be assumed, that the area contains possibly more TiO_2 nanorod arrays. Based on the Tables 11 and 12, also the concentration of nitrogen is a little bit higher on the TiO_2-rich area, where the MOF is supposed to be attached more easily in contrast to the area on the left, which is assumed to contain less TiO_2. However, the differences between the concentrations of the elements of NH_2-MIL-125 are so small, that no reliable conclusions can be made on them.
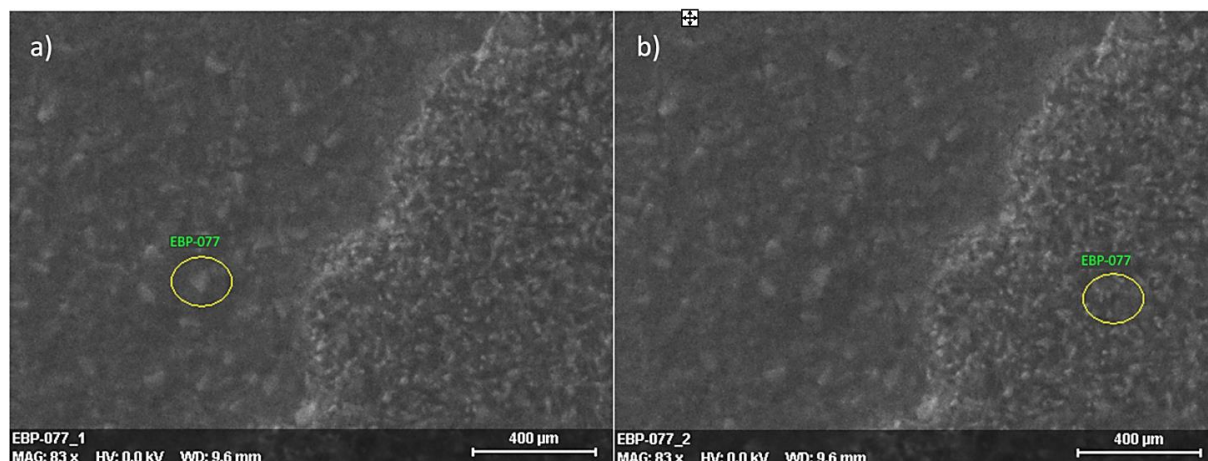
Figure 49. SEM images of EBP-077 surface. a) The marked area for EDX on the surface with larger particles and b) the area for EDX on the surface with smaller particles.

Table 11. The EDX signals of the area with larger particles on the EBP-077 surface.

Element	Atomic number	Series	norm. C [wt.-%]	Atom. C [at.-%]	Error [%]
Sn	50	L-series	56.59	15.41	1.6
Ti	22	K-series	2.51	1.70	0.3
N	7	K-series	1.31	3.03	1.5
C	6	K-series	1.05	2.84	0.4
Si	14	K-series	0.92	1.06	0.1
O	8	K-series	37.60	75.96	6.1
Total:			100 %	100 %	

norm. C [wt.-%] = normalised concentration in weight percent of the element

Atom. C [at.-%] = atomic concentration in weight percent of the element.

Table 12. The main EDX signals of the area with smaller particles on the EBP-077 surface.

Element	Atomic number	Series	norm. C [wt.-%]	Atom. C [at.-%]	Error [%]
Sn	50	L-series	47.11	12.33	2.1
Ti	22	K-series	12.15	7.88	0.7
N	7	K-series	2.76	6.11	3.2
C	6	K-series	0.55	1.41	0.6
Si	14	K-series	0.50	0.55	0.3
O	8	K-series	36.94	71.72	6.7
Total:			100 %	100 %	

norm. C [wt.-%] = normalised concentration in weight percent of the element

Atom. C [at.-%] = atomic concentration in weight percent of the element.

Ce-UiO-66-NH₂ on FTO

It is significantly more energetically favourable to synthetise photocatalytic MOFs in room temperature than solvothermally on elevated temperatures. Room temperature synthetised Ce-UiO-66-MOFs have been reported to have photocatalytic properties; therefore, it can be anticipated, that growing a Ce-UiO-66-NH$_2$-MOF directly on the FTO substrate could be profitable. Two FTO glasses (Redoxme) were cleaned in deionised water-acetone-2-propanol (volume ratio 1:1:1) solution with ultrasonication for 15 min. BDC-NH$_2$-modified TiO$_2$ nanorod layers were then grown on the FTO surfaces with the same procedure, as described for the synthesis of the Au@NH$_2$-MIL-125 nanocomposite. For the nanorods, a 6 M HCl solution with 0.83 ml of TBT was put in a 100 ml Teflon-lined autoclave with the substrates, and the mixture was kept at 150 °C for 5 h. After drying under flowing nitrogen and keeping in an oven at 450 °C for 30 minutes, the substrates were kept in an 8 ml BDC-NH$_2$-DMF solution (0.0289 g, 20 mM) at 120 °C for 3h.

Two NH$_2$-Ce-UiO-66-MOFs were synthetised according to the synthesis of EBP-070, one in a room temperature (EBP-079) and one with 15 min heating at 100 °C (EBP-080). For EBP-079, the weighed mass of (NH$_4$)$_2$Ce(NO$_3$)$_6$ was 820.2 mg (1.5 mmol) and for EBP-080 820.8 mg (1.5 mmol) and they were put in 50 ml beakers with 10 ml of EtOH. The weighed mass of NH$_2$-BDC for EBP-079 was 0.1358 g (0.75 mmol) and for EBP-080 0.1355 g (0.75 mmol). After all the reagents had been added into the mixture, the NH$_2$-BDC-treated FTO substrates were

promptly immersed into the solutions conductive side upwards, in order to enable reactions and bind on the FTO surface. After 10 minutes, the heat plate was turned off, and the EBP-080 mixture was let to cool down slowly on the plate. After the samples had been in the solutions for 2 hours, they were washed with distilled water and ethanol.

After drying, PXRD analyses were made for both samples with data range of 3–70° 2θ and the recorded patterns were compared to a PXRD-pattern of a pristine FTO substrate. Based on the analysis (Figure 50) the Ce-MOFs had not been attached on the FTO surface. However, the MOF peaks have not been visible in some previous experiments either. The only difference between the PXRD patterns of the samples and the pristine FTO substrate was a very low intensity bump on the angle of approximately 36.5° 2θ, in the sample patterns, which is a characteristic angle for one peak of TiO_2 pattern. Because of this, and the fact that there are no large differences between the patterns of SnO_2 and TiO_2 (Figure 43), it is possible, that the TiO_2 layer has attached to the FTO surface. However, since the Ce-UiO-66-MOFs have their strong, characteristic peaks under 10° 2θ and they were not visible in these measurements, the success of the attachment of Ce-UiO-66-MOF cannot be confirmed only by PXRD analysis.
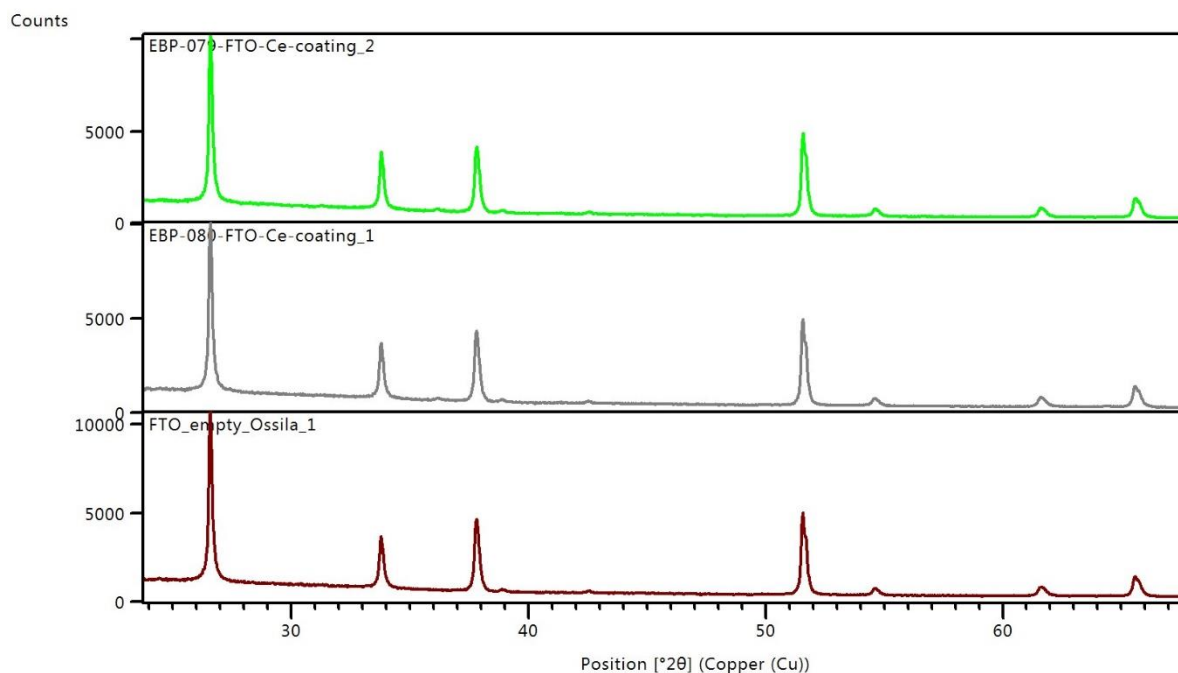
Figure 50. PXRD-patterns of Ce-UiO-66-NH$_2$-MOFs on FTO compared to an empty substrate.

Compared to the SEM-image of UiO-66(Zr) reported by Miyamoto *et al* (2015)[88] (Figure 51), the particles on the EBP-079 sample (Figure 52) appear to have the same octahedral-like morphology as the reported UiO-66(Zr) MOF. According to the EDX analysis (Appendix 10,

Figure 53, Tables 13 and 14), it seems that cerium is not attached to the structure, and this indicates, that the particles on the surface of EBP-079 would not be the Ce-UiO-66 structure. However, based on the reactants and the particle morphology seen in the image, it can be assumed, that the synthetised structure on the FTO substrate has to be the Ce-UiO-66-MOF. The reason why cerium signals do not appear in the EDX measurements may be caused by the low sensitivity and resolution of the EDX method. Elements that indicate to the TiO_2-coating were also distinguished in addition to the SnO_2 layer of the substrate. The large concentration differences between tin (43.71 wt.-%, 9.70 at.-%, Table 14) and titanium (3.02 wt.-%, 1.66 at.-%, Table 14) are possibly due to the fact that the tin oxide layer of the substrate is in a macro scale, and the TiO_2 is supposed to be in a nano scale. The high concentration of the tin can also explain the lack of the TiO_2 layer peaks in the PXRD measurements, because if the synthetised TiO_2 layer would be thicker and denser, there could possibly have been an intensity difference between the patterns including the TiO_2 layer and pristine substrate. In addition, darker and lighter areas were found on top of the sample EBP-079, which according to the EDX analyses for the lighter area contain higher levels of titanium (3.02 wt.-%, 1.66 at.-%, Table 14), whereas the darker areas show only trace amount of titanium (0.29 wt.-%, 0.17 at.-%, Table 13). This indicates, that the TiO_2 nanorods have not been evenly distributed on the substrate. The EDX analysis of EBP-080 (Appendix 11, Figure 54, Table 15), on the other hand, showed similar results, but distinctly more carbon (9.56 wt.-%, 20.32 at.-%) compared to the EBP-079 signals (3.64 wt.-%, 7.97 at.-%, Table 14).
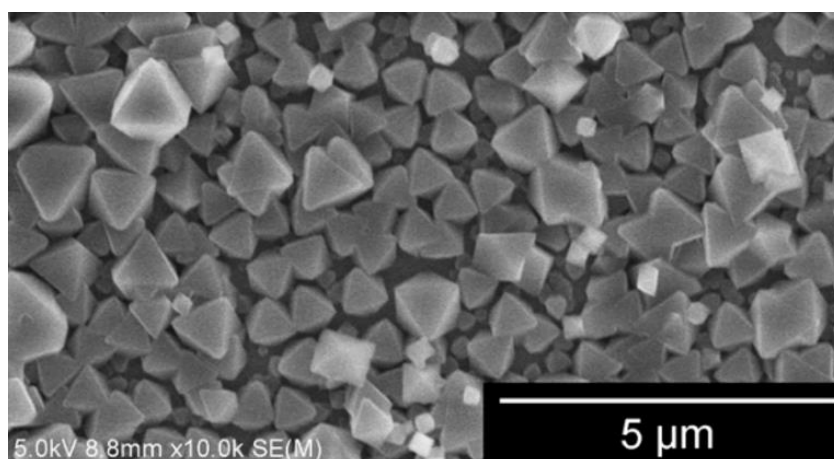
Figure 51. A previously reported SEM image of UiO-66 (Miyamoto *et al.* 2015).[88]
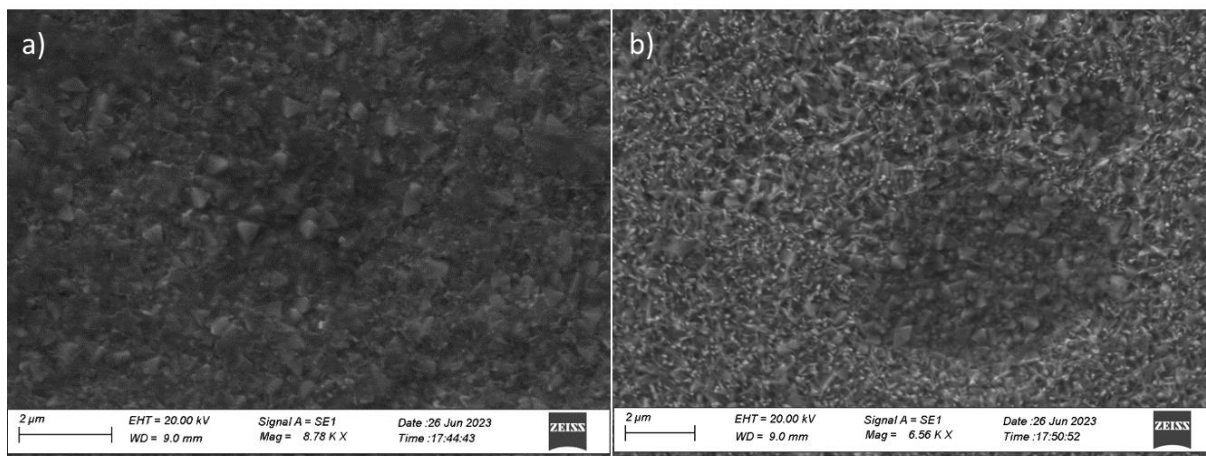
Figure 52. SEM images of the surface of EBP-079.
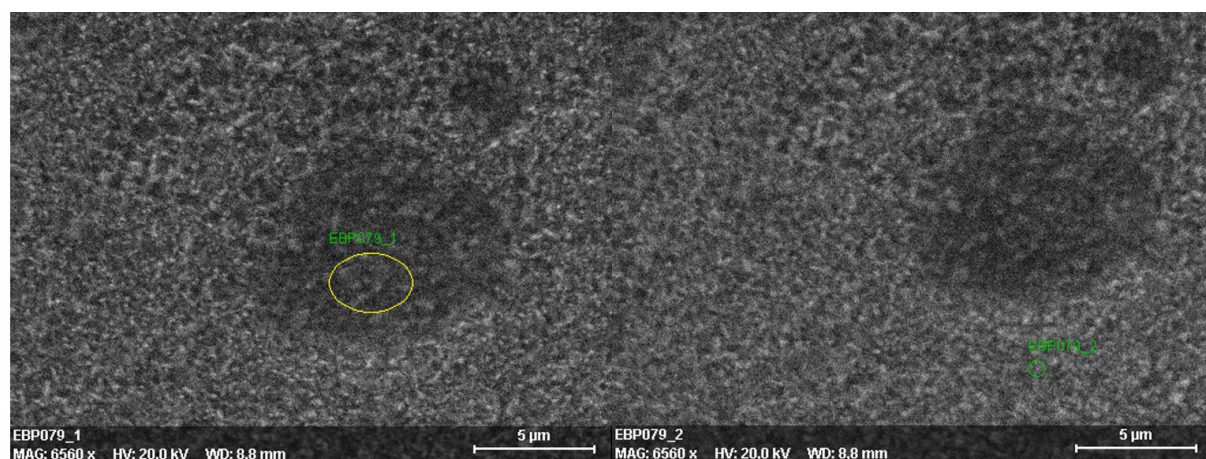
Figure 53. SEM images of EBP-079 surface. a) The marked area for EDX on the surface in the pit area and b) the area for EDX around the darker area in the middle.

Table 13. The main EDX signals of the area in the middle of the image on the EBP-079 surface.

Element	Atomic number	Series	norm. C [wt.-%]	Atom. C [at.-%]	Error [%]
Sn	50	L-series	50.69	12.34	1.7
Si	14	K-series	1.82	1.88	0.2
C	6	K-series	1.57	3.77	1.2
Ti	22	K-series	0.29	0.17	0.1
O	8	K-series	45.12	81.48	9.3
Total:			100 %	100 %	

norm. C [wt.-%] = normalised concentration in weight percent of the element

Atom. C [at.-%] = atomic concentration in weight percent of the element.

Table 14.The main EDX signals of the area at the edges of the image on the EBP-079 surface.

Element	Atomic number	Series	norm. C [wt.-%]	Atom. C [at.-%]	Error [%]
Sn	50	L-series	43.71	9.70	1.3
C	6	K-series	3.64	7.97	0.9
Ti	22	K-series	3.02	1.66	0.3
Si	14	K-series	1.12	1.05	0.1
O	8	K-series	48.26	79.45	8.6
Total:			100 %	100 %	

norm. C [wt.-%] = normalised concentration in weight percent of the element

Atom. C [at.-%] = atomic concentration in weight percent of the element.
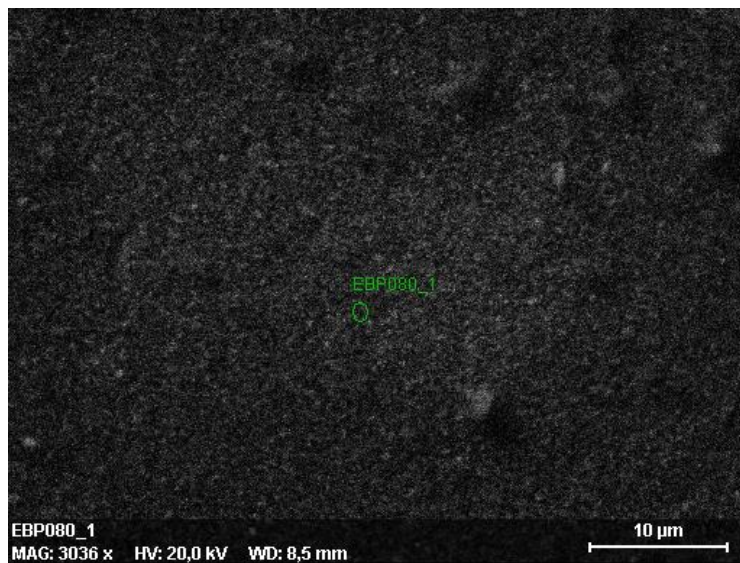
Figure 54. SEM image of EBP-080 surface and the marked area for EDX.

Table 15. The main EDX signals of EBP-080 surface.

Element	Atomic number	Series	norm. C [wt.-%]	Atom. C [at.-%]	Error [%]
Sn	50	L-series	43.63	9.38	1.2
C	6	K-series	9.56	20.32	1.5
Ti	22	K-series	3.40	1.81	0.3
Si	14	K-series	0.90	0.82	0.1
O	8	K-series	42.32	67.54	6.8
Total:			100 %	100 %	

norm. C [wt.-%] = normalised concentration in weight percent of the element

Atom. C [at.-%] = atomic concentration in weight percent of the element.

10 Conclusions

In the experimental part 6 different MOF compounds were synthetised successfully by saturation crystallisations in a room temperature, except of a single compound that was attempted to be synthetised by refluxing. Four different MOFs were grown on electrode materials, of which one on nickel foam (NF) and three on FTO glass. All the samples were characterised with PXRD and TG/DSC methods and the electrode materials were imaged by SEM as well as analysed with EDX. In this work, FTO and NF electrode materials were examined for the first time and the aim of the work, in regards to the materials, was to map their function as a growth medium for MOFs.

The extremely fast synthesis method for CuI(bpy)-MOF nicely exemplified that catalytic MOFs can be prepared in a very small time frame, which is beneficial considering commercial production. Inspired by the success of the CuI(bpy)-MOF, the Ce-UiO-66-MOFs Ce-UiO-66, Ce-UiO-66-NH$_2$, Ce-UiO-66-Br, Ce-UiO-66-COOH and Ce-Ui-66-NO$_2$ were synthetised in a room temperature also in a relatively short synthesis time. The large modification possibilities of the functional group of the Ce-UiO-66-MOF enabled variations for example in the heat resistance without changing the MOF network topology. When searching for structures that can be used in green hydrogen production, mild reaction parameters, such as low reaction temperatures and the avoidance of organic solvents, would be ideal for achieving more environmentally friendly methods.

The aim of the synthesis of NH_2-UiO-66 was to test a method, which would require less reactants and less time, than the syntheses reported in the earlier literature. However, it appeared, that by combining these methods the yield remained small, and the amorphous product was probably not purely the wanted compound. Therefore, it can be concluded, that with a relatively quick reflux conditions, auxiliary substances are needed or with simpler reagents, longer, solvothermal synthesis must presumably be used. In addition, the reaction of NH_2-UiO-66 requires equal amounts of substances of linker and metal node, but only after the synthesis it was noticed, that the mass or amount of substance of NH_2-BDC-linker was reported incorrectly in the Kandiah group's[73] paper, which could have affected the yield negatively.

ZnO works as a good electrode material but requires a surface passivation layer, which can be achieved for example by ZIF-8-MOF. Therefore, $Ni(OH)_2$-ZIF-8-ZnO-layer was synthetised on top of NF electrode material. According to the PXRD and SEM-EDX results, it is clear, that the characterisation of the $Ni(OH)_2$ZIF-8-ZnO on nickel foam would require different, or additional characterisation methods. As both of the ZnO and ZIF-8 contain the same metal, the elemental mapping did not offer reliable information about the synthetised layers. Therefore, it was assumed, that the visual separation of the morphologies of the two species would be accurate enough method to distinguish them from each other. However, the SEM images of the $Ni(OH)_2$ZIF-8-ZnO coatings corresponded visually more of a pure ZnO than the target compound. For comparison, a pure ZnO-layer was tried to grow on a NF, but the sample may have damaged during the synthesis, and the EDX suggested, that there was no ZnO-nanorod arrays, and even visually the particles did not correspond a morphology of nanorods. Thus, it did not work as a reference sample. In addition, the characterisation of $Ni(OH)_2$ nanosheets was difficult, because the signal of the nickel may get mixed with the signal coming from the nickel foam. Therefore, for easier characterisation, it would be better if the synthetised sample and the electrode material to contained different elements. Nevertheless, the nickel foam itself was found to be easy to coat and operate with.

Au@NH_2-MIL-125, NH_2-MIL-125 and NH_2-Ce-UiO-66-MOFs were grown on FTO substrates on top of TiO_2 nanorod layers. The first growth attempt of a TiO_2-layer failed, but the next syntheses without $TiCl_4$ were more successful. However, as in the case of NF samples, the MOF-structure could not be detected by the PXRD or EDX. In the case of Au@NH_2-MIL-125 and NH_2-Ce-UiO-66 the MOF-structures were concluded to have successfully grown on top of the TiO_2 nanorods only by visual inspection of the SEM images, which were compared to the literature. However, the presence of Au NPs was not confirmed. The SEM analysis of NH_2-MIL-125 without the nanoparticles showed only a smooth indistinguishable layers.

As a conclusion, the size difference of a nano scale MOF and macro scale substrate hampers the detection of the MOF compounds when it is grown on top of an electrode material. Therefore, a reliable characterisation of a MOF-structure grown on an electrode would require additional or totally different methods. However, it was observed, that room temperature syntheses of powdery samples can be achieved relatively fast and with a small number of different reactants. Consequently, further research wherein such compounds are grown on the electrode would be highly desirable to achieve composite materials suitable for green hydrogen production in a PEC cell.

References

1.   James G. Speight, *Global Climate Change Demystified,* 1. Edition, John Wiley & Sons, Incorporated, **2019**.

2.   Campbell, N. A.; Urry, L. A.; Cain, M. L.; Wasserman, S. A.; Minorsky, P. V. & Reece, J. B, *Biology : a global approach*, Pearson, **2021.**

3.   The European Commission, The European Green Deal, **2019**.

4.   P. K. Pahwa & G. K. Pahwa, *Hydrogen Economy*, The Energy and Resources Institute, New Delhi, **2014**.

5.   Eberle, U.; Felderhoff, M. & Schüth, F., Chemical and Physical Solutions for Hydrogen Storage, *Angewandte Chemie International Edition*, **2009**, *48*, 6608–6630.

6.   A hydrogen strategy for a climate-neutral Europe, *COM(2020) 301 final*, **2020**.

7.   Makaryan, I. A. & Sedov, I. V., Cost-Effectiveness Assessment of the Scale of Hydrogen Production by Various Methods, *Russ. J. Gen. Chem.*, **2021**, *91*, 2743–2757.

8.   Voldsund, M.; Jordal, K. & Anantharaman, R., Hydrogen production with CO_2 capture, *Int. J. Hydrogen Energy*, **2016**, *41*, 4969–4992.

9.   Nikolaidis, P. & Poullikkas, A., A comparative overview of hydrogen production processes, *Renewable and Sustainable Energy Reviews*, **2017**, 67, 597–611.

10. GH2 Facts: CO_2 emissions per kg of hydrogen depending on the method of production, Hydrogen Newsletter. Referred on 12.4.2024. https://www.hydrogennewsletter.com/gh2-facts/

11. Wang, Z.; Roberts, R. R.; Naterer, G. F. & Gabriel, K. S., Comparison of thermochemical, electrolytic, photoelectrolytic and photochemical solar-to-hydrogen production technologies, *Int. J. Hydrogen Energy*, **2012**, *37*, 16287–16301.

12. Eyvaz, M., Advances In Hydrogen Generation Technologies, *Advances In Hydrogen Generation Technologies*, **2019**, 134.

13. van de Krol, R. & Grätzel, M., *Photoelectro-chemical Hydrogen Production*, 1. Edition, Springer New York, **2014**.

14. El-Shafie, M., Hydrogen production by water electrolysis technologies: A review, *Results in Engineering*, **2023**, *20*, 101426.

15. Bak, T.; Nowotny, J.; Rekas, M. & Sorrell, C. C., Photo-electrochemical hydrogen generation from water using solar energy. Materials-related aspects, 27, **2002**.

16. Mills, A. & Le Hunte, S., An overview of semiconductor photocatalysis, *J. Photochem. Photobiol. A. Chem.*, **1997**, *108*, 1–35.

17. Wang, L.; Shi, X.; Jia, Y.; Cheng, H.; Wang, L. & Wang, Q., Recent advances in bismuth vanadate-based photocatalysts for photoelectrochemical water splitting, *Chinese Chemical Letters*, **2021**, 32, 1869–1878.

18. Dutta, R.; Shrivastav, R.; Srivastava, M.; Verma, A.; Saxena, S.; Biswas, N. K.; Satsangi, V. R. & Dass, S., MOFs in photoelectrochemical water splitting: New horizons and challenges, *Int. J. Hydrogen Energy*, **2022**, *47*, 5192–5210.

19. Yacobi, B. G., *Semiconductor Materials*, Springer US, **2003**.

20. Kisch, Horst., Semiconductor Photocatalysis : Principles and Applications., **2014**, 266.

21. Brydson, R., Electron Energy Loss Spectroscopy, **2020**.

22. Nguyen, H. L., Metal–Organic Frameworks for Photocatalytic Water Splitting, *Solar RRL*, **2021**, 5.

23. Greiner, M. T. & Lu, Z. H., Thin-film metal oxides in organic semiconductor devices: their electronic structures, work functions and interfaces, *NPG Asia Mater.*, **2013**, *5*, e55.

24. Altaf, M.; Sohail, M.; Mansha, M.; Iqbal, N.; Sher, M.; Fazal, A.; Ullah, N. & Isab, A. A., Synthesis, Characterization, and Photoelectrochemical Catalytic Studies of a Water-Stable Zinc-Based Metal–Organic Framework, *ChemSusChem*, **2018**, *11*, 542–546.

25. Gong, Y. N.; Liu, J. W.; Shao, B. Z.; Zhong, D. C. & Lu, T. B., Stable metal–organic frameworks for PEC water splitting, *FlatChem*, **2021**, *27*, 100240.

26. Ali, M.; Pervaiz, E.; Noor, T.; Rabi, O.; Zahra, R. & Yang, M., Recent advancements in MOF-based catalysts for applications in electrochemical and photoelectrochemical water splitting: A review, *Int. J. Energy Res.*, **2021**, *45*, 1190–1226.

27. Han, Y.; Zhai, J.; Zhang, L. & Dong, S., Direct carbonization of cobalt-doped NH$_2$-MIL-53(Fe) for electrocatalysis of oxygen evolution reaction, *Nanoscale*, **2015**, *8*, 1033–1039.

28. Anantharaj, S. & Noda, S., How properly are we interpreting the Tafel lines in energy conversion electrocatalysis?, *Mater. Today Energy*, **2022**, *29*.

29. Pettinari, C.; Mhetti, F.; Mosca, N.; Tosi, G. & Drozdov, A., Application of metal − organic frameworks, *Polym. Int.*, **2017**, 66, 731–744.

30. Stock, N. & Biswas, S., Synthesis of Metal-Organic Frameworks (MOFs): Routes to Various MOF Topologies, Morphologies, and Composites, *Chem. Rev.*, **2011**, *112*, 933–969.

31. Yoon, J. W.; Kim, J. H.; Kim, C.; Jang, H. W. & Lee, J. H., MOF-Based Hybrids for Solar Fuel Production, *Adv. Energy Mater*, **2021**, 11.

32. Seoane, B.; Castellanos, S.; Dikhtiarenko, A.; Kapteijn, F. & Gascon, J., Multi-scale crystal engineering of metal organic frameworks, *Coord. Chem. Rev.*, **2016**, *307*, 147–187.

33. O'Keeffe, M. & Yaghi, O. M., Deconstructing the crystal structures of metal-organic frameworks and related materials into their underlying nets, *Chem. Rev.*, **2012**, *112*, 675–702.

34. Ghanbari, T.; Abnisa, F. & Wan Daud, W. M. A., A review on production of metal organic frameworks (MOF) for CO_2 adsorption, *Science of the Total Environment*, **2020**, 707.

35. Groom, C. R.; Bruno, I. J.; Lightfoot, M. P. & Ward, S. C., The Cambridge Structural Database, *urn:issn:2052-5206*, **2016**, *72*, 171–179.

36. Moghadam, P. Z.; Li, A.; Wiggin, S. B.; Tao, A.; Maloney, A. G. P.; Wood, P. A.; Ward, S. C. & Fairen-Jimenez, D., Development of a Cambridge Structural Database Subset: A Collection of Metal-Organic Frameworks for Past, Present, and Future, *Chemistry of Materials*, **2017**, *29*, 2618–2625.

37. Mandal, S.; Natarajan, S.; Mani, P. & Pankajakshan, A., Post-Synthetic Modification of Metal–Organic Frameworks Toward Applications, *Adv. Funct. Mater.*, **2021**, *31*.

38. Butova, V. V; Soldatov, M. A.; Guda, A. A.; Lomachenko, K. A. & Lamberti, C., Metal-organic frameworks: structure, properties, methods of synthesis and characterization, *Russian Chemical Reviews*, **2016**, *85*, 280–307.

39. Thomas, K. M., Adsorption and desorption of hydrogen on metal–organic framework materials for storage applications: comparison with other nanoporous materials, *Dalton Transactions*, **2009**, 1487–1505.

40. Reinsch, H., "Green" Synthesis of Metal-Organic Frameworks, *Eur. J. Inorg. Chem.*, **2016**, *2016*, 4290–4299.

41. Lv, L. L.; Yang, J.; Zhang, H. M.; Liu, Y. Y. & Ma, J. F., Metal-ion exchange, small-molecule sensing, selective dye adsorption, and reversible iodine uptake of three

coordination polymers constructed by a new resorcin[4]arene-based tetracarboxylate, *Inorg. Chem.*, **2015**, *54*, 1744–1755.

42. Yuan, S.; Chen, Y. P.; Qin, J.; Lu, W.; Wang, X.; Zhang, Q.; Bosch, M.; Liu, T. F.; Lian, X. & Zhou, H. C., Cooperative Cluster Metalation and Ligand Migration in Zirconium Metal–Organic Frameworks, *Angewandte Chemie International Edition*, **2015**, *54*, 14696–14700.

43. Zhang, L.; Cui, P.; Yang, H.; Chen, J.; Xiao, F.; Guo, Y.; Liu, Y.; Zhang, W.; Huo, F. & Liu, B., Metal-Organic Frameworks as Promising Photosensitizers for Photoelectrochemical Water Splitting, *Adv. Sci. (Weinh)*, **2015**, *3*.

44. Liu, T. F.; Zou, L.; Feng, D.; Chen, Y. P.; Fordham, S.; Wang, X.; Liu, Y. & Zhou, H. C., Stepwise synthesis of robust metal-organic frameworks via postsynthetic metathesis and oxidation of metal nodes in a single-crystal to single-crystal transformation, *J. Am. Chem. Soc.*, **2014**, *136*, 7813–7816.

45. Wang, W.; Song, X. W.; Hong, Z.; Li, B.; Si, Y.; Ji, C.; Su, K.; Tan, Y.; Ju, Z.; Huang, Y.; Chen, C. N. & Yuan, D., Incorporation of iron hydrogenase active sites into a stable photosensitizing metal-organic framework for enhanced hydrogen production, *Appl. Catal. B.*, **2019**, *258*.

46. Cohen, S. M., Postsynthetic Methods for the Functionalization of Metal-Organic Frameworks, *Chem. Rev.*, **2012**, *112*, 970–1000.

47. Johnson, B. A.; Bhunia, A. & Ott, S., Electrocatalytic water oxidation by a molecular catalyst incorporated into a metal–organic framework thin film, *Dalton Transactions*, **2017**, *46*, 1382–1388.

48. Yuan, S.; Chen, Y.-P.; Qin, J.-S.; Lu, W.; Zou, L.; Zhang, Q.; Wang, X.; Sun, X. & Zhou, H.-C., Linker Installation: Engineering Pore Environment with Precisely Placed Functionalities in Zirconium MOFs, **2016**.

49. Dincă, M. & Long, J. R., High-enthalpy hydrogen adsorption in cation-exchanged variants of the microporous metal-organic framework $Mn_3[(Mn_4Cl)_3(BTT)_8(CH_3OH)_{10}]_2$, *J. Am. Chem. Soc.*, **2007**, *129*, 11172–11176.

50. Guo, Z.; Panda, D. K.; Gordillo, M. A.; Khatun, A.; Wu, H.; Zhou, W. & Saha, S., Lowering Band Gap of an Electroactive Metal-Organic Framework via Complementary Guest Intercalation, *ACS Appl. Mater. Interfaces*, **2017**, *9*, 32413–32417.

51. Suryanarayana, C. & Norton, M. Grant., X-Ray diffraction : a practical approach, 273, **1998**.

52. Teknillisten tieteiden akatemia; Kivalo, P.; Suoninen, E. & Tuominen, P., *Instrumenttianalytiikka: 4, Röntgen- ja fotoelektronispektrometria 1*, Gummerus, **1982**.

53. Billinge, S. & Dinnebier, R., Principles of Powder Diffraction, *Powder Diffraction: Theory and Practice*, **2008**.

54. Aitipamula, S. & Vangala, V. R., X-Ray Crystallography and its Role in Understanding the Physicochemical Properties of Pharmaceutical Cocrystals, *J. Indian. Inst. Sci.*, **2017**, *97*, 227–243.

55. Speakman, S. A., Introduction to x-ray powder diffraction data analysis, *Center for Materials Science and Engineering at MIT*, **2013**.

56. Royal Society of Chemistry (Great Britain), *Principles of Thermal Analysis and Calorimetry*, 2nd edition, **2016**.

57. Mohammed, A. & Abdullah, A., SCANNING ELECTRON MICROSCOPY (SEM): A REVIEW, N.d.

58. Electron Microscopy, TEM vs SEM, Thermo Fisher Scientific, N.d. Referred on 14.3.2024. https://www.thermofisher.com/fi/en/home/materials-science/learning-center/applications/sem-tem-difference.html

59. Allen, L. J.; D'Alfonso, J. D.; Findlay, S. D.; Lebeau, J. M.; Lugg, N. R. & Stemmer, S., Elemental mapping in scanning transmission electron microscopy, *J. Phys. Conf. Ser.*, **2010**, *241*, 012061.

60. Yang, J.; Grzech, A.; Mulder, F. M. & Dingemans, T. J., Methyl modified MOF-5: a water stable hydrogen storage material, *Chem. Commun.*, **2011**, *47*, 8.

61. Butler, K. T.; Hendon, C. H. & Walsh, A., Electronic Chemical Potentials of Porous Metal−Organic Frameworks Terms of Use, *J. Am. Chem. Soc.*, **2014**, *136*.

62. Guo, X.; Liu, L.; Xiao, Y.; Qi, Y.; Duan, C. & Zhang, F., Band gap engineering of metal-organic frameworks for solar fuel productions, *Coord. Chem. Rev.*, **2021**, *435*, 213785.

63. Sippel, P.; Denysenko, D.; Loidl, A.; Lunkenheimer, P.; Sastre, G. & Volkmer, D., Dielectric Relaxation Processes, Electronic Structure, and Band Gap Engineering of MFU-4-type Metal-Organic Frameworks: Towards a Rational Design of Semiconducting Microporous Materials, *Adv. Funct. Mater.*, **2014**, *24*, 3885–3896.

64. Gascon, J.; Hernández-Alonso, M. D.; Almeida, A. R.; van Klink, G. P. M.; Kapteijn, F. & Mul, G., Isoreticular MOFs as efficient photocatalysts with tunable band gap: an operando FTIR study of the photoinduced oxidation of propylene., *ChemSusChem*, **2008**, *1*, 981–983.

65. Choi, J. H.; Choi, Y. J.; Lee, J. W.; Shin, W. H. & Kang, J. K., Tunability of electronic band gaps from semiconducting to metallic states via tailoring Zn ions in MOFs with Co ions, *Physical Chemistry Chemical Physics*, **2009**, *11*, 628–631.

66. Xie, L. S.; Skorupskii, G. & Dincă, M., Electrically Conductive Metal-Organic Frameworks, *Chem. Rev.*, **2020**, *120*, 8536–8580.

67. Duan, J.; Goswami, S.; Patwardhan, S. & Hupp, J. T., Does the Mode of Metal−Organic Framework/Electrode Adhesion Determine Rates for Redox-Hopping-Based Charge Transport within Thin-Film Metal−Organic Frameworks?, *J. Phys. Chem. C*, **2022**, *2022*, 4611.

68. Takaishi, S.; Hosoda, M.; Kajiwara, T.; Miyasaka, H.; Yamashita, M.; Nakanishi, Y.; Kitagawa, Y.; Yamaguchi, K.; Kobayashi, A. & Kitagawa, H., Electroconductive porous coordination polymer $Cu[Cu(pdt)_2]$ composed of donor and acceptor building units, *Inorg. Chem.*, **2009**, *48*, 9048–9050.

69. Goswami, S.; Hod, I.; Duan, J. D.; Kung, C.-W.; Rimoldi, M.; Malliakas, C. D.; Palmer, R. H.; Farha, O. K. & Hupp, J. T., Anisotropic Redox Conductivity within a Metal−Organic Framework Material, *J. Am. Chem. Soc*, **2019**, *141*, 52.

70. Yoon, J. W.; Kim, D. H.; Kim, J. H.; Jang, H. W. & Lee, J. H., NH_2-MIL-125(Ti)/TiO_2 nanorod heterojunction photoanodes for efficient photoelectrochemical water splitting, *Appl. Catal. B.*, **2019**, *244*, 511–518.

71. Yang, H.; Bright, J.; Kasani, S.; Zheng, P.; Musho, T.; Chen, B.; Huang, L. & Wu, N., Metal–organic framework coated titanium dioxide nanorod array p–n heterojunction photoanode for solar water-splitting, *Nano. Res.*, **2019**, *12*, 643–650.

72. Batten, S. R.; Jeffery, J. C. & Ward, M. D., Studies of the construction of coordination polymers using linear pyridyl-donor ligands, **1999**.

73. Kandiah, M.; Nilsen, M. H.; Usseglio, S.; Jakobsen, S.; Olsbye, U.; Tilset, M.; Larabi, C.; Quadrelli, E. A.; Bonino, F. & Lillerud, K. P., Synthesis and stability of tagged UiO-66 Zr-MOFs, *Chemistry of Materials*, **2010**, *22*, 6632–6640.

74. Motegi, H.; Yano, K.; Setoyama, N.; Matsuoka, Y.; Ohmura, T. & Usuki, A., A facile synthesis of UiO-66 systems and their hydrothermal stability, *Journal of Porous Materials*, **2017**, *24*, 1327–1333.

75. Li, X.; Liu, S.; Fan, K.; Liu, Z.; Song, B.; Yu, J.; Li, X.; Liu, S.; Fan, K.; Yu, J. & Liu, Z. MOF-Based Transparent Passivation Layer Modified ZnO Nanorod Arrays for Enhanced Photo-Electrochemical Water Splitting, *Adv. Energy Mater.*, **2018**, *8*, 1800101.

76. Dai, S.; Montero-Lanzuela, E.; Tissot, A.; Baldoví, H. G.; García, H.; Navalón, S. & Serre, C., Room temperature design of Ce(IV)-MOFs: from photocatalytic HER and OER to overall water splitting under simulated sunlight irradiation, *Chem. Sci.*, **2023**, *14*, 3451–3461.

77. Wang, H.; Bai, Y.; Wu, Q.; Zhou, W.; Zhang, H.; Li, J. & Guo, L., Rutile TiO_2 nano-branched arrays on FTO for dye-sensitized solar cells, *Physical Chemistry Chemical Physics*, **2011**, *13*, 7008–7013.

78. Gates-Rector, S. & Blanton, T., The Powder Diffraction File: a quality materials characterization database, **2019**.

79. Shi, D.; Zheng, R.; Sun, M.-J.; Cao, X.; hun-Xiao Sun, C.; Cui, C.-J.; Liu, C.-S.; Zhao, J.; Miao Du, and; Shi, D.; Sun, C.; Cui, C.; Liu, C.; Du, M.; -J Sun, D.; ao, D.; Zheng, R. & Zhao, J., Semiconductive Copper(I)–Organic Frameworks for Efficient Light-Driven Hydrogen Generation Without Additional Photosensitizers and Cocatalysts, *Angewandte Chemie International Edition*, **2017**, *56*, 14637–14641.

80. Kobayashi, A.; Fujii, M.; Shigeta, Y.; Yoshida, M. & Kato, M., Quantitative Solvent-Free Thermal Synthesis of Luminescent Cu(I) Coordination Polymers, *Inorg. Chem.*, **2019**, *58*, 4456–4464.

81. Synthesis, characterization and adsorption ability of UiO-66-NH_2, **2015**.

82. Bailey, M. & Brown, C. J., The crystal structure of terephthalic acid, *Acta Crystallogr.*, **1967**, *22*, 387–391.

83. Lammert, M.; Wharmby, M. T.; Smolders, S.; Bueken, B.; Lieb, A.; Lomachenko, K. A.; De Vos, D. & Stock, N., Cerium-based metal organic frameworks with UiO-66 architecture: synthesis, properties and redox catalytic activity, *Chem. Commun.*, **2015**, *51*, 12578–12581.

84. Maier, J. & Göpel, W., Investigations of the bulk defect chemistry of polycrystalline Tin(IV) oxide, *J. Solid State Chem.*, **1988**, *72*, 293–302.

85. Zhang, Y.; Song, J.; Shao, W. & Li, J., Au@NH$_2$-MIL-125(Ti) heterostructure as light-responsive oxidase-like mimic for colorimetric sensing of cysteine, *Microporous and Mesoporous Materials*, **2021**, *310*, 110642.

86. Ding, J.; Chen, M.; Du, X.; Shang, R.; Xia, M.; Hu, J. & Zhong, Q., Visible-Light-Driven Photoreduction of CO$_2$ to CH$_4$ with H$_2$O Over Amine-Functionalized MIL-125(Ti), *Catal. Letters*, **2019**, *149*, 3287–3295.

87. Gao, J.; Zhang, S.; Ma, X.; Sun, Y. & Zhang, X., Two-Dimensional Sb Modified TiO$_2$ Nanorod Arrays as Photoanodes for Efficient Solar Water Splitting, *Nanomaterials,* **2023**, *13*, 1293.

88. Miyamoto, M.; Kohmura, S.; Iwatsuka, H.; Oumi, Y. & Uemiya, S., In situ solvothermal growth of highly oriented Zr-based metal organic framework UiO-66 film with monocrystalline layer, *CrystEngComm*, **2015**, *17*, 3422–3425.

Appendices

Appendix 1. The PXRD measurement parameters.

Appendix 2. The synthesis codes and the corresponding compounds

Appendix 3. The measured TG- and DSC-graph of EBP-013-b.

Appendix 4. The measured TG- and DSC-graph of EBP-067.

Appendix 5. The measured TG- and DSC-graphs of Ce-UiO-66-NH$_2$-MOFs.

Appendix 6. The SEM-EXD spectrum and a table of the SEM-EDX signals of EBP-068.

Appendix 7. The SEM-EDX spectra and tables of the signals of EBP-081.

Appendix 8. The SEM-EXD spectrum and a table of the SEM-EDX signals of EBP-076.

Appendix 9. The SEM-EDX spectra and tables of the signals of EBP-077.

Appendix 10. The SEM-EDX spectra and tables of the signals of EBP-079.

Appendix 11. The SEM-EDX spectrum and a table of the signals of EBP-080.

Parameter	Value
Start angle (°2θ)	3–6
End angle (°2θ)	50–80
Step size (°)	0.0167
Time per step (s)	40–200
X-ray tube voltage (kV)	45
X-ray-tube current (mA)	40
Cu K-α (Å)	1.5418
Sample holder	Zero-background plate or modified

Synthesis code	The desired compound	Product description
EBP-013-b	CuI(bpy)	CuI(bpy)
EBP-067	NH_2-UiO-66	Unknown
EBP-068	$Ni(OH)_2$-ZIF-8-ZnO (NF)	At least ZnO
EBP-068-b	$Ni(OH)_2$-ZIF-8-ZnO (NF)	At least ZnO
EBP-069	Ce-UiO-66	Ce-UiO-66 + BDC
EBP-069-b	Ce-UiO-66	Ce-UiO-66 + BDC
EBP-070	Ce-UiO-66-NH_2	Ce-UiO-66-NH_2
EBP-071	Ce-UiO-66-Br	Ce-UiO-66-Br
EBP-072	Ce-UiO-66-COOH	Ce-UiO-66-COOH
EBP-073	NH_2-MIL-125/TiO_2 (FTO)	FTO film peeled off
EBP-074	Au@NH_2-MIL-125/TiO_2 (FTO)	Au NPs not detected
EBP-075	Au@NH_2-MIL-125/TiO_2 (FTO)	Unknown particles, no EDX
EBP-076	NH_2-MIL-125/TiO_2 (FTO)	NH_2-MIL-125/TiO_2
EBP-077	NH_2-MIL-125/TiO_2 (FTO)	At least TiO_2
EBP-078	Ce-UiO-66-NO_2	Ce-UiO-66-NO_2
EBP-079	NH_2-Ce-UiO-66 (FTO)	visually NH_2-Ce-UiO-66
EBP-080	NH_2-Ce-UiO-66 (FTO)	possibly NH_2-Ce-UiO-66
EBP-081	ZnO (NF)	damaged

EBP-013-b

Filename:	C:\Data\KuikkaT\EBP-013-b_1.stad
Operator ID:	TK
Sample ID:	EBP-013-b_1
Sample Weight:	7.005 mg
Comment:	#838, 40 mL/min Air, Pt

Onset Y = 100.474 %
Onset X = 209.31 °C

Onset Y = 77.175 %
Onset X = 327.93 °C

X1 = 167.30 °C
Y1 = 100.371 %

X1 = 260.71 °C
Y1 = 77.931 %

X2 = 260.71 °C
Y2 = 77.931 %

X2 = 466.13 °C
Y2 = 23.330 %

Delta Y = 22.440 %

Delta Y = 54.601 %
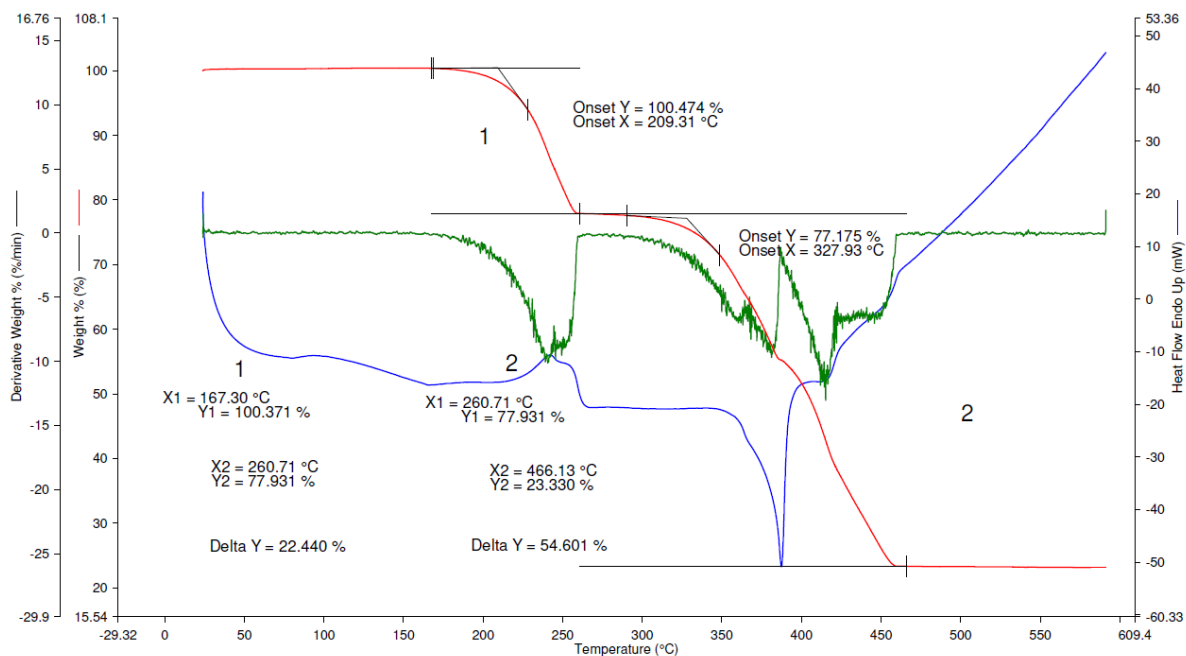
27/04/2023 14:07:54

| 1) Hold for 1.0 min at 24.00°C | 2) Heat from 24.00°C to 600.00°C at 15.00°C/min |

EBP-067

Filename:	C:\Data\KuikkaT\EBP-067_1.stad
Operator ID:	TK
Sample ID:	EBP-067_1
Sample Weight:	5.217 mg
Comment:	#839, 40 mL/min Air, Pt

Onset Y = 99.173 %
Onset X = 45.73 °C

1

X1 = 24.14 °C
Y1 = 99.491 %

X2 = 186.53 °C
Y2 = 90.474 %

Delta Y = 9.016 %

2

X1 = 240.27 °C
Y1 = 89.229 %

X2 = 493.32 °C
Y2 = 34.351 %

Delta Y = 54.878 %

Onset Y = 88.200 %
Onset X = 305.67 °C

2

3

X1 = 493.84 °C
Y1 = 34.347 %

X2 = 593.87 °C
Y2 = 33.817 %

Delta Y = 0.529 %

3

27/04/2023 14:08:34

| 1) Hold for 1.0 min at 24.00°C | 2) Heat from 24.00°C to 600.00°C at 15.00°C/min |

EBP-069

Filename: C:\Data\KuikkaT\EBP-069_1.stad
Operator ID: TK
Sample ID: EBP-069_1
Sample Weight: 6.662 mg
Comment: #945, 40 ml/min, Air, Al2O3

PerkinElmer Thermal Analysis

Onset Y = 98.185 %
Onset X = 44.53 °C

Onset Y = 81.284 %
Onset X = 190.99 °C

Onset Y = 70.404 %
Onset X = 348.73 °C

X1 = 21.98 °C
Y1 = 99.797 %

X2 = 163.93 °C
Y2 = 82.494 %

Delta Y = 17.303 %

X1 = 164.48 °C
Y1 = 82.479 %

X2 = 234.05 °C
Y2 = 75.615 %

Delta Y = 6.864 %

X1 = 234.60 °C
Y1 = 75.583 %

X2 = 597.30 °C
Y2 = 35.130 %

Delta Y = 40.452 %
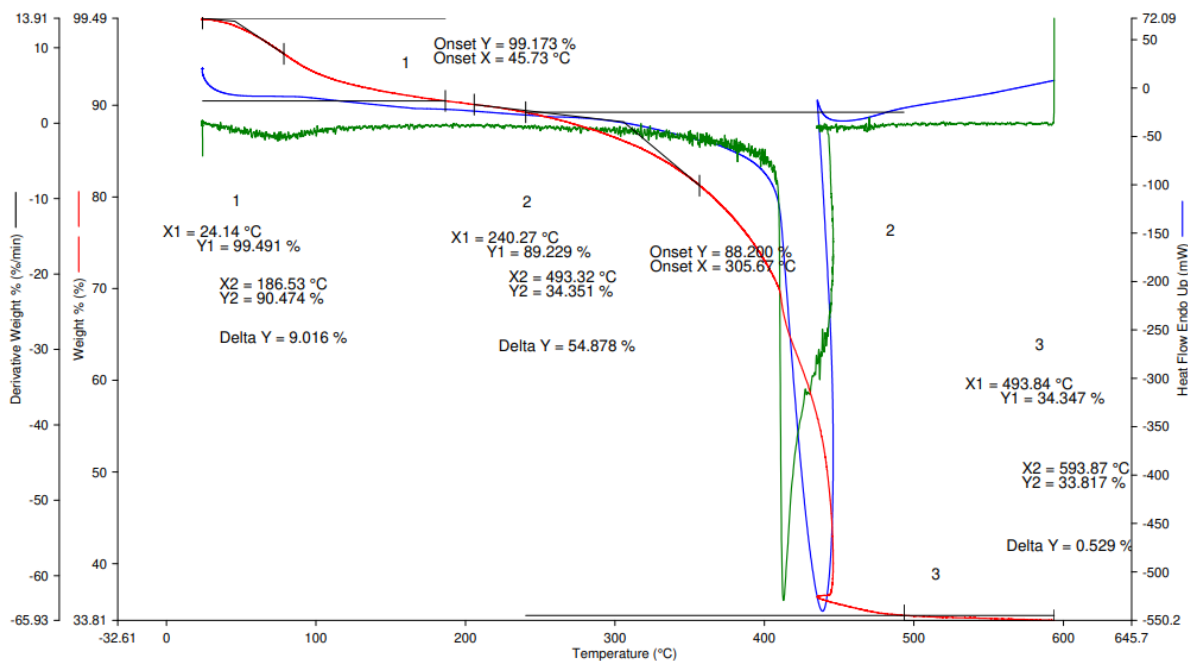
20/06/2023 10:28:55

1) Hold for 1.0 min at 22.00°C   2) Heat from 22.00°C to 600.00°C at 15.00°C/min

EBP-069-b

Filename: C:\Data\KuikkaT\EBP-069-b_1.stad
Operator ID: TK
Sample ID: EBP-069-b_1
Sample Weight: 5.870 mg
Comment: #946, 40 ml/min, Air, Al2O3

Onset Y = 98.632 %
Onset X = 34.97 °C

Onset Y = 89.672 %
Onset X = 164.64 °C

Onset Y = 72.985 %
Onset X = 290.06 °C

Onset Y = 56.736 %
Onset X = 363.88 °C

X1 = 23.06 °C
Y1 = 99.151 %

X2 = 126.61 °C
Y2 = 90.390 %

Delta Y = 8.761 %

X1 = 126.61 °C
Y1 = 90.390 %

X2 = 266.79 °C
Y2 = 75.844 %

Delta Y = 14.545 %

X1 = 267.28 °C
Y1 = 75.790 %

X2 = 340.55 °C
Y2 = 59.041 %

Delta Y = 16.748 %

X1 = 341.03 °C
Y1 = 59.019 %

X2 = 595.83 °C
Y2 = 27.031 %

Delta Y = 31.988 %

15/06/2023 12:28:22

1) Hold for 1.0 min at 22.00°C   2) Heat from 22.00°C to 600.00°C at 15.00°C/min

EBP-070

Filename: C:\Data\KuikkaT\EBP-070_1.stad
Operator ID: TK
Sample ID: EBP-070_1
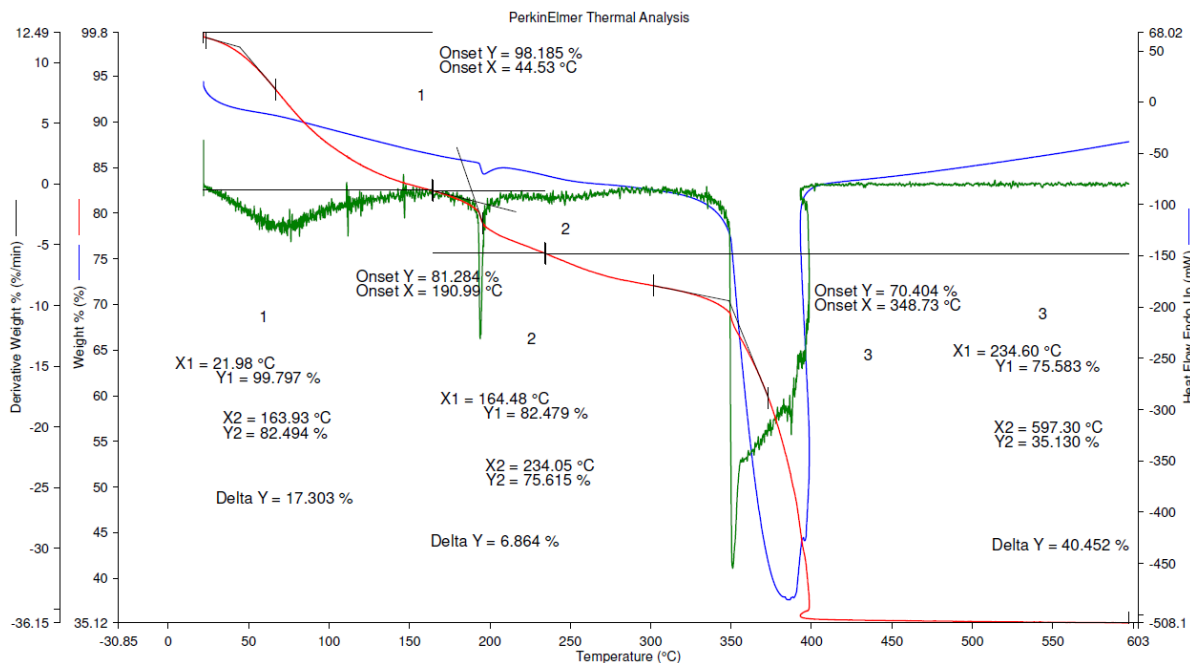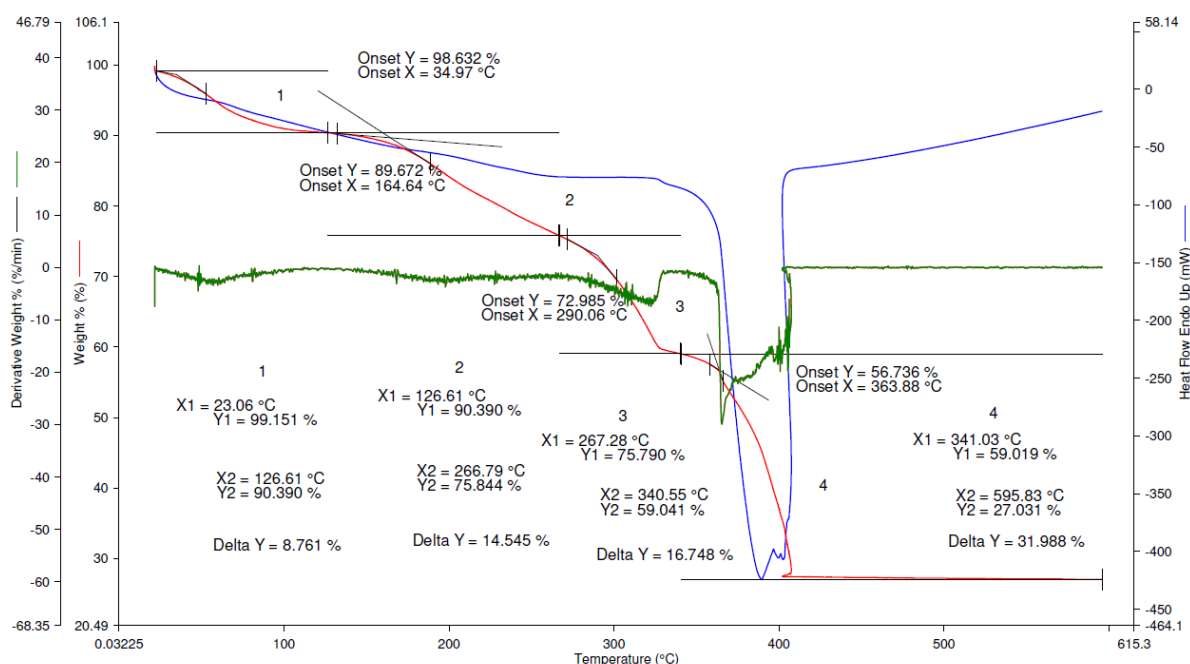Sample Weight: 5.208 mg
Comment: #947, 40 ml/min, Air, Al2O3

Onset Y = 99.704 %
Onset X = 39.72 °C

Onset Y = 90.262 %
Onset X = 145.75 °C

Onset Y = 84.263 %
Onset X = 263.61 °C

X1 = 22.36 °C
Y1 = 99.912 %

X1 = 113.61 °C
Y1 = 91.869 %

X1 = 205.75 °C
Y1 = 86.489 %

X2 = 113.11 °C
Y2 = 91.912 %

X2 = 205.75 °C
Y2 = 86.489 %

X2 = 596.64 °C
Y2 = 34.492 %

Delta Y = 8.000 %

Delta Y = 5.380 %

Delta Y = 51.997 %

15/06/2023 12:34:57

1) Hold for 1.0 min at 22.00°C   2) Heat from 22.00°C to 600.00°C at 15.00°C/min

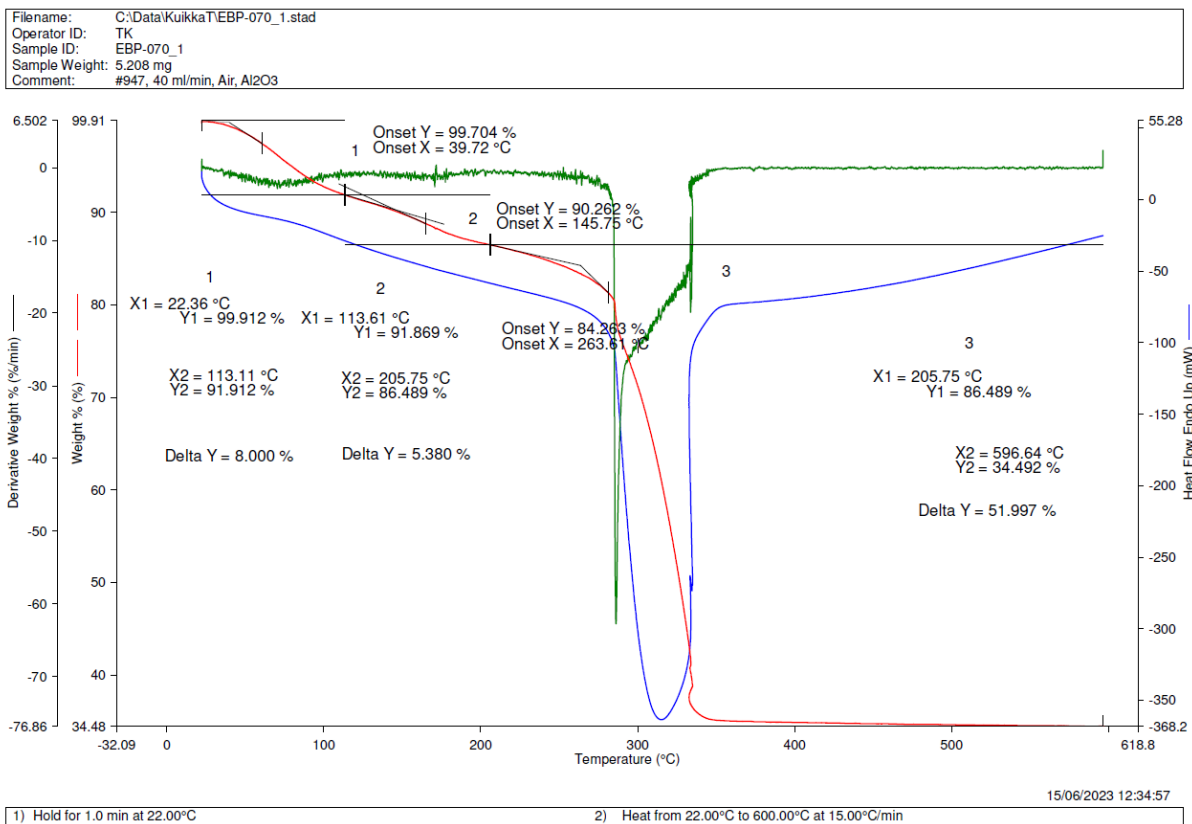## EBP-071

Filename: C:\Data\KuikkaT\EBP-071_1.stad
Operator ID: TK
Sample ID: EBP-071_1
Sample Weight: 7.805 mg
Comment: #948, 40 ml/min, Air, Al2O3

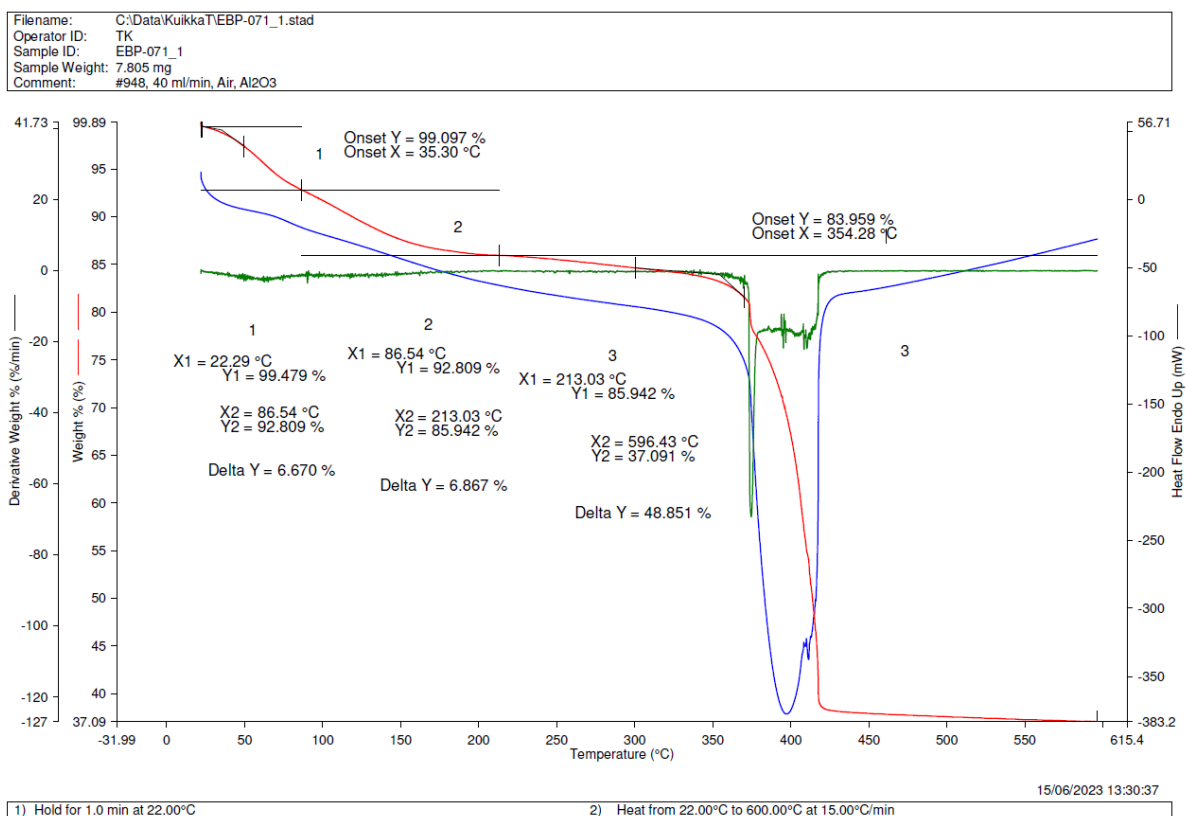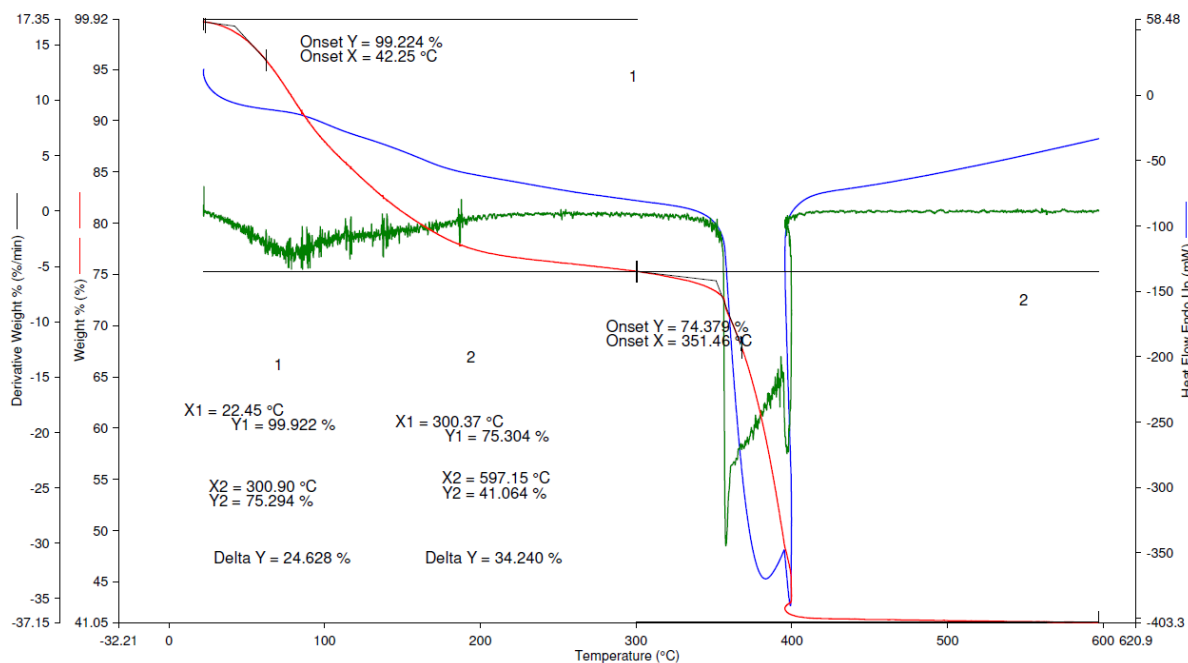Onset Y = 99.097 %
Onset X = 35.30 °C

Onset Y = 83.959 %
Onset X = 354.28 °C

X1 = 22.29 °C
Y1 = 99.479 %

X1 = 86.54 °C
Y1 = 92.809 %

X1 = 213.03 °C
Y1 = 85.942 %

X2 = 86.54 °C
Y2 = 92.809 %

X2 = 213.03 °C
Y2 = 85.942 %

X2 = 596.43 °C
Y2 = 37.091 %

Delta Y = 6.670 %

Delta Y = 6.867 %

Delta Y = 48.851 %

15/06/2023 13:30:37

1) Hold for 1.0 min at 22.00°C   2) Heat from 22.00°C to 600.00°C at 15.00°C/min

EBP-072

EBP-078

EBP-068

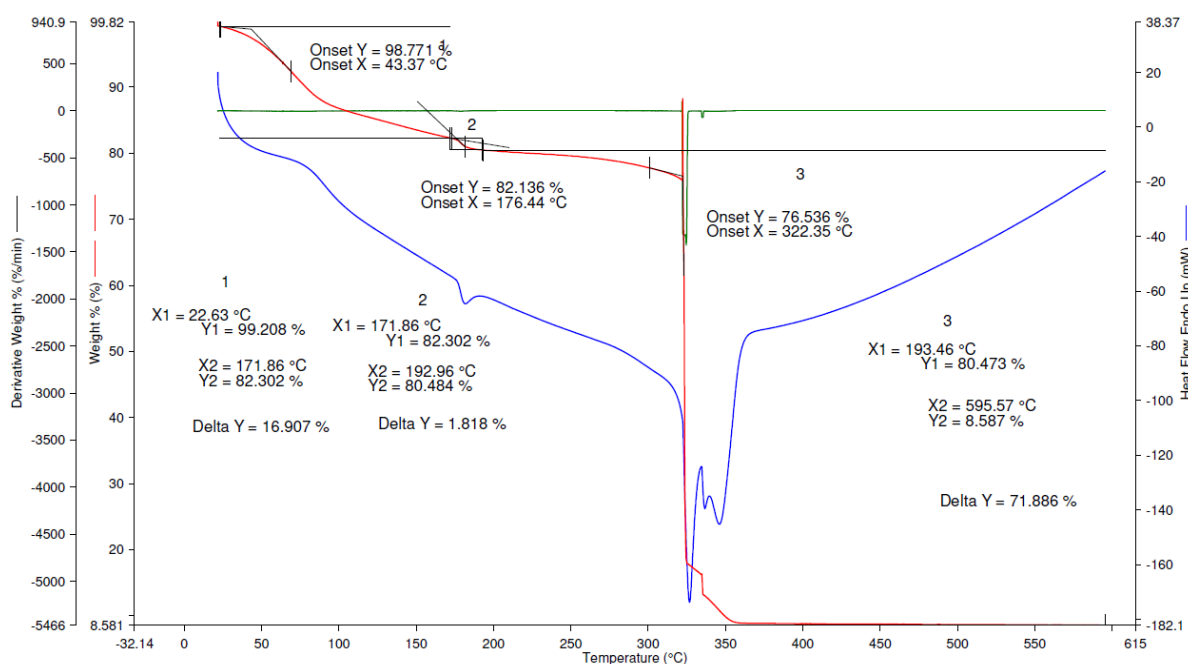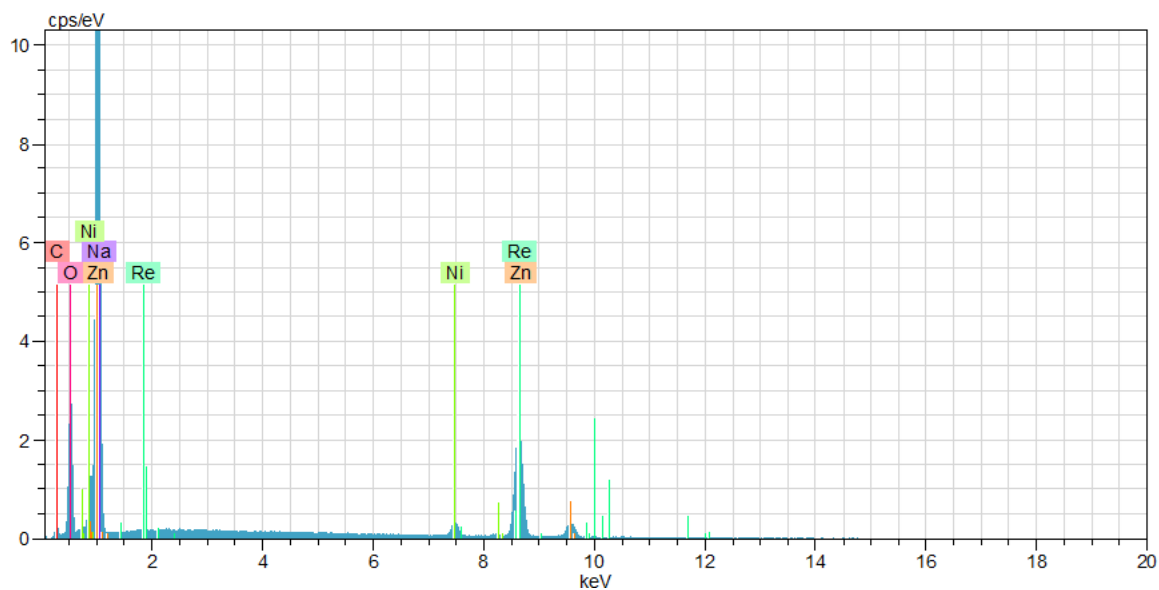
```
El AN  Series   unn. C norm. C Atom. C Error
                [wt.-%] [wt.-%] [at.-%]   [%]
------------------------------------------------
Zn 30 K-series   93,25   67,99   50,26    3,0
Re 75 L-series   15,35   11,19    2,90    5,1
Na 11 K-series   14,42   10,51   22,10    1,0
Ni 28 K-series    4,31    3,14    2,59    0,6
C   6 K-series    0,71    0,52    2,07    0,3
O   8 K-series    9,11    6,65   20,08    1,8
------------------------------------------------
      Total:    137,14  100,00  100,00
```

EBP-081 smoother area


```
El AN  Series   unn. C norm. C Atom. C Error
                [wt.-%] [wt.-%] [at.-%]   [%]
--------------------------------------------
Zn 30 K-series   88,45   50,29   44,82   4,9
Ni 28 K-series   58,80   33,43   33,19   2,4
Re 75 L-series   21,16   12,03    3,76  11,0
C   6 K-series    5,58    3,17   15,39   1,3
Na 11 K-series    1,69    0,96    2,44   1,0
O   8 K-series    0,19    0,11    0,40   0,3
--------------------------------------------
      Total:    175,87  100,00  100,00
```

EBP-081 particles


```
El AN  Series   unn. C norm. C Atom. C Error
                [wt.-%] [wt.-%] [at.-%]   [%]
-------------------------------------------
Zn 30 K-series  117,73   58,95   51,49   6,4
Ni 28 K-series   43,75   21,90   21,32   3,0
Re 75 L-series   22,79   11,41    3,50  11,9
Na 11 K-series   10,39    5,20   12,92   1,3
C   6 K-series    2,87    1,44    6,84   0,9
O   8 K-series    2,21    1,10    3,94   1,0
-------------------------------------------
        Total:  199,74  100,00  100,00
```

EBP-076


```
El AN  Series   unn. C norm. C Atom. C Error
                [wt.-%] [wt.-%] [at.-%]   [%]
-----------------------------------------------
Sn 50 L-series   44,35   48,21   12,39   1,5
Ti 22 K-series    8,38    9,11    5,80   0,4
N  7  K-series    2,52    2,74    5,96   1,3
Si 14 K-series    0,77    0,84    0,91   0,1
C  6  K-series    0,52    0,57    1,44   0,3
O  8  K-series   35,46   38,54   73,50   6,3
-----------------------------------------------
      Total:     91,99  100,00  100,00
```

EBP-077 area with larger particles


```
El AN   Series    unn. C norm. C Atom. C Error
                  [wt.-%] [wt.-%] [at.-%]   [%]
---------------------------------------------
Sn 50 L-series    48,18   56,59   15,41    1,6
Ti 22 K-series     2,14    2,51    1,70    0,3
N  7  K-series     1,12    1,31    3,03    1,5
C  6  K-series     0,90    1,05    2,84    0,4
Si 14 K-series     0,78    0,92    1,06    0,1
O  8  K-series    32,01   37,60   75,96    6,1
---------------------------------------------
      Total:      85,13  100,00  100,00
```

EBP-077 area with smaller particles


```
El  AN   Series    unn. C norm. C Atom. C Error
                   [wt.-%] [wt.-%] [at.-%]   [%]
-------------------------------------------------
Sn 50 L-series     42,41   47,11   12,33    2,1
Ti 22 K-series     10,94   12,15    7,88    0,7
N   7  K-series     2,48    2,76    6,11    3,2
C   6  K-series     0,49    0,55    1,41    0,6
Si 14 K-series      0,45    0,50    0,55    0,3
O   8  K-series    33,25   36,94   71,72    6,7
-------------------------------------------------
       Total:      90,01  100,00  100,00
```

EBP-079 area in the middle of the image


```
El AN  Series    unn. C norm. C Atom. C Error
                 [wt.-%] [wt.-%] [at.-%]   [%]
-----------------------------------------------
Sn 50 L-series    41,65   50,69   12,34   1,7
Si 14 K-series     1,50    1,82    1,88   0,2
C  6  K-series     1,29    1,57    3,77   1,2
Ca 20 K-series     0,42    0,51    0,37   0,3
Ti 22 K-series     0,24    0,29    0,17   0,1
N  7  K-series     0,00    0,00    0,00   0,0
Ce 58 L-series     0,00    0,00    0,00   0,0
O  8  K-series    37,08   45,12   81,48   9,3
-----------------------------------------------
        Total:    82,17  100,00  100,00
```

EBP-079 area at the edges of the image
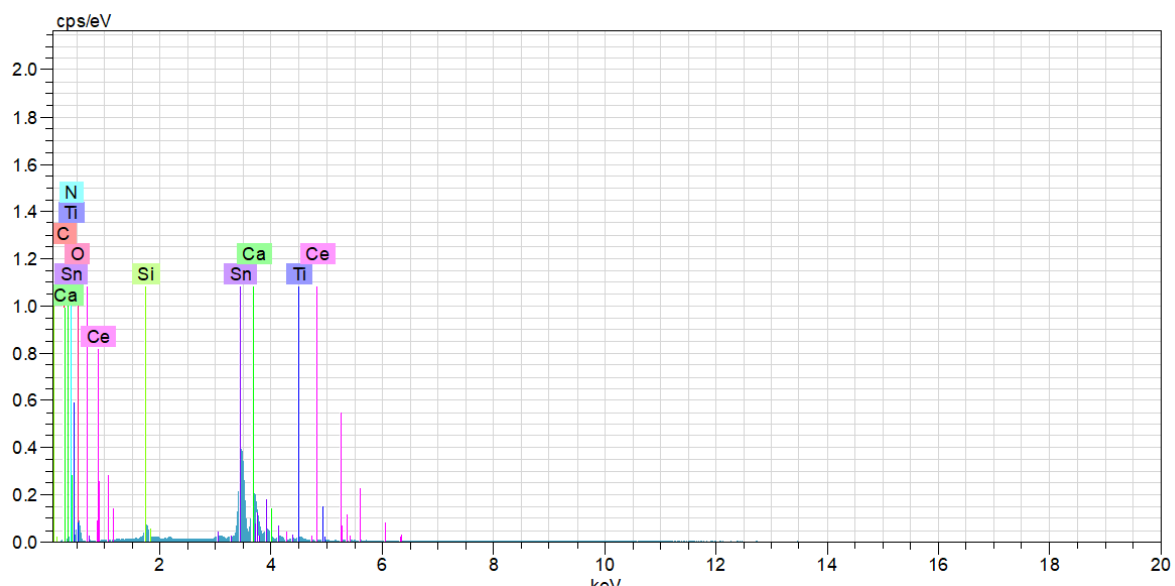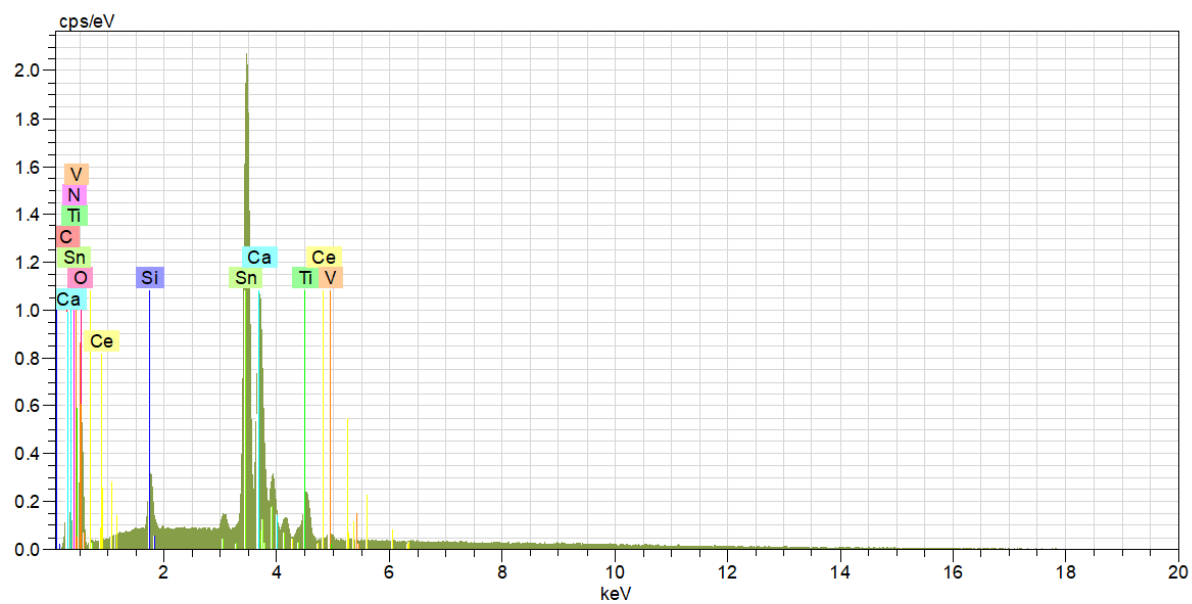
El	AN	Series	unn. C [wt.-%]	norm. C [wt.-%]	Atom. C [at.-%]	Error [%]
Sn	50	L-series	36,51	43,71	9,70	1,3
C	6	K-series	3,04	3,64	7,97	0,9
Ti	22	K-series	2,52	3,02	1,66	0,3
Si	14	K-series	0,94	1,12	1,05	0,1
Ca	20	K-series	0,21	0,25	0,17	0,1
N	7	K-series	0,00	0,00	0,00	0,0
Ce	58	L-series	0,00	0,00	0,00	0,0
V	23	K-series	0,00	0,00	0,00	0,0
O	8	K-series	40,31	48,26	79,45	8,6
		Total:	83,53	100,00	100,00	

EBP-080


```
El AN  Series    unn. C norm. C Atom. C Error
                 [wt.-%] [wt.-%] [at.-%]   [%]
------------------------------------------------
Sn 50 L-series    36,67   43,63    9,38   1,2
C   6 K-series     8,03    9,56   20,32   1,5
Ti 22 K-series     2,86    3,40    1,81   0,3
Si 14 K-series     0,76    0,90    0,82   0,1
Ca 20 K-series     0,16    0,19    0,12   0,1
N   7 K-series     0,00    0,00    0,00   0,0
Ce 58 L-series     0,00    0,00    0,00   0,0
V  23 K-series     0,00    0,00    0,00   0,0
O   8 K-series    35,57   42,32   67,54   6,8
------------------------------------------------
      Total:      84,05  100,00  100,00
```